Red Blood Cells and Disturbed Hemodynamics in Microbubble Targeting

---

A Dissertation

Presented to

the faculty of the School of Engineering and Applied Science

University of Virginia

---

in partial fulfillment

of the requirements for the degree

Doctor of Philosophy

by

Sunil Unnikrishnan

December

2014

APPROVAL SHEET

The dissertation

is submitted in partial fulfillment of the requirements

for the degree of

Doctor of Philosophy

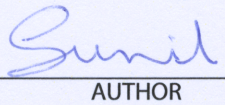

AUTHOR

The dissertation has been read and approved by the examining committee:

Alexander L. Klibanov

Advisor

Michael B. Lawrence

William H. Guilford

John A. Hossack

Richard J. Price

Accepted for the School of Engineering and Applied Science:

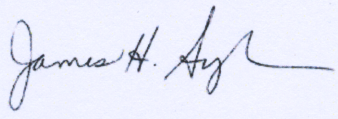

Dean, School of Engineering and Applied Science

December

2014

Abstract

Targeted microbubble ultrasound contrast agents are being widely studied for potential clinical targeting applications in molecular imaging and drug delivery. Local hemodynamics play a crucial role in microbubble binding to the vascular endothelium. Microbubble binding *in vivo* occurs at higher shear rates as compared to *in vitro* flow assays. The *in vitro* studies are typically conducted without red blood cells (RBCs) and do not account for the particulate nature of blood. The presence of RBCs has been shown to enhance the adhesion of leukocytes, microparticles, and platelets to the endothelium, but the role of RBC-microbubble interaction on microbubble adhesion dynamics is not fully understood. Disturbed flow is commonly found in the arterial system at bifurcations and pathological sites like stenoses. The effect of disturbed flow on microbubble adhesion has not previously been studied. The central hypothesis of the proposed work is that red blood cells and locally disturbed hemodynamics play a critical role in microbubble targeting to disease markers on the vascular endothelium. Rational design of microbubbles to improve targeting efficacy requires adequate understanding of microbubble adhesion dynamics in the vasculature.

The first part of this dissertation was conducted to assess the influence of red blood cells (RBCs) on microbubble targeting. Using fluorescent microscopy and ultrasound imaging, the binding of biotin and P-selectin antibody-conjugated microbubbles to streptavidin and murine P-selectin, respectively, was evaluated under dynamic flow conditions in a parallel-plate chamber. In the presence of RBCs (20% and 40% hematocrit), the adhesion efficiency of biotin microbubbles was enhanced relative to phosphate buffered-saline (PBS) at wall

shear rates (WSR) greater than 100 s^{-1}. An order-of-magnitude improvement in binding efficiency was observed at 450 s^{-1} and 40% hematocrit. At lower WSR, RBCs did not significantly alter binding. For P-selectin targeting at high antibody coating concentration (1.5 μg/10^7 microbubbles) and at high WSR (450 and 600 s^{-1}), the bound microbubble echo intensity was 40-50% greater when RBCs were present. In contrast, at low antibody concentration (0.075 μg/10^7 microbubbles), RBCs reduced microbubble targeting by 35-50% relative to PBS. A two-fold increase in P-selectin targeting was observed in the presence of RBCs in an *ex vivo* carotid artery flow assay was performed at the high antibody concentration. The effect of RBCs on microbubble detachment from P-selectin substrate was examined using a flow detachment assay. At low antibody concentration, half-maximal detachment occurred at 600 s^{-1} and 3900 s^{-1} with RBCs and PBS, respectively. At high concentration, half-maximal detachment occurred at 3300 s^{-1} when RBCs were present, while with PBS 60% of the bound microbubbles remained adherent even at WSR as high as 19200 s^{-1}. Overall, we demonstrate that RBCs affect microbubble targeting in a shear- and ligand concentration-dependent manner.

We hypothesized that localized microbubble adhesion would be promoted in vascular regions with disturbed flow, where recirculation and stagnation zones are present. In the second part of this dissertation, we tested this hypothesis by characterizing microbubble adhesion to streptavidin in a model of disturbed flow implemented using a backward-step flow expansion chamber. The flow separation at the step established a recirculation zone, a stagnation zone, and fully developed flow further downstream. Microbubble adhesion was augmented in the vicinity of the reattachment zone relative to the region far downstream under all tested flow conditions. At 1:2 expansion ratio (254 μm:508 μm), the peak

adhesion around the flow reattachment region, relative to far downstream, was greater at higher shear rates (4-fold at 700 s^{-1} vs 2-fold at 350 s^{-1}). With step expansion ratio of 1:3 (127 μm:381 μm), the peak adhesion in the region was enhanced 8-fold. The enhancement in local adhesion with RBCs was lower compared to that observed with plain buffer. Computational fluid dynamics simulations were performed to compute local velocities and wall shear rates. The presence of wall-directed normal velocity components along the flow path correlated with the regions of elevated binding, suggesting that convective transport towards the wall enhances microbubble adhesion.

Overall, we demonstrated that particulate nature of blood and locally disturbed hemodynamics play a critical role in microbubble targeting. These factors should be taken into account in the design of targeting strategies to optimize targeting efficacy in physiological conditions.

Table of Contents

List of figures

List of Tables

List of Abbreviations

apoE	Apolipoprotein E
BSA	Bovine serum albumin
CAM	Cell adhesion molecule
CEUS	Contrast-enhanced ultrasonography
CFD	Computational fluid dynamics
cP	centipoise
CPS	Contrast pulse sequence
DiI	Dioctadecyl-3,3,3',3'-tetramethylindocarbocyanine iodide
DSPE	Distearoylphosphatidylethanolamine
FDA	Food and Drug Administration
FOV	Field of view
g	Gravitational force
Hct	Hematocrit
HFD	High-fat diet
ICAM-1	Intercellular adhesion molecule – 1
IgG	Immunoglobulin
IL-1	Interleukin-1
IMT	Intima-media thickness
LDLr	Low density lipoprotein receptor
MI	Mechanical index
MHz	Megahertz
MRI	Magnetic resonance imaging
NO	Nitric oxide
NA	Numerical aperture
OD	Outer diameter
PBS	Phosphate buffered saline
PE	Polyethylene
PEG	Polyethylene glycol
PET	Positron emission tomography
pN	piconewton
PSGL-1	P-selectin glycoprotein ligand-1
ROI	Region of interest
rpm	Rotations per minute
RBC	Red blood cell
sle^a	Sialyl Lewis^a
SPECT	Single-photon emission computer tomography
TIRF	Total internal reflection fluorescence
TNF- α	Tumor necrosis factor-α
VCAM-1	Vascular cell adhesion molecule – 1
VEGFR2	Vascular endothelial growth factor receptor – 2
WSR	Wall shear rate
w/v	weight by volume

Chapter 1

Background and Significance

Ultrasound and Precision Medicine

Modern patient care is increasingly moving towards a paradigm of precision medicine. Under this concept, molecular information is obtained for a pathological state and interpreted alongside traditional clinical indices [1]. Treatment regimens can then be precisely designed for the individual. On the therapeutic side, targeted delivery systems that can deliver drugs locally and minimize systemic effects are desirable. On the diagnostic side, reliable quantitation of the relevant molecular profile is necessary. By enabling close examination of the underlying pathophysiology, molecular imaging allows, inter alia, early detection, improved monitoring of disease progression, and better risk stratification. Towards this end molecular imaging tools are increasingly being developed for diagnostic radiology.

All imaging modalities possess molecular imaging capabilities to varying extents [2]. Currently, radionuclide techniques like positron emission tomography (PET) and single-photon emission computed tomography (SPECT) are the modalities of choice in the clinical. They provide excellent sensitivity and specificity, but require costly equipment and expose the patient to ionizing radiation. Magnetic resonance imaging (MRI) is another promising modality, with particular strengths in terms of spatial resolution for anatomic imaging and functional imaging capabilities. But it is challenging to obtain real-time images with MRI. Moreover, MRI detection sensitivity is limited for molecular imaging. Ultrasound imaging is a safe, inexpensive, portable modality that allows real-time imaging. Molecular imaging can

be expanded to smaller clinics and mobile units with the help of ultrasound. Microbubbles are gas-filled, encapsulated microspheres that are used as ultrasound contrast agents for blood pool imaging. Site-targeted microbubbles have the potential to enhance the functional range of clinical ultrasound to include molecular imaging and targeted drug delivery [3, 4].

Microbubbles and Ultrasound

Microbubbles are intravascular contrast agents, typically 1-10 μm in size. The encapsulating shell in most formulations is lipid-based; protein- and polymer-based materials are used to a lesser extent. The gas inside is usually a heavy insoluble gas like perfluorocarbon or sulfur hexafluoride. Contrast in ultrasound imaging depends on the differences in acoustic impedance, which in turn depends on tissue properties like density and compressibility. Due to impedance mismatch at interfaces, the incident sound wave is reflected and scattered. For structures smaller than the wavelength of the sound wave, for e.g. microbubbles, the latter mechanism is dominant. Due to the high compressibility of the gas compared to the surrounding medium, microbubbles scatter ultrasound efficiently and provide excellent contrast. They resonate and undergo volume oscillations at clinical diagnostic frequencies (1-15 MHz) and the resulting backscatter acoustic signal is then detected. Microbubbles can be detected by ultrasound with exquisite sensitivity: individual bubbles can be detected [5]. Additionally, microbubble detection techniques, like phase and amplitude modulation, which take advantage of the non-linear oscillatory behavior of microbubbles, have been particularly effective in suppressing background tissue signal and improving detection sensitivity [6, 7]. Microbubbles are administered intravenously and

circulate in the bloodstream for several minutes. Ultrasound imaging is performed during this period. The clearance of bubbles occurs primarily through the liver and spleen, while the gas is exhaled via the lungs.

Microbubbles are generally considered safe and have been approved for use by the Food and Drug Administration (FDA). Contrast-enhanced ultrasonography (CEUS) is used in echocardiography for left ventricular opacification (thus improving endocardial surface delineation) [8], and in hepatology for detecting liver lesions (outside the United States). Furthermore, there is clinical potential for assessing organ perfusion using microbubbles. This relies on two important characteristics associated with microbubbles. First, microbubble rheology is similar to that of RBCs in the microvasculature [9, 10]. Second, microbubbles can be destroyed with high intensity acoustic pulses. To assess perfusion, microbubbles are first destroyed in the region of interrogation. The refilling process of the microbubbles is imaged and the blood flow rate is quantified from the replenishment kinetics [11].

Targeted Microbubbles

Microbubbles can be targeted to relevant sites in the body for the purpose of imaging or drug delivery. The typical target is a cell surface protein or glycoprotein that is upregulated during disease. Suitable ligands have to be conjugated to the bubble shell to enable targeting to the cell receptors. Antibodies, antibody fragments, peptides, and carbohydrates have been coupled to the microbubble surface via several linking schemes [3, 12]. A schematic of antibody-conjugated microbubble is shown in Fig. 1.1. The ligands should have adequate specificity and affinity for the molecular markers, allowing binding and

retention of bubbles to the endothelium under physiologic flow conditions (Fig. 1.2). Microbubble accumulation permits visualization and quantitation of the biomarker pattern at pathological sites. The monitoring of the disease from its early stages becomes feasible. The effects of therapeutic intervention can also be better evaluated with the help of molecular imaging.

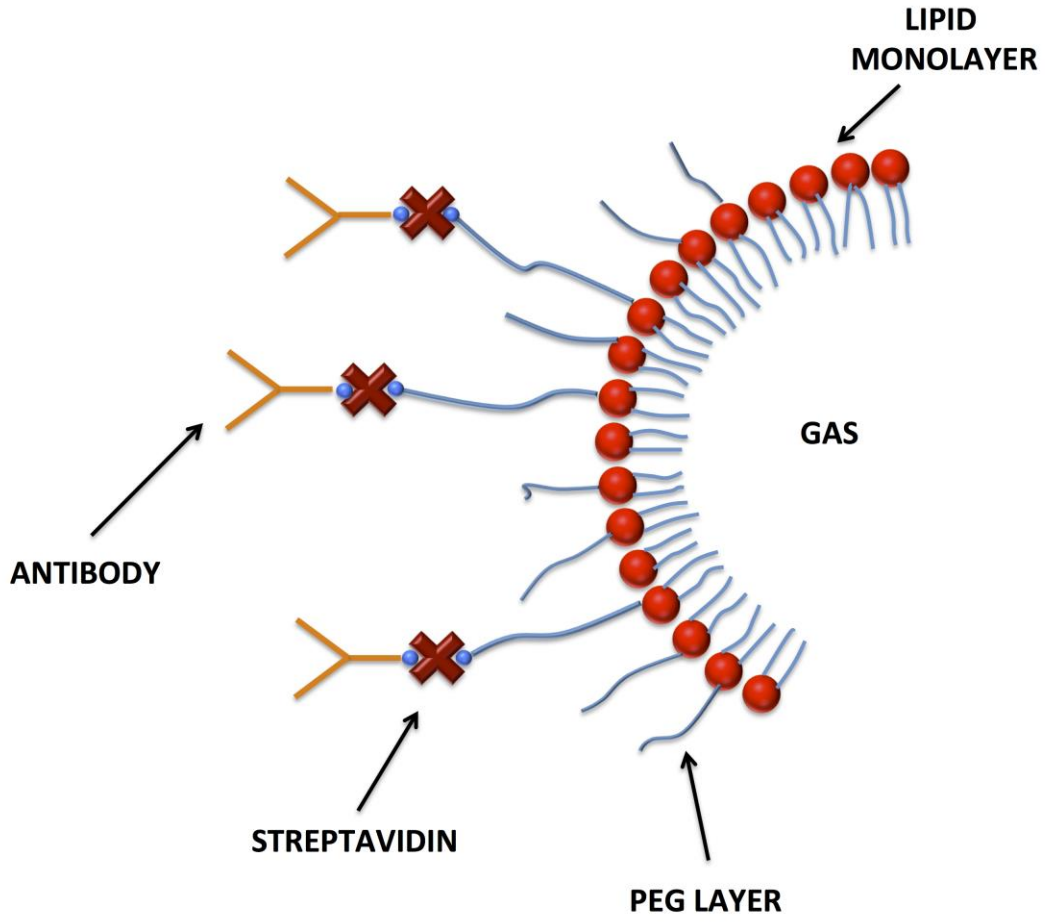

Fig. 1.1: Schematic of antibody-conjugated lipid-shelled microbubble. Streptavidin linker attaches biotinylated antibody to microbubble. Polyethylene glycol (PEG) polymer inhibits coalescence and increases stability of microbubbles. Figure adapted from [12].

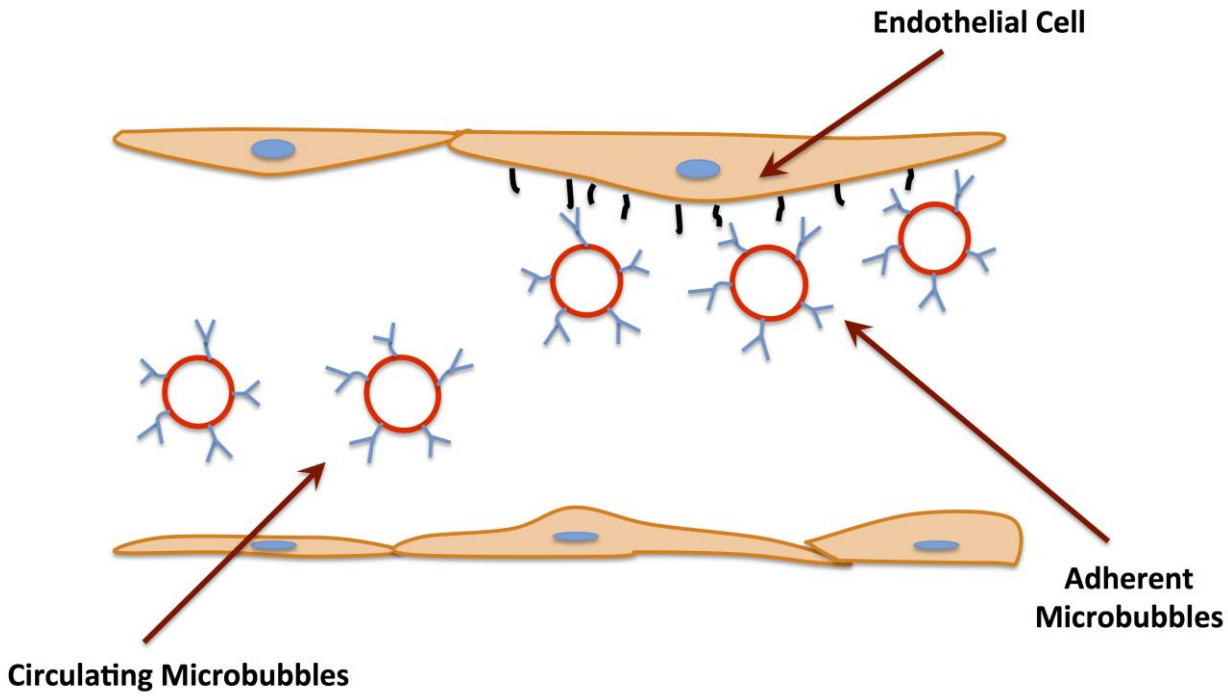

Fig. 1.2: Microbubble targeting to disease markers on the vascular endothelium

Inflammation, angiogenesis, and thrombus markers have been targeted using microbubbles. Inflammation markers (for e.g. VCAM-1, ICAM-1, P-selectin) are routinely overexpressed at sites of atherosclerosis, ischemia-reperfusion injury, and inflammatory bowel disease. In animal models of these diseases antibody-coupled microbubbles have been used to image inflammation [13-18]. Angiogenesis markers VEGFR-2 and $\alpha_v\beta_3$ integrin on the tumor neovasculature have been successfully targeted in pre-clinical studies [19-23]. Furthermore, BR-55 (Bracco Inc., Geneva, Switzerland), a commercial microbubble formulation targeting VEGFR-2, has undergone successful early stage (phase 0) clinical testing in prostate cancer patients [24]. Clot imaging is important in cases of stroke and myocardial infarction. Thrombus-specific microbubbles that bind to glycoprotein IIb/IIIa integrins on activated platelets have been developed for this purpose

[25-27]. In addition to imaging, high acoustic power destruction of the microbubbles in proximity to the clot can be used to lyse it as well.

Rational design of microbubbles to improve targeting efficacy requires adequate understanding of microbubble adhesion dynamics in the vasculature. The adhesion of targeted microbubbles to the vasculature is mediated by specific non-covalent receptor-ligand interactions. Local hydrodynamics play an important role in these adhesive interactions. Microbubble binding occurs *in vivo* at higher shear rates as compared to *in vitro* flow chamber studies. This discrepancy highlights shortcomings in our understanding of the factors affecting the targeting process in physiologic settings. The particulate nature of blood is typically not taken into consideration in the *in vitro* flow assays. Red blood cells (RBCs) are known to enhance adhesion of leukocytes [28-30], microparticles [31, 32], and platelets [33, 34] to the endothelium, but their influence on microbubble adhesion dynamics has not been fully elucidated.

In certain regions of the arterial tree blood flow is characterized by the existence of recirculation patterns. These regions of so-called 'disturbed' hemodynamics occur at bifurcations, like the carotid bifurcation, and at curvatures, like the aortic arch. The sites are often associated with endothelial dysfunction and atheroma formation. Vortex formation in flow occurs downstream of stenosed regions as well. Hence these locations are prime targets for diagnostic imaging and therapeutic interventions. It has been reported that disturbed flow promotes the adhesion of leukocytes and platelets to the endothelium, but the effect of these altered flow conditions on microbubble targeting has not been investigated.

Aims and Outline of the Study

The central hypothesis of this study is that the particulate nature of blood and locally disturbed hemodynamics play a critical role in microbubble targeting to molecular markers in the vasculature. In chapter 2 of the dissertation, we present our work evaluating the influence of RBCs on microbubble targeting *in vitro* and *ex vivo*. Chapter 3 focuses on the effects of recirculating flow on microbubble adhesion, examined using a backward step flow chamber.

Chapter 2

Red Blood Cells and Microbubble Targeting

Introduction

Effective microbubble targeting requires delivery of the agent to the vessel wall and the subsequent formation of bonds to ensure firm adhesion and retention. The factors that have a direct bearing on targeting include the microbubble concentration near the wall, density of receptors and ligands, the length of the interacting molecules, the kinetics of the reaction, and the local flow environment. Hemodynamic factors play a major role in limiting the targeting efficacy of microbubbles. Microbubble concentration profile in the vessel cross-section has been reported to be similar to RBCs, i.e. lower in the near-wall region compared to the center of the vessel [9, 10]. This limits the delivery of microbubbles to the near-wall region, where binding interactions with the endothelium occur. Furthermore, hemodynamic conditions vary substantially in the vasculature, with large differences in shear rates and hematocrit. Microbubbles should have the ability to bind efficiently under diverse conditions. But at higher shear rates and shear stresses, due to the limited time available for bond formation and higher disruptive stresses on bonds, adhesion is typically lower than at low shear conditions.

These limitations have spurred the development of several strategies to improve microbubble targeting. Acoustic radiation force has been used to push microbubbles towards the vessel wall and enhance their near-wall concentration, while simultaneously increasing their contact time with the endothelium. Innovative ligand-based strategies, inspired by the example of leukocyte adhesion during inflammation, have been

implemented to partially overcome the effect of high shear rates [35, 36]. But our understanding of the targeting process *in vivo* remains incomplete. In flow chamber studies, antibody-conjugated microbubbles were found to bind efficiently only up to 150 s^{-1} [37]. In contrast, *in vivo* in the microvasculature the same microbubbles can bind at higher shear rates, up to 1500 s^{-1} [16]. Successful microbubble targeting has also been reported in large arteries with high flow rates, such as the aortic arch, in mouse models of atherosclerosis [13, 14]. One possible difference between the *in vivo* and *in vitro* tests is the respective presence or absence of cells: the *in vitro* assays are typically performed in plain buffer without red blood cells (RBCs). They are thus limited in their ability to replicate the hemodynamic environment, both in normal physiology and in pathological conditions. Physical interactions with RBCs have been known to enhance leukocyte, platelet, and microparticle adhesion to the vessel wall. RBC-microbubble interactions could be playing a critical role in microbubble targeting as well, but this remains relatively unexplored. It is only quite recently that groups have started paying attention to the role of RBCs in microbubble targeting [38].

RBCs and Adhesion Dynamics of Leukocytes, Platelets and Microparticles

RBCs are biconcave, high deformable, non-nucleated cells, roughly 8 μm in diameter and 2 μm in thickness. They form the largest particulate fraction of blood, comprising about 40-45% by volume. Thus, they strongly influence fluid properties, like viscosity, and their collective behavior accounts for several features observed in the vasculature. For e.g. the radial migration of RBCs towards the vessel axis leads to the formation of the plasma layer near the wall, which is a spatially and temporally varying RBC-free fluid layer [39]. Furthermore, in flowing concentrated suspensions like blood, cells are constantly colliding

against one another. Seminal studies by Goldsmith et al. have demonstrated that the motions of individual RBCs exhibit irregular fluctuations under flow at physiologic hematocrit [40]. For cells, like leukocytes and platelets, and intravascular agents, like microparticles and microbubbles, these mechanical interactions with RBCs are an inescapable aspect of the local hemodynamic environment [41, 42]. In the near-wall regions, these interactions with RBCs can have an impact on adhesion to the wall.

Several studies have shown the importance of local flow conditions and blood rheological parameters on adhesion to the endothelium. Munn et al. and Abbitt et al. showed that at low shear rates (< 150 s^{-1}) leukocyte adhesion increased with increasing hematocrit up to 30% and then remained constant from 30% to 60% [29, 43]. The increase in adhesion was already apparent at a low hematocrit of 5%. Additionally, Melder et al. observed that augmentation of binding in the presence of RBCs was especially pronounced at shear rates greater than 400 s^{-1}, where no binding was seen in the absence of RBCs [28]. There was no concomitant increase in the near-wall concentration of leukocytes, but the enhancement in binding was associated with an order-of-magnitude increase in leukocyte collision frequency with the wall as well as larger leukocyte velocity fluctuations. This suggested that RBC collisions with leukocytes contribute additional forces that tend to aid adhesion. It was proposed that the wall-directed normal force component resulting from these collisions would have a pro-adhesive effect by increasing the contact frequency and/or by enhancing the efficiency of each wall interaction in producing firm adhesion to the vessel.

RBCs also enhance platelet and microparticle adhesion [32, 33]. Platelets accumulate in the near-wall region of the vessel [44, 45] and this 'near-wall excess' increases with hematocrit and shear rate [44, 46]. The enhanced platelet concentration near the wall is linked to the

lateral migration of RBCs towards the center of the vessel [34], although the details of the mechanism are unclear and remain a subject of vigorous research [47-50]. Moreover, the near-wall excess is only a partial contributor to the observed increase in platelet adhesion and other factors, like near-wall collisions with RBCs [51], play a key role. Recent computational studies have also shed light on the role of RBC mechanical interactions on thrombus growth. Collisions with RBCs tend to restrict the vertical growth of platelet aggregates towards the center of the vessel, limiting the height to which thrombus could grow [52, 53]. They also caused thrombi to persistently roll along the wall [53].

The above-mentioned works suggest that RBCs under flow can affect adhesive interactions in myriad ways. In the context of microbubble targeting, the role of RBCs has not yet been analyzed. In this study, we investigated the influence of RBCs on microbubble targeting. In a flow chamber setting, we examined microbubble binding to streptavidin and to P-selectin using biotin and monoclonal P-selectin antibody ligands, respectively. Biotin-streptavidin interaction is the strongest known non-covalent biological interaction and is a good model for binding studies. P-selectin is a transmembrane glycoprotein that is expressed on activated endothelial cells [54] and supports leukocyte rolling during inflammation [55]. It is a reliable marker for molecular imaging of inflammation. We conducted detachment studies to understand the effect of RBCs on microbubble retention under flow. Furthermore, we implemented an *ex vivo* flow assay to assess the influence of RBCs on targeting to the vasculature.

Materials and Methods

Preparation of microbubbles and RBC suspensions

Biotinylated microbubbles were manufactured from decafluorobutane gas (F2 Chemicals, Lancashier, UK) coated with a lipid monolayer shell comprised of phosphatidylcholine (Avanti Lipids, Alabaster, AL), polyethylene glycol stearate (PEG stearate, Stepan Kessco, Northfield, IL) and biotin-PEG3400-distearoylphosphatidylethanolamine (biotin-PEG-DSPE, Shearwater Polymers, Huntsville, AL). When needed, a trace amount (<1%) of 1,1'-Dioctadecyl-3,3,3',3'-tetramethylindocarbocyanine iodide (DiI, excitation peak – 550 nm, emission peak – 570 nm) was added to the lipid mixture as a fluorescence microscopy label. The preparation was via a standard aqueous saline lipid micellar dispersion sonication procedure [56]. After completion of the formulation, the microbubble dispersion was, placed in a glass vial, sealed under decafluorobutane atmosphere, and stored at 4 °C. Prior to use, free unincorporated lipid micelles, biotin-lipid and dye were removed from the microbubble solution by repeated centrifugal flotation (140 g, 10 min) in degassed phosphate buffered saline (PBS) containing 0.25% bovine serum albumin (BSA, Sigma-Aldrich, St. Louis, MO).

Biotinylated microbubbles were used for targeting to streptavidin-coated surface. For P-selectin targeting, biotinylated monoclonal antibody RB40.34 (BD Biosciences, San Jose, CA) was conjugated to the microbubbles using streptavidin. After the initial centrifugation steps described above, the biotinylated microbubbles were counted using a Coulter Multisizer 3 (Beckman Coulter, Brea, CA). Streptavidin (Anaspec, Fremont, CA) was added to the microbubble dispersion at a concentration of 3 μg/10^7 microbubbles and incubated

for 10 min at room temperature. The microbubbles were gently agitated every 2 minutes to ensure mixing. This dispersion was washed two times to remove the excess streptavidin and counted again. Next, the biotinylated antibody or oligosaccharide was added to the microbubbles at the specified concentration and incubated for 10 min. Two more washing steps were performed to remove the excess antibody (or oligosaccharide). Microbubble count and size distribution was acquired before each experiment. The mean microbubble diameter was 2.1 μm (standard deviation = 0.9 μm) and 98% of the microbubbles were less than 6 μm in diameter.

Citrated bovine whole blood was obtained from Hemostat Inc, Dixon, CA. Washed RBC suspensions were used because leukocytes and platelets present in whole blood would possibly adhere to the target and may mask the biomechanical effects of RBCs. Whole blood was centrifuged at 500g for 20 min to remove plasma and buffy coat. The RBCs were washed with PBS 3 more times and were suspended in PBS at the desired hematocrit (Hct). Additionally, to evaluate the effect of RBC deformability on microbubble adhesion fixed non-deformable cells were prepared using glutaraldehyde [57]. Washed and packed RBCs (20 ml) were added drop by drop to 0.0125% glutaraldehyde in PBS (400 ml) and incubated for 30 min at room temperature. The hardened cells were washed three more times in PBS and suspended at 40% hematocrit. Furthermore, to control for the effect of viscosity on targeting, a higher viscosity (~ 3 cP) solution was prepared by dissolving PEG 4000 (Sigma-Aldrich, St. Louis, MO) in PBS (10% w/v).

Microbubble targeting in a parallel plate flow chamber

The microbubble adhesion and detachment studies were carried out using a parallel-plate flow chamber (Glycotech Inc., Gaithersburg, MD) with custom modifications [36]. A silicon rubber gasket established the dimensions of the flow channel. The channel height was 0.127 mm (set by gasket thickness) and the width was 2.5 mm. The gasket was affixed to a circular acrylic flow deck with inlet and outlet ports. Finally, the protein-adsorbed tissue culture dishes (35 mm) were mounted onto the deck before each flow experiment. A syringe pump (Harvard Apparatus Inc., Holliston, MA) operated in withdrawal mode was used to draw microbubbles through the chamber. The wall shear rate (WSR) was manipulated by adjusting the pump flow rate. The WSR for viscous flow between parallel plates is computed by the following formula: $6Q/bh^2$, where Q is the flow rate (cm^3/s), 'b' is width of the channel (cm), and 'h' is height of the channel (cm).

Streptavidin or murine P-selectin (BD Biosciences, San Jose, CA) was adsorbed on 35 mm tissue culture dishes (Corning Inc., NY). PBS droplets (200 µl) containing the protein at the specified concentration were placed on the dish and covered with plastic cover slips (22 X 22 mm) [36]. After overnight incubation at 4 °C, the dishes were washed with PBS and blocked with 1.5% BSA in PBS for at least 4 hours at room temperature to minimize non-specific adhesion of microbubbles.

Microbubble Binding Study using Fluorescence Microscopy

Targeting of biotinylated microbubbles to streptavidin-coated surface was assessed by fluorescence microscopy. The experimental set-up is shown in Fig. 1.3. A schematic of the flow assay and the flow path is shown in Fig. 1.4 and Fig. 1.5, respectively. Streptavidin at

concentration 10 μg/ml was adsorbed on the dishes. Microbubbles were diluted to 5 $\times 10^6$/ml in PBS and introduced into the flow chamber at shear rates ranging from 50 to 450 s^{-1}. Experiments were conducted in two configurations: upright, where buoyancy drives the bubble towards the reactive surface, and inverted, where buoyancy drives it away from the reactive substrate. The chamber was imaged with a 40X water immersion objective (Zeiss, Thornwood, NY) for upright experiments. For the inverted experiments, the chamber was simply flipped and imaged with a long working distance 40X dry lens (Olympus America, Center Valley, PA) on an inverted microscope. To assess whether RBCs affect microbubble interaction with the wall at low site densities, another set of experiments were conducted in the upright mode with streptavidin adsorbed at lower concentration (0.5 μg/ml) and at WSR of 450 s^{-1}.

Video microscopy was performed for 2 minutes using a standard NTSC camera. The images were then exported to a PC and analyzed off-line. The observation area was 105 μm X 140 μm. The number of adherent microbubbles in the field-of-view (FOV) was counted. A microbubble was considered to be adherent if it remained bound to the surface for 5 seconds or more [58]. The adhesion efficiency was computed by normalizing the number of adherent bubbles to the near-wall flux of bubbles. The near-wall flux was quantified as the number of bubbles that flowed near the chamber surface, detected by video microscopy. The depth of the near-wall region was estimated to be ~10 μm based on the velocity of microbubbles. From a subset of the experimental runs, we also collected the velocities of individual microbubbles immediately before they bound.

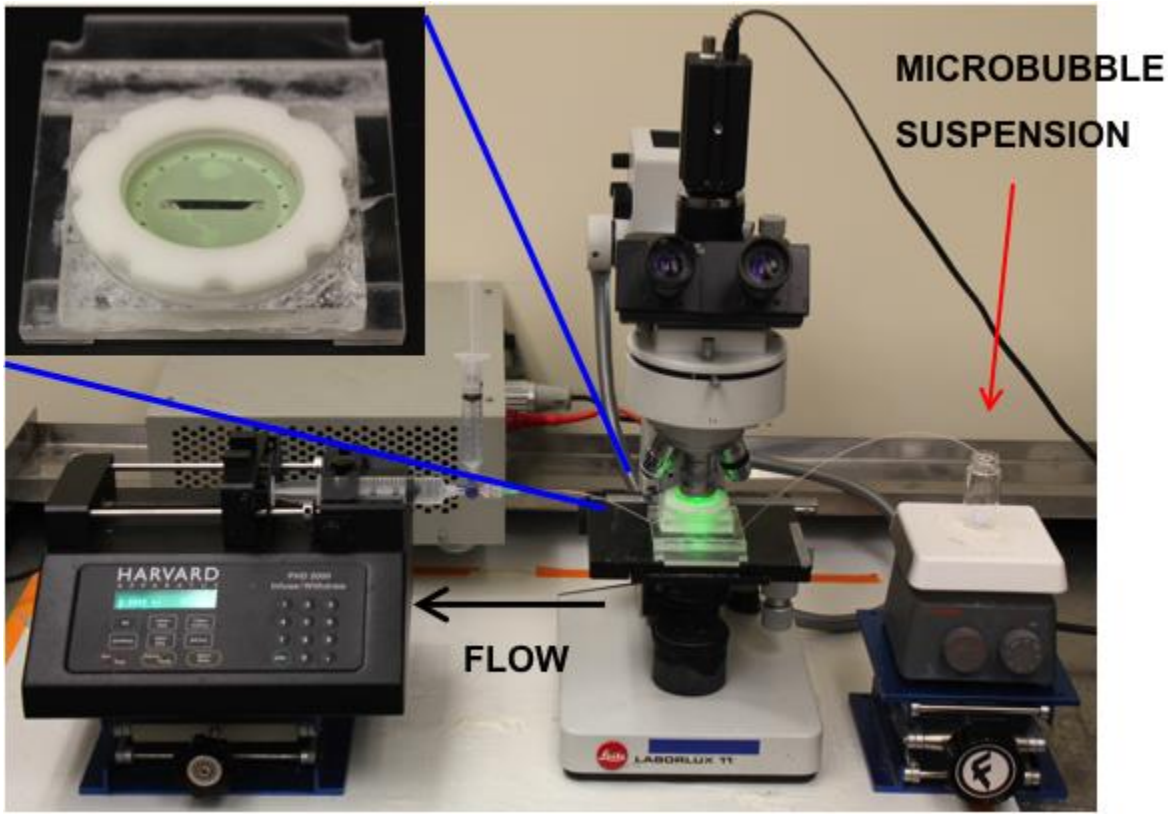

Fig. 1.3: Experimental set-up for assessing microbubble adhesion using fluorescence microscopy. Inset: Flow chamber.

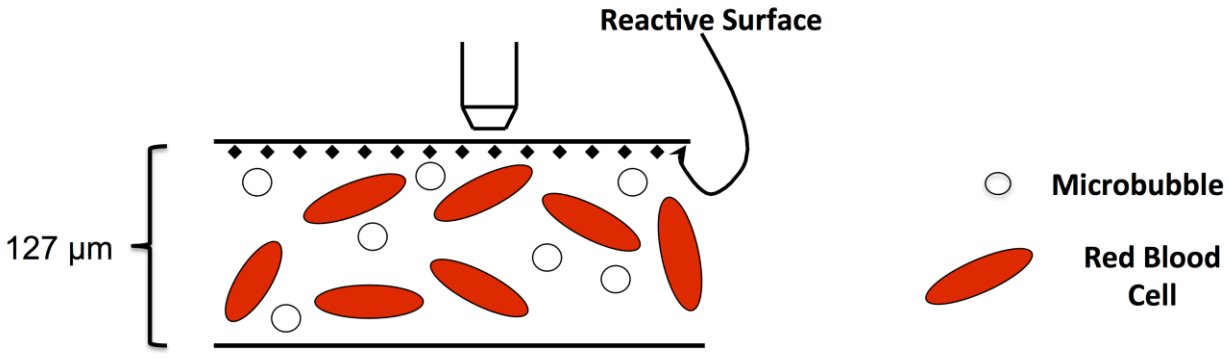

Fig. 1.4: Schematic representation of the flow assay with microbubbles and RBCs

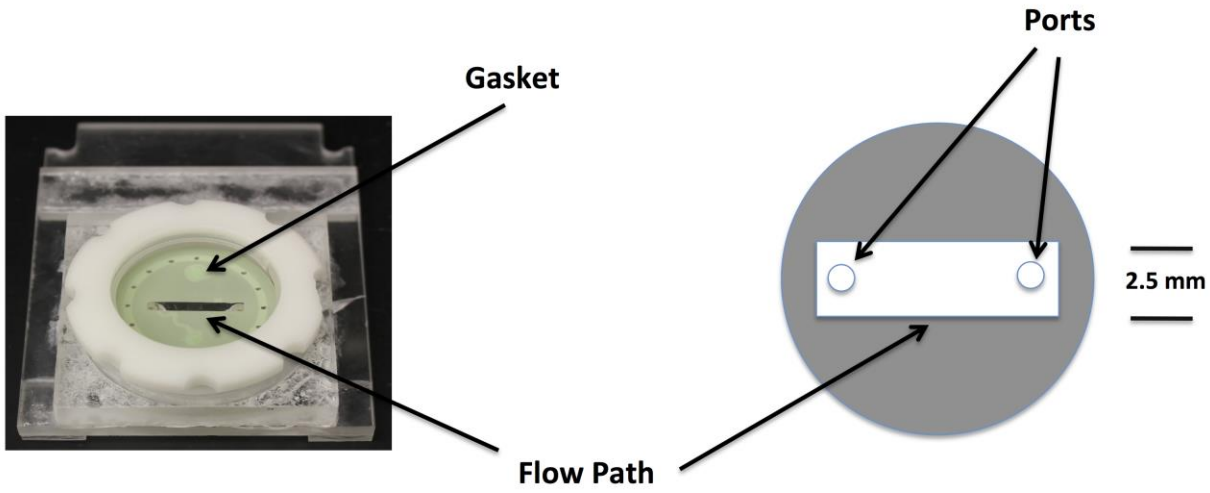

Fig. 1.5: Flow chamber image and schematic representation of the flow path

Microbubble Binding Study using Ultrasound Imaging

In the flow chamber experiments evaluating P-selectin targeting, binding of antibody-decorated microbubbles was assessed using ultrasound imaging [59]. Microbubble binding along the entire flow path can be imaged with ultrasound. A schematic of the experimental set-up is shown in Fig. 4. In these experiments, only fast flows, with high wall shear rates (> 150 s^{-1}), were tested. P-selectin at concentration 3 μg/ml was adsorbed on the culture dish as described above. The ligand density on the microbubbles was modified in these experiments by conjugating different amounts of biotinylated antibody (RB40.34, monoclonal rat anti-mouse P-selectin antibody). The antibodies were added at concentrations of 1.5 μg per 10^7 microbubbles (high ligand density) and 0.075 μg per 10^7 microbubbles (low ligand density). These correspond to ~10^5 and ~10^4 [16, 36] antibody molecules per microbubble, respectively. Ultrasound imaging experiments were also

carried with microbubbles conjugated to the fast-binding ligand sialyl Lewis^a (sLe^a). Sialyl Lewis^a is a carbohydrate moiety on P-selectin glycoprotein ligand-1 (PSGL-1) molecule found on leukocyte microvilli and is known to interact with all three selectins [60]. It is characterized by fast on- and off-rates for its reaction with P-selectin; the kinetics of its interaction with P-selectin are distinct from antibody-antigen interaction. Selectin targeting at high WSR using microbubbles has been shown to be feasible using sialyl Lewis^x, an isomer of sLe^a [35]. For our experiments, a multivalent polymeric form of the molecule, sLe^a-PAA-biotin (Glycotech, Gaithersburg, MD) was conjugated to the microbubbles at 1 μg per 10^7 microbubbles [35].

The flow chamber was completely immersed in a shallow water bath to ensure acoustic coupling with the transducer (Fig. 1.6). The transducer was positioned so that the entire length of flow channel, from the entrance to the outlet, could be visualized. Imaging was performed using a Siemens Acuson Sequoia 512 system (15L8 transducer, Contrast Pulse Sequencing mode, 7MHz, Mechanical Index (MI) = 0.18). Microbubbles (reservoir concentration = 5×10^5/ml) were drawn through the chamber for 2 minutes. For each shear flow condition, the chamber was perfused with microbubble dispersions in PBS or RBCs (Hct ~ 40%) in random order. The chamber was subsequently flushed with PBS to remove unbound bubbles from the flow channel. At the end of each run, to obtain the background image, the MI was increased to 1.9 to destroy the adherent bubbles in the field of view. Echo images were collected and imported into ImageJ (NIH, Bethesda, MD) for offline analysis. After subtraction of the background image, a region-of-interest (ROI) was selected that excluded the inlet and outlet portions of the chamber; the echo intensity was subsequently quantified.

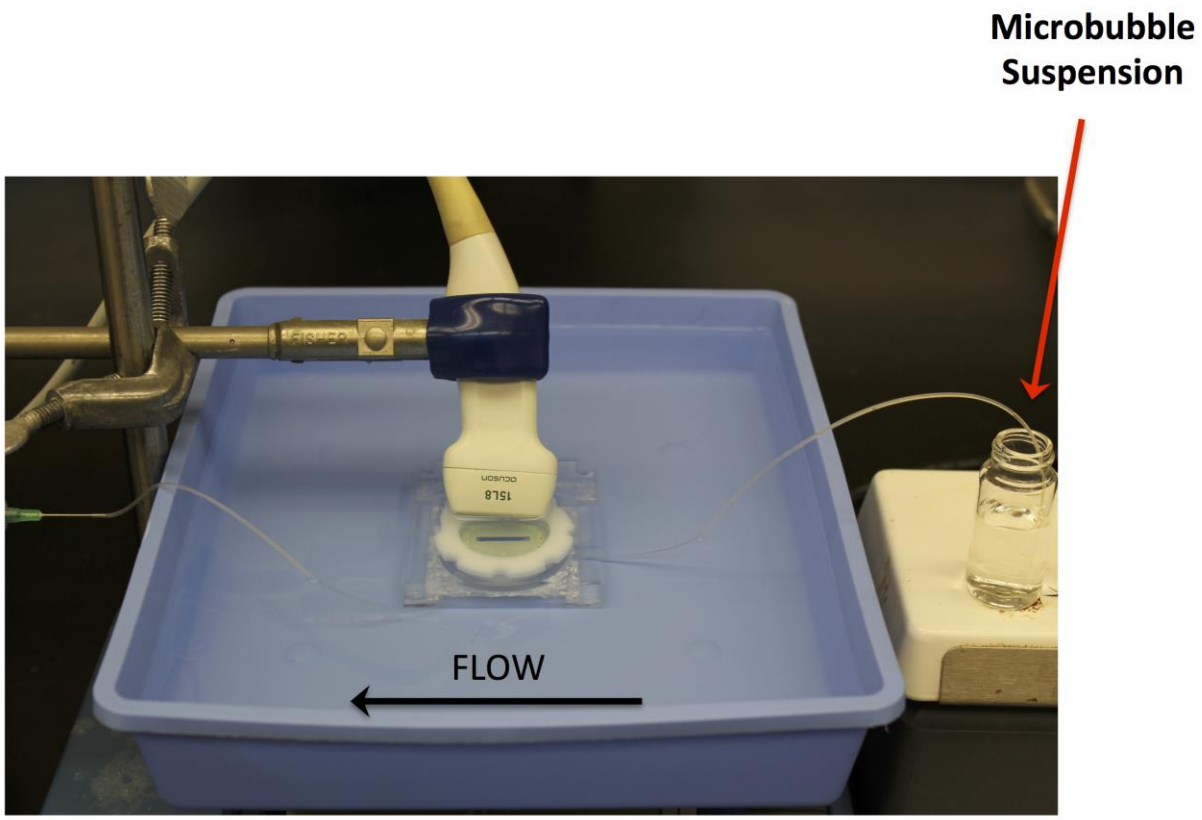

Fig. 1.6: Experimental set-up for assessing microbubble adhesion using ultrasound imaging

Detachment of targeted microbubbles from a P-selectin-coated surface

A microbubble detachment flow assay was performed to examine the effect of RBCs on the retention of bound microbubbles. The P-selectin substrate was generated as described above. Microbubbles with high and low surface density of antibodies were tested in the presence and absence of RBCs. Fluorescent diI carrying microbubbles were imaged using a 40X water immersion lens. The microbubbles were diluted to 20×10^6/ml in PBS and drawn into the parallel plate flow chamber. They were allowed to bind under static condition for 3 minutes. Unbound bubbles were washed away at 50 s^{-1} and the number of bound microbubbles under static conditions was recorded. The WSR was then increased to

300 s^{-1} and doubled every 30 seconds up to a shear rate of 19200 s^{-1}. Microbubble detachment was evaluated by computing the fraction of microbubbles remaining bound at the end of the each shear rate condition's time interval.

P-selectin microbubble targeting *ex vivo*

We evaluated the effect of RBCs on microbubble targeting in an *ex vivo* model with strong physiological relevance: an inflamed mouse carotid artery. P-selectin upregulation was induced by combined intravenous and local tissue administration of tumor necrosis factor-α (TNF-α, Sigma-Aldrich, St. Louis, MO) to C57BL/6 mice (0.5 μg/mouse, 2-3 hours prior to euthanasia). Euthanasia was performed by ketamine overdose, in accordance with the animal study protocol approved by the institutional Animal Care and Use Committee. The common carotid artery was excised immediately after euthanasia, flushed with PBS, and cannulated using PE-10 tubing (OD = 0.61 mm, Becton Dickinson and Company, Sparks, MD). The vessel was allowed to equilibrate in Krebs solution for 30 min and was maintained at 37 °C throughout the course of the experiment.

Microbubble targeting to the vessel wall was evaluated with ultrasound imaging. *Ex vivo* studies were performed only with the higher ligand density microbubbles. Microbubbles (5 × 10^5/ml) were perfused for 2 min (flow rate = 0.5 ml/min). The WSR was computed to be ~ 400-650 s^{-1}, depending on the vessel diameter. As compared to the *in vitro* study, the imaging for the *ex vivo* work was performed at a higher ultrasound frequency of 14 MHz (Sequoia 512, 15L8 transducer, CPS mode). This enables the acquisition of higher resolution images. During the perfusion of microbubbles the mechanical index (MI) was kept at 0.06 to minimize microbubble detachment from top of the vessel and accumulation

at the bottom due to the acoustic radiation force action. The vessel was flushed with PBS to remove free bubbles from the lumen and the MI was increased to 0.2 to image the bound microbubbles. Every vessel was perfused with microbubble dispersions in PBS or RBCs (Hct 40%) in random order. Isotype-matched nonspecific IgG-conjugated microbubbles (BD Biosciences, San Jose, CA) were used as controls. Following the completion of the binding and imaging stages, microbubbles were destroyed to obtain the background signal. Image collection and analysis was carried out similar to the *in vitro* ultrasound experiments described above.

Flow chamber particle trajectory monitoring with total internal reflection fluorescence (TIRF) microscopy

Total internal reflection fluorescence (TIRF) microscopy is used to observe events in close vicinity of a surface (<200-250 nm distance from the surface) with low background contributions from out-of-focus regions. Briefly, in TIRF microscopy an evanescent light wave is generated at the interface between two media with different refractive indices. The evanescent wave front radiates into the lower refractive index medium and the intensity of the wave decays exponentially, thus illuminating only a small region (Fig. 1.7).

The TIRF experiments were conducted using a parallel-plate flow chamber with a thin plastic wall (μ-slide $I^{0.2}$ Luer ibiTreat, IBIDI GmbH, Muenchen, Germany). The chamber wall thickness was 180 μm and the refractive index was 1.52 (manufacturer specifications). This is comparable to No. 1.5 standard glass coverslips typically used in TIRF experiments. The channel height was 200 μm. The flow experiments were conducted with non-targeted polystyrene beads to observe the effect of flowing RBCs on near-wall particle trajectories,

in comparison with PBS-only particle dispersion. To obtain sufficient signal for TIRF fluorescence microscopy, 3 μm fluorescent polystyrene beads (Duke Scientific, excitation – 542 nm, emission – 612 nm) were used for the flow experiments. Imaging was performed with 60X oil-immersion lens (NA = 1.45). The camera exposure time was 1 s. The flow rate was adjusted to obtain a shear rate of 300 s^{-1}.

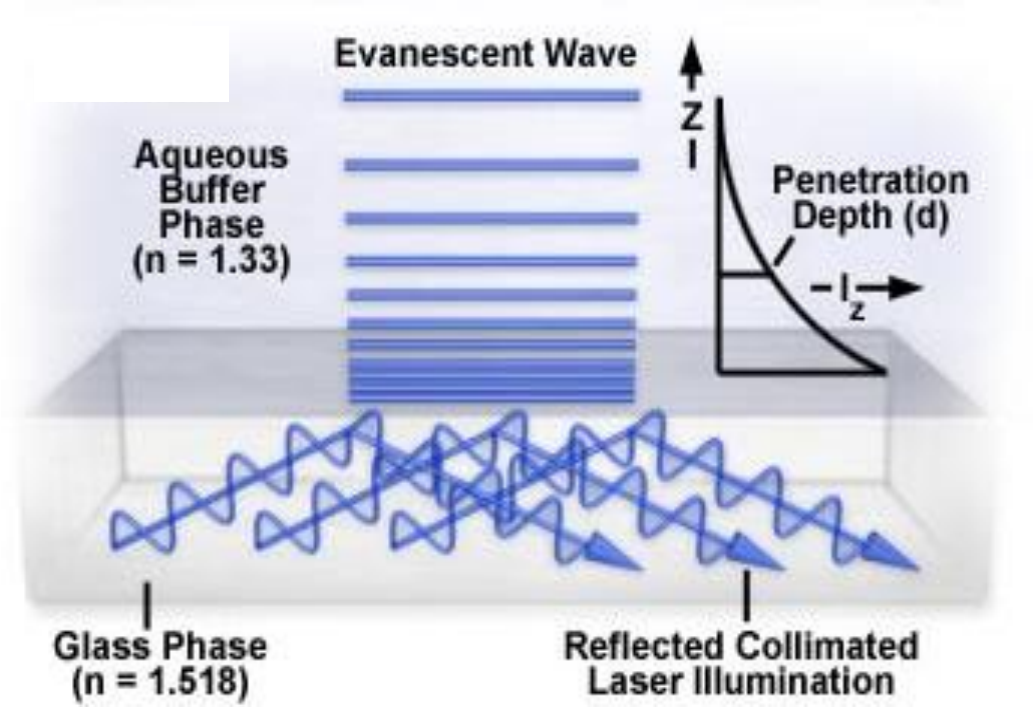

Fig. 1.7: Principle of TIRF microscopy (Source: Olympus Microscopy Resource Center website. http://www.olympusmicro.com)

Statistical Analysis

Student's 2-tailed t-test was used to calculate the p-value for all experimental data and $p < 0.05$ was assumed as the level of significance.

Results

Targeting of biotinylated microbubbles to streptavidin

In the upright configuration of the flow chamber buoyancy is responsible for bringing bubbles towards the reactive surface. Binding to streptavidin-coated surface was assessed for a range of shear rates and with (or without) the presence of RBC suspensions at different hematocrits. The targeted microbubble adhesion efficiencies for different RBC suspensions are shown in Fig. 1.8. At low flow, no difference in adhesion efficiency was seen between PBS and RBC suspensions. At higher shear rates, ≥ 150 s^{-1}, the binding efficiency was significantly higher in the case of RBC suspensions. This difference was particularly notable at 40% hematocrit with normal RBCs, where more than an order of magnitude increase was observed at 450 s^{-1} (0.22% for PBS vs 15.5% for RBCs). Modifying the RBC deformability had no effect on microbubble binding compared to normal RBCs. Adhesion efficiencies of microbubbles dispersed in high viscosity PEG solution was lower than those in RBC suspensions at all shear rates, but similar to microbubbles in PBS. Near-wall flux values for our studies in the upright configuration are presented in Fig. 1.9. At low shear rates, no significant difference between fluxes was seen between the suspensions, but at higher shear rates of 300 and 450 s^{-1}, the observed flux in the PBS case was higher than in RBC dispersions.

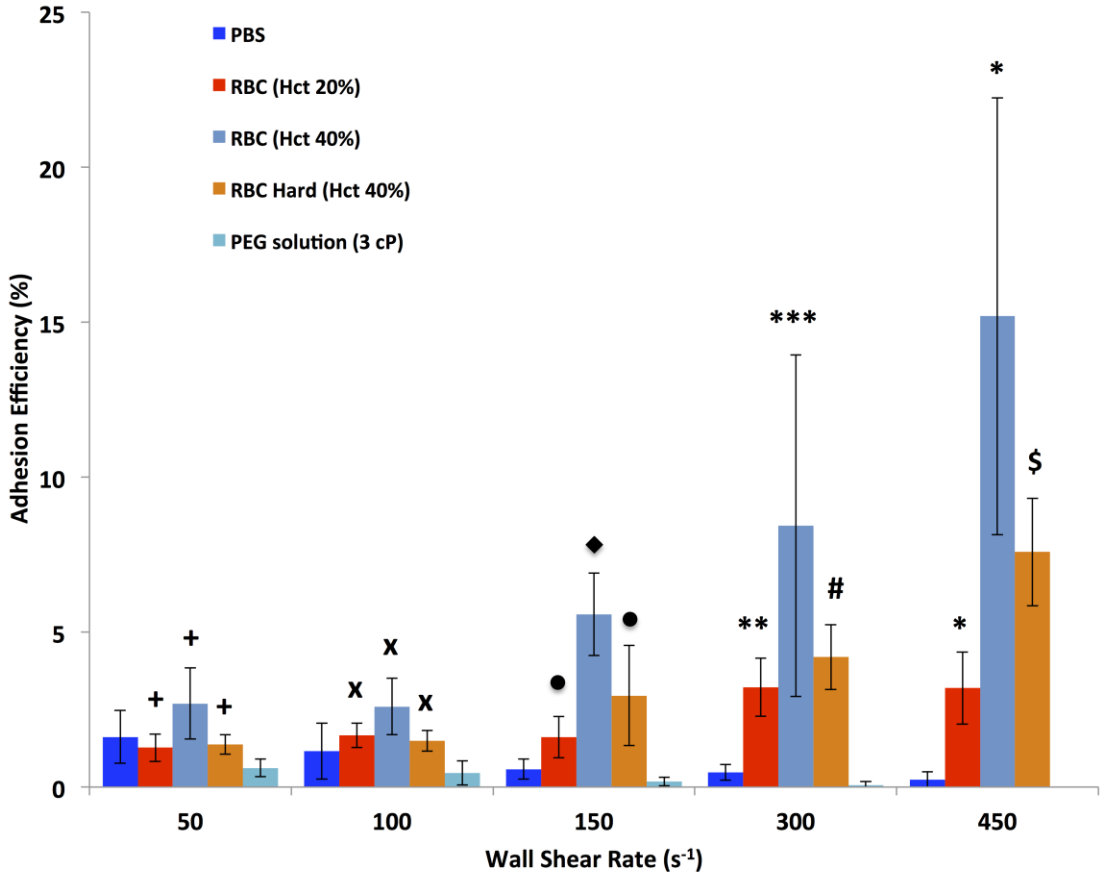

Fig. 1.8: Adhesion efficiency of biotinylated microbubbles targeted to streptavidin (10 µg/ml) in the upright configuration assessed by fluorescent microscopy. Values are mean ± SD (n = 3-5). +$p < 0.05$ vs. PEG solution. x $p < 0.01$ vs. PEG solution. •$p < 0.02$, ◆$p < 0.0002$ vs. PBS and PEG solution at 150 s^{-1}. ***$p < 0.05$, **$p < 0.005$, #$p < 0.002$ vs. PBS and PEG solution at 300 s^{-1}. \$$p < 0.001$, *$p$ <0.02 vs. PBS at 450 s^{-1}.

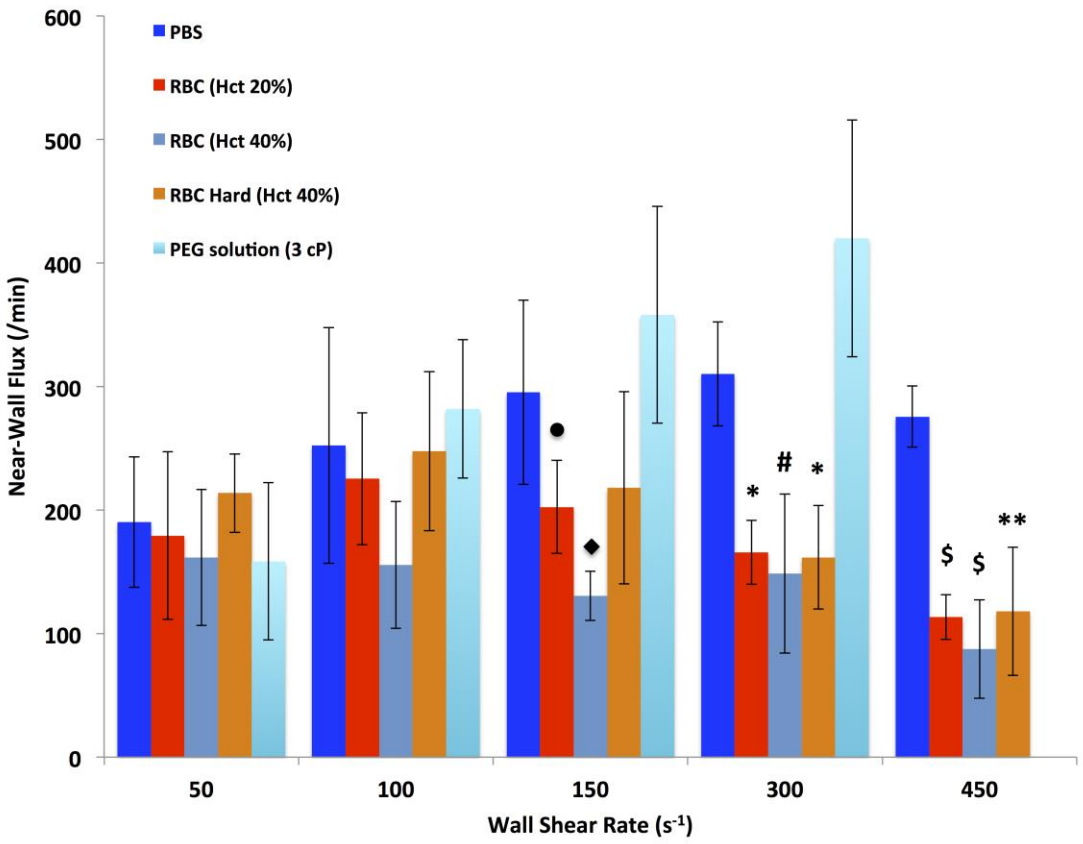

Fig. 1.9: Near-wall flux of biotinylated microbubbles targeted to streptavidin (10 µg/ml) in the upright configuration assessed by fluorescent microscopy. Values are mean ± SD (n = 3-5). •$p < 0.05$, ◆$p < 0.005$ vs. PBS and PEG solution at 150 s^{-1}. *$p < 0.005$, #$p < 0.01$ vs. PBS and PEG solution at 300 s^{-1}. \$$p < 0.001$, **$p < 0.005$ vs. PBS at 450 s^{-1}.

In the inverted flow chamber setting, the buoyant forces work against the binding of bubbles to the substrate: gravity pulls the bubbles away from the target surface. Fig. 10 shows the results for adhesion efficiency of microbubbles under these experimental conditions for a hematocrit of 40%. In the absence of red cells, virtually no microbubble targeting was observed in the inverted configuration, but in their presence significantly higher adhesion of microbubbles to the target surface was observed (Fig. 1.10).

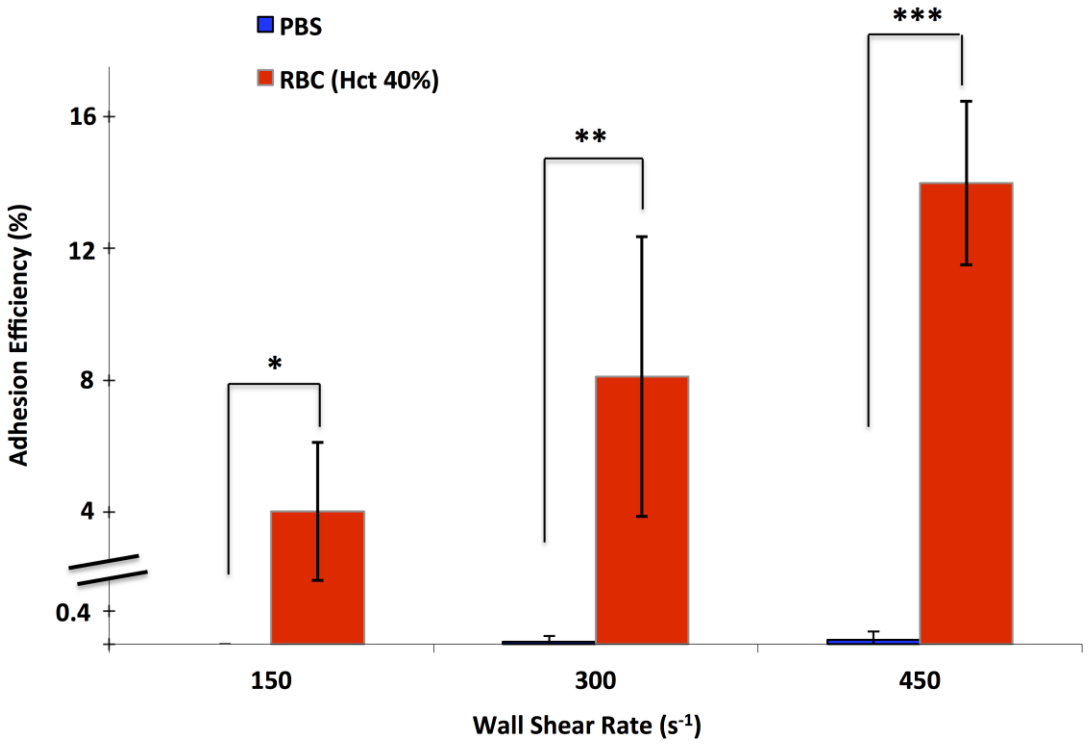

Fig. 1.10: Adhesion efficiency of biotinylated microbubbles targeted to streptavidin (10 μg/ml) in the inverted configuration assessed by fluorescent microscopy (n = 4, *p < 0.01, **p < 0.05, ***p < 0.0005).

At low streptavidin concentration (0.5 μg/ml), we found that large fraction of the adhesive interactions were transient in the presence of RBCs (Fig. 1.11). At 450 s^{-1}, while the total (stable + transient) adhesive interactions were still high, more than 75% of these interactions were transient. This behavior is qualitatively different from the interactions seen at high substrate densities, where transient interactions were absent with RBCs. In plain buffer, microbubbles never displayed transient binding to the substrate.

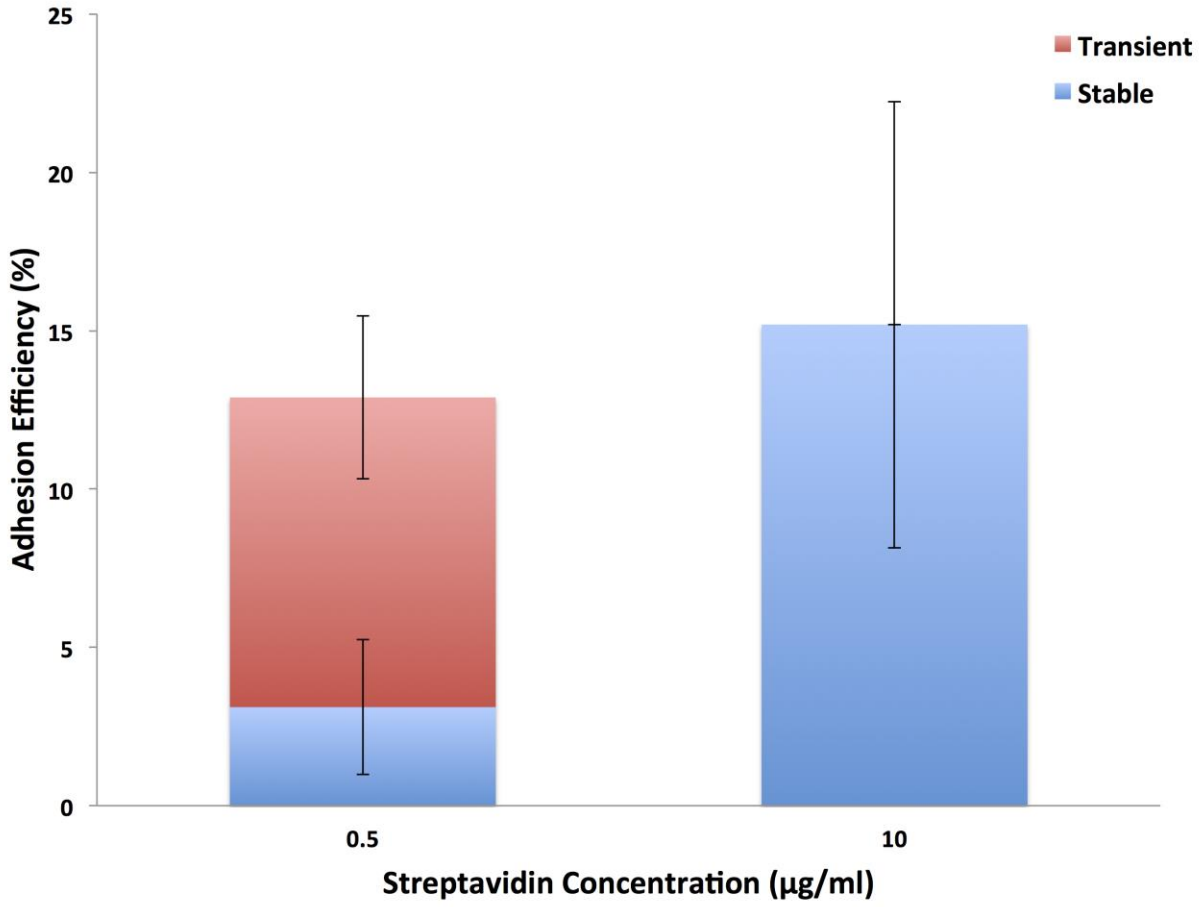

Fig. 1.11: Transient and stable adhesion of microbubbles in the presence of RBCs (hct ~ 40%) at 450 s^{-1} at different streptavidin concentrations

Microbubble velocity was measured for a subset of the microbubbles that went on to adhere to the surface. The results are presented in Fig. 1.12 for shear rate of 450 s^{-1}. Microbubble velocities were substantially higher when RBCs were present, with velocities as much as three times that found in PBS. This also indicates that the microbubbles decelerate more before binding when RBCs are present. The images in Fig. 1.13 illustrate the unsteady nature of the near-wall flow field due to the presence of RBCs. Microbubbles

undergo higher velocity variations when RBCs are present. In contrast, in PBS the microbubble velocity is constant (Fig. 1.14).

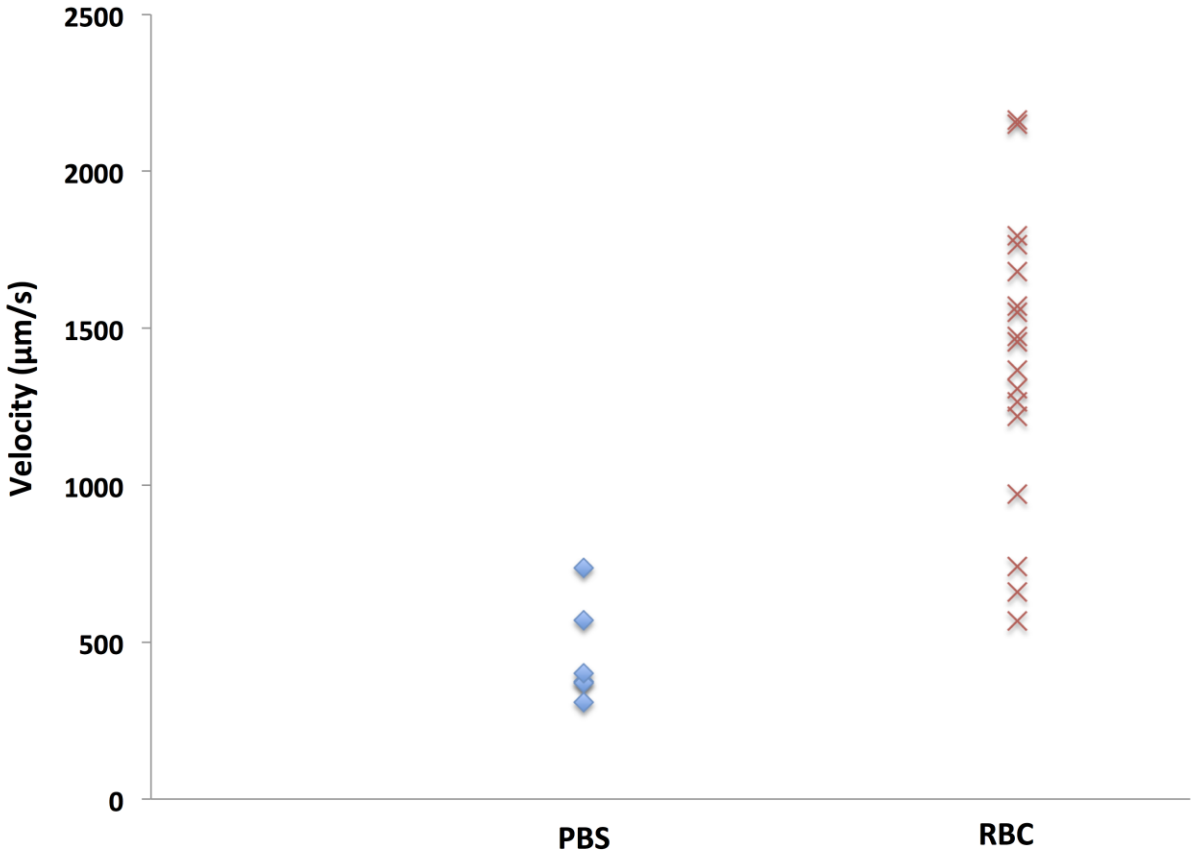

Fig. 1.12: Velocity of microbubbles prior to adhesion with PBS and RBCs at hematocrit ~ 40% (Shear rate = 450 s^{-1})

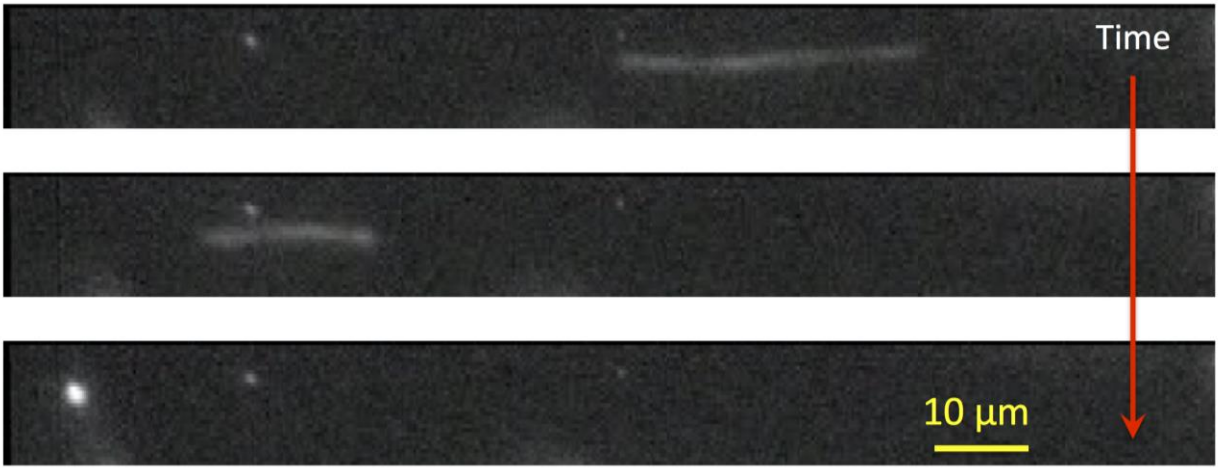

Fig. 1.13: Microbubble tracking in RBC (Hct 40%) prior to adhesion (Shear Rate = 450 s^{-1}, Frame rate = 30 fps, 3 consecutive frames)

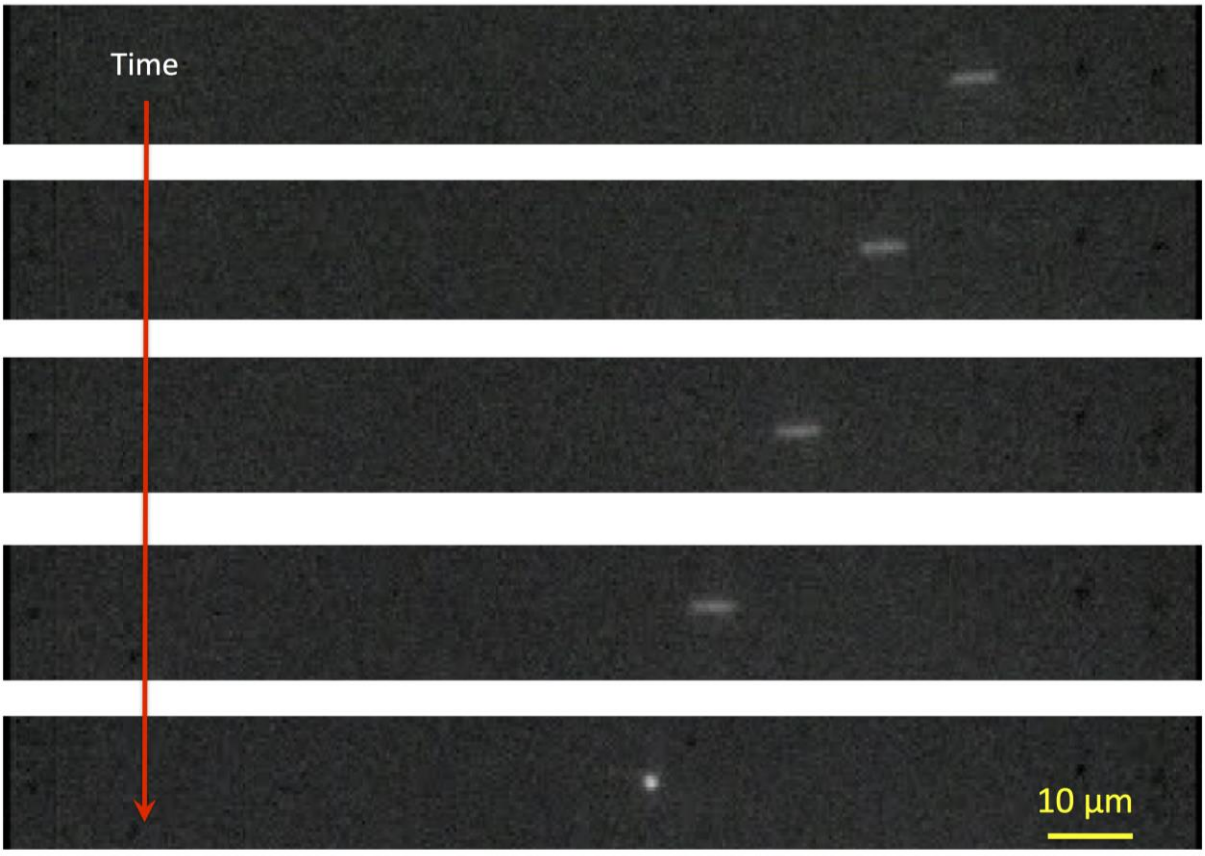

Fig. 1.14: Microbubble tracking in PBS prior to adhesion (Shear Rate = 450 s^{-1}, Frame rate = 30 fps, 5 consecutive frames)

P-selectin targeting in flow chamber assay

To examine whether the effect of RBCs on microbubble targeting is ligand concentration dependent we performed P-selectin targeting experiments with two different antibody concentrations. At high ligand concentration (1.5 μg/10^7 microbubbles), microbubble binding to P-selectin was found to be significantly higher in the presence of RBCs in fast flow conditions. Mean echo intensity from bound bubbles was 35-50% higher ($p < 0.05$) when RBCs were used at a hematocrit of 40% (Fig. 1.15). In contrast, microbubble binding at the low ligand concentration (0.075 μg/10^7 microbubbles) was significantly reduced in the presence of RBCs in fast flow conditions ($p < 0.01$). At 600 s^{-1}, signal from bound bubbles in the presence of RBCs was less than 50% of that observed in PBS (Fig. 1.16). P-selectin targeting at high shear rates using sLe^a-conjugated microbubbles was not affected by the presence of RBCs. There was no significant different in the bound bubble signal between PBS and RBC at 40% hematocrit (Fig. 1.17). sLe^a-conjugated microbubbles have previously been demonstrated to binding efficiently at high shear rates even in plain buffer [35].

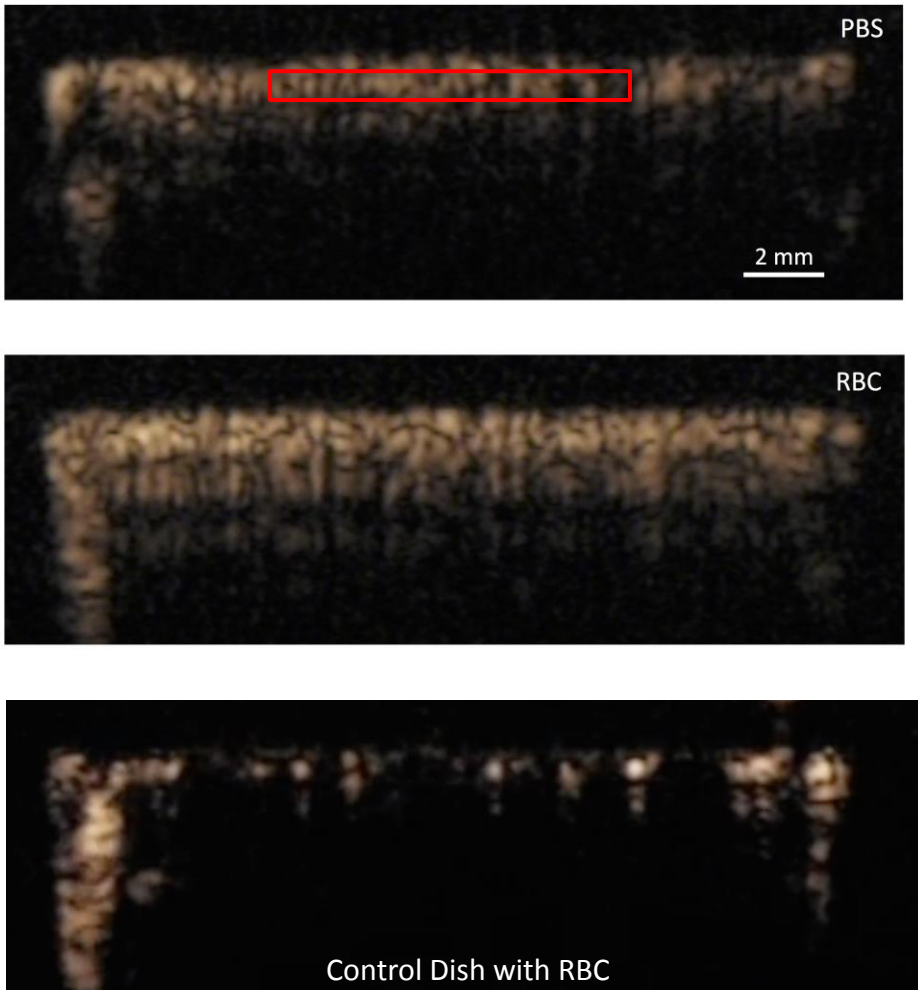

Fig. 1.15a: Representative ultrasound images of *in vitro* microbubble targeting to P-selectin at high antibody concentration (1.5 μg/10^7 μBs). The red box indicates the ROI on the image where echo intensity was quantified. Control dish was incubated with PBS and blocked with 1.5% BSA.

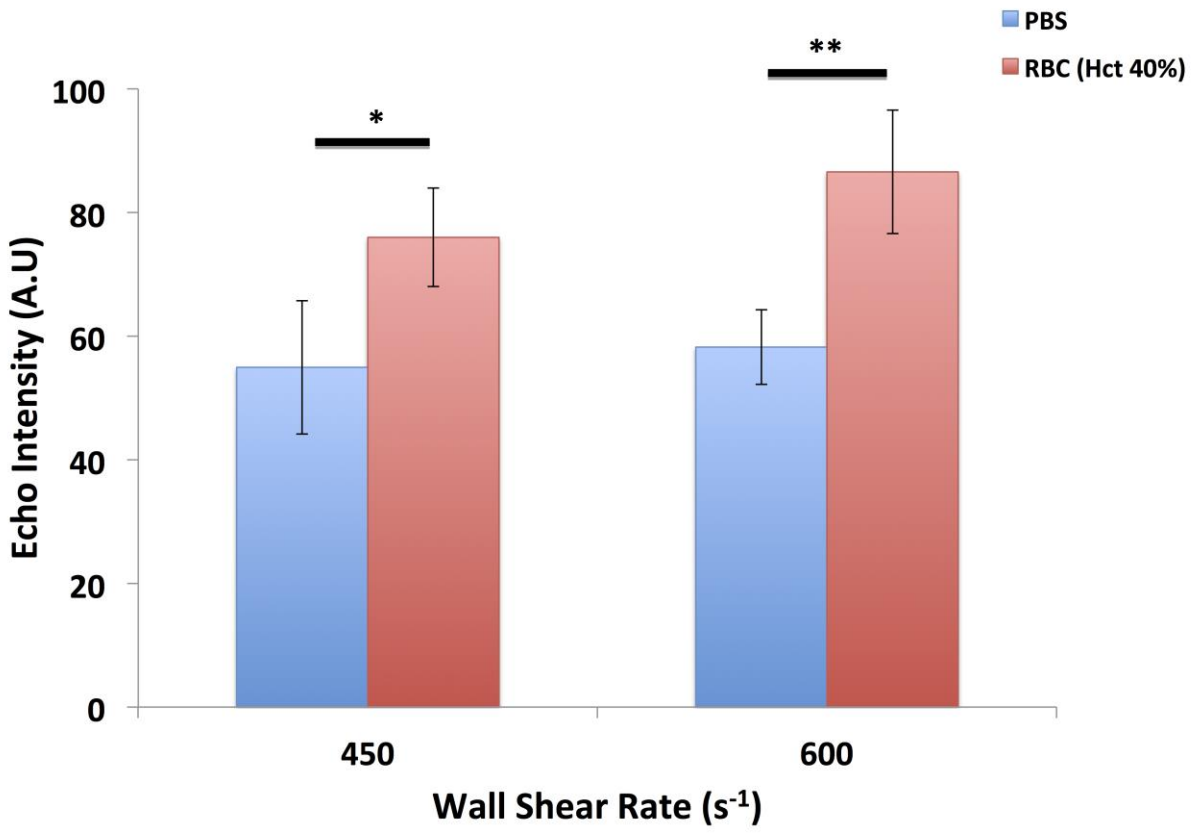

Fig. 1.15b: Bound microbubble echo intensity at high antibody (anti P-selectin) concentration (1.5 μg/10^7 μBs). n = 4, *p < 0.05, **p < 0.005.

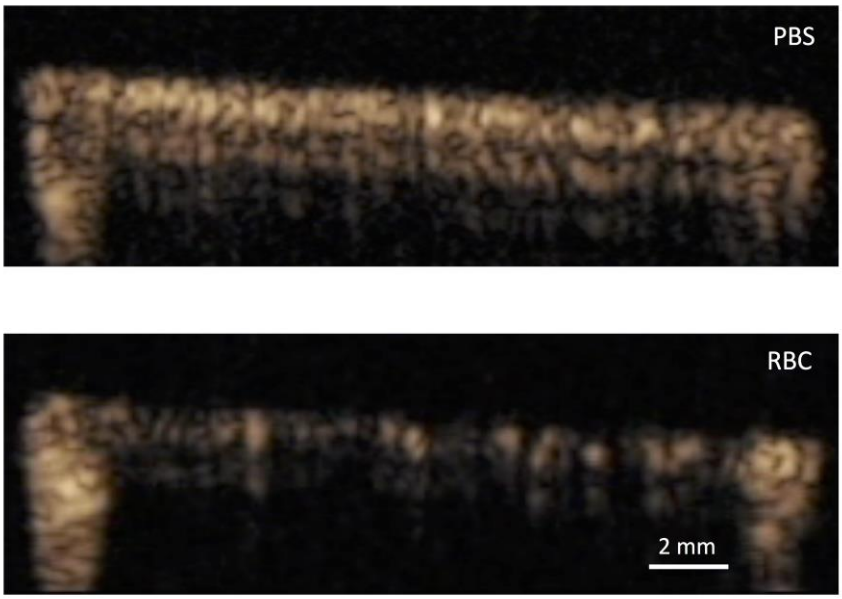

Fig. 1.16a: Representative ultrasound images of *in vitro* microbubble targeting to P-selectin at low antibody concentration (0.075 μg/10^7 μBs)

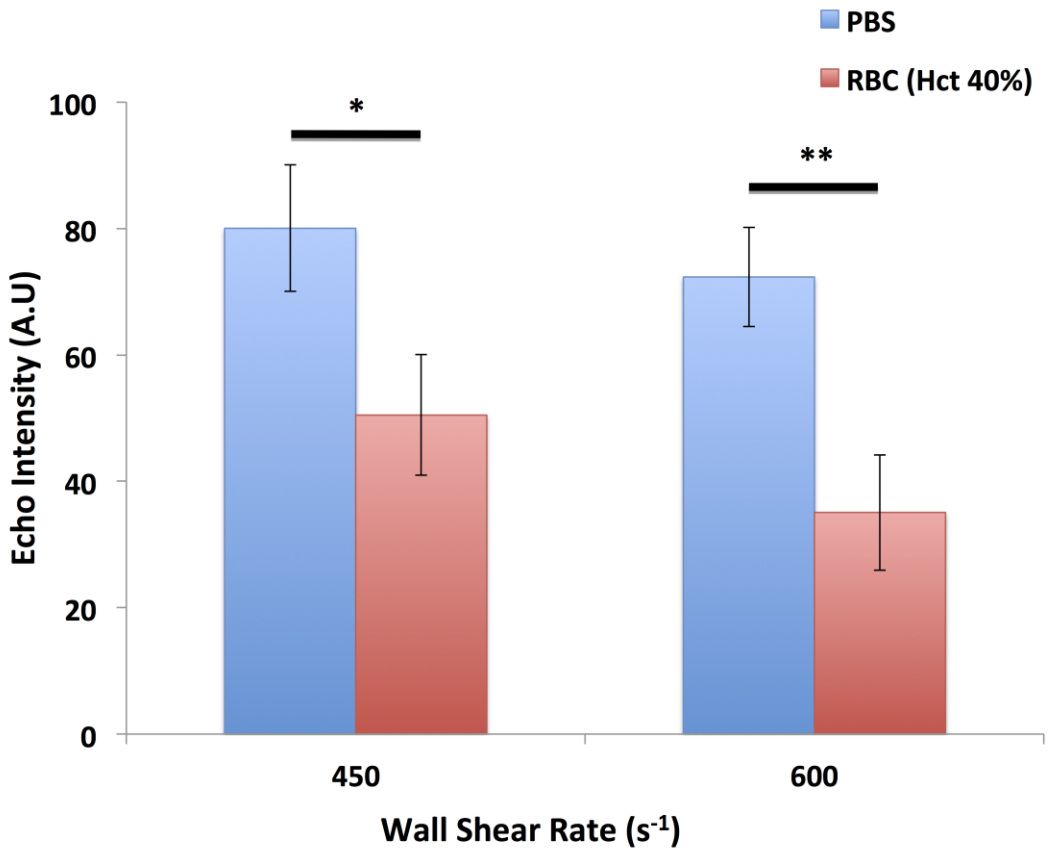

Fig. 1.16b: Bound microbubble echo intensity at low antibody (anti P-selectin) concentration (0.075 μg/10^7 μBs). n = 4-5, *p < 0.01, **p < 0.0002.

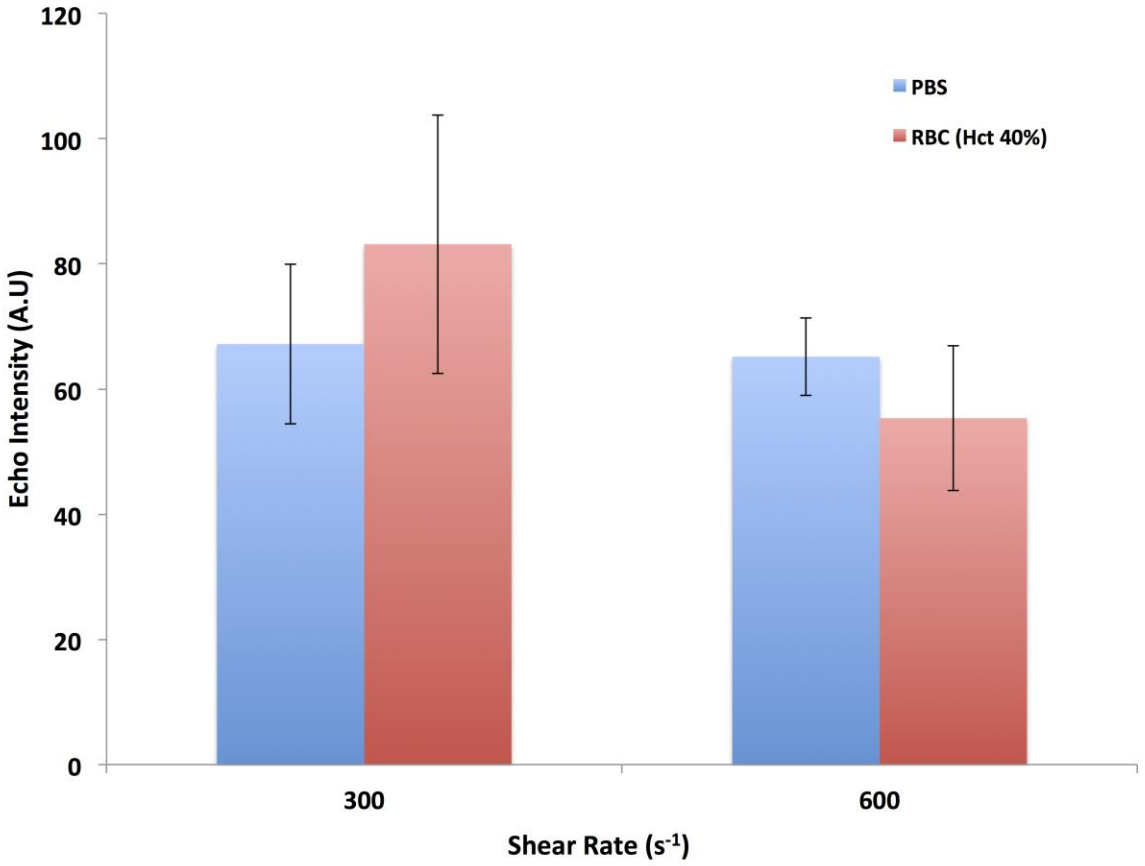

Fig. 1.17: *In vitro* P-selectin targeting using sLe^a-conjugated microbubbles. (n = 5)

Ex vivo P-selectin targeting

To investigate the role of RBCs in P-selectin targeting in a relevant physiological model, we performed flow studies in an *ex vivo* inflamed murine carotid artery model. Due to natural variation in vessel diameter the flow rate we chose (0.5 ml/min) corresponded to a range of shear rates (400-650 s^{-1}). These are similar to the WSR values used in the *in vitro* flow experiments. In these fast flow conditions, in PBS, antibody-coupled microbubbles exhibited a low level of binding, similar to the binding seen with isotype-conjugated control microbubbles. P-selectin targeting using monoclonal antibody RB40.34 was significantly higher in the presence of RBCs in this *ex vivo* model. Mean echo intensity from bound

bubbles was more than two-fold higher when RBCs (Hct 40%) were used ($n = 5$, $p < 0.001$) as shown in Fig. 1.18.

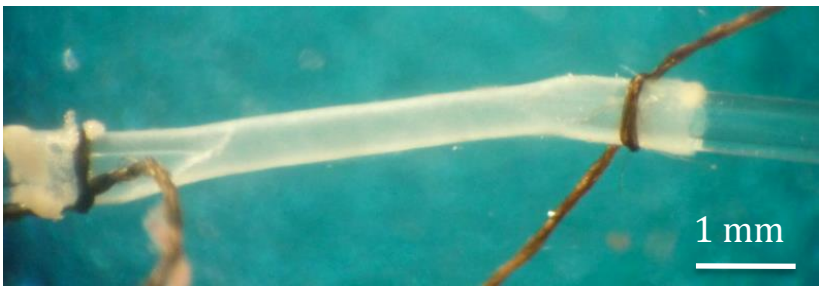

Fig. 1.18a: Mouse carotid artery cannulated using PE-10 tubing.

Fig. 1.18b: P-selectin targeted microbubble signal in PBS

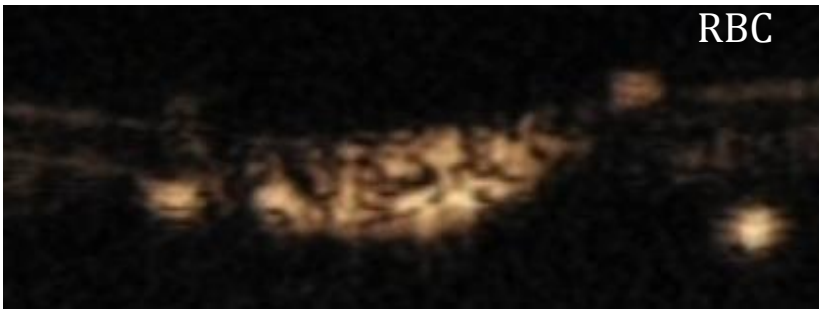

Fig. 1.18c: P-selectin targeted microbubble signal with RBCs at hct ~ 40%

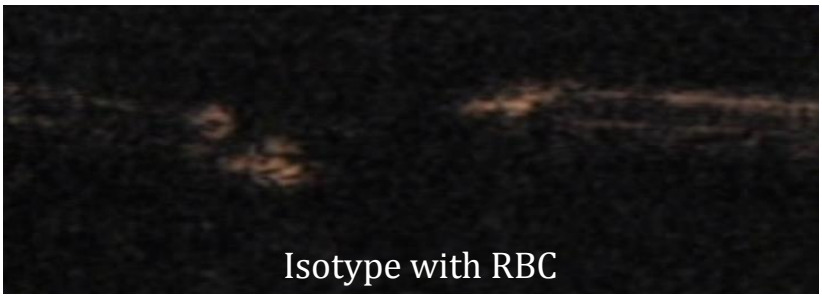

Fig. 1.18d: Isotype-conjugated microbubbles with RBCs at hct ~ 40%

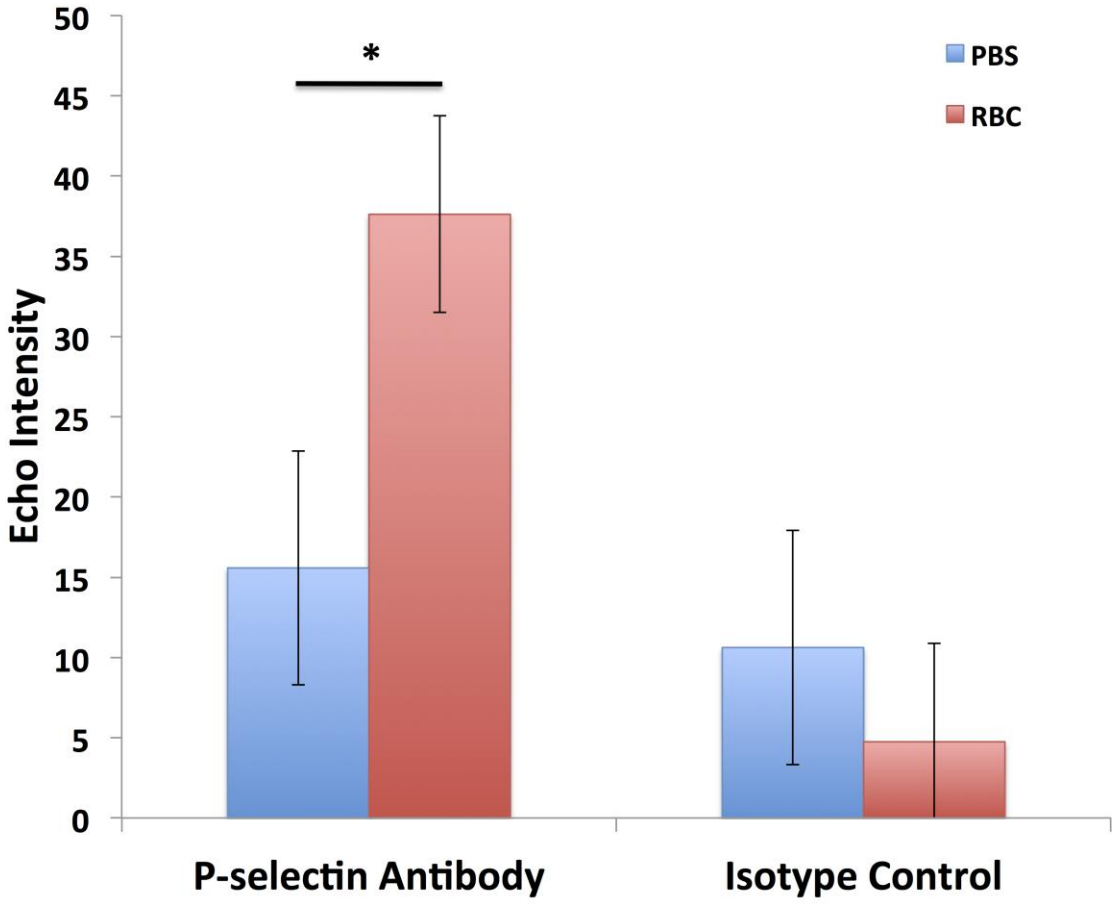

Fig. 1.18e: Ex-vivo murine carotid artery targeting to P-selectin. Microbubbles targeted to P- selectin using antibody RB40.34 (n = 5, *p < 0.001) and isotype control (n=3).

Microbubble detachment

Microbubble detachment was studied to understand the effect of RBCs on microbubble retention under flow. Detachment from P-selectin was assessed for high and low ligand concentrations, with and without RBCs. Microbubble detachment occurred at lower shear rates in the presence of RBCs (Fig. 1.19). For low ligand concentration, half-maximal detachment occurred at 600 s^{-1} and 3900 s^{-1} with RBCs and PBS, respectively. For high

ligand concentration, half-maximal detachment occurred at 3300 s^{-1} in the presence of RBCs; with PBS almost 60% of initially bound microbubbles remained adherent even at 19200 s^{-1}.

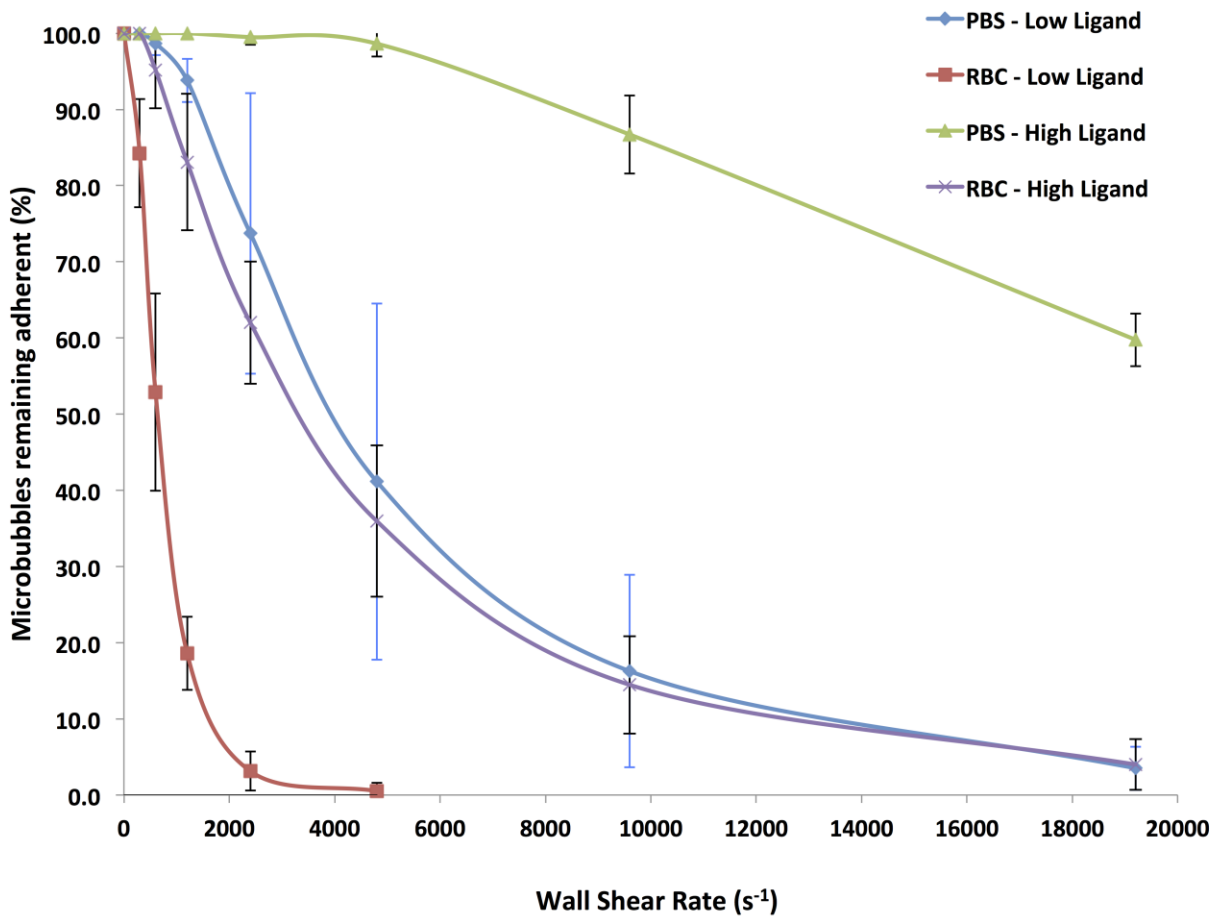

Fig. 1.19: Microbubble detachment with PBS and RBCs (hct 40%) under incremental increases of shear stress at different antibody densities (High – 1.5 µg per 10^7 microbubbles, Low – 0.075 µg per 10^7 microbubbles). P-selectin concentration = 3 µg/ml. (n = 4-5)

TIRF microscopy

Near-wall trajectories of 3 μm polystyrene beads obtained from TIRF microscopy are shown in Fig. 1.20. During particle translation in the flow direction no substantial lateral movement was seen in the case of PBS. But in the presence of RBCs the particle exhibited repeated lateral excursions from its general flow path. Significant fluctuations of the particle TIRF signal intensities in the RBC-containing media also point to the variation of particle distance from the flow deck. These deviations are caused by the hydrodynamic interactions and physical collisions of the particles with RBCs.

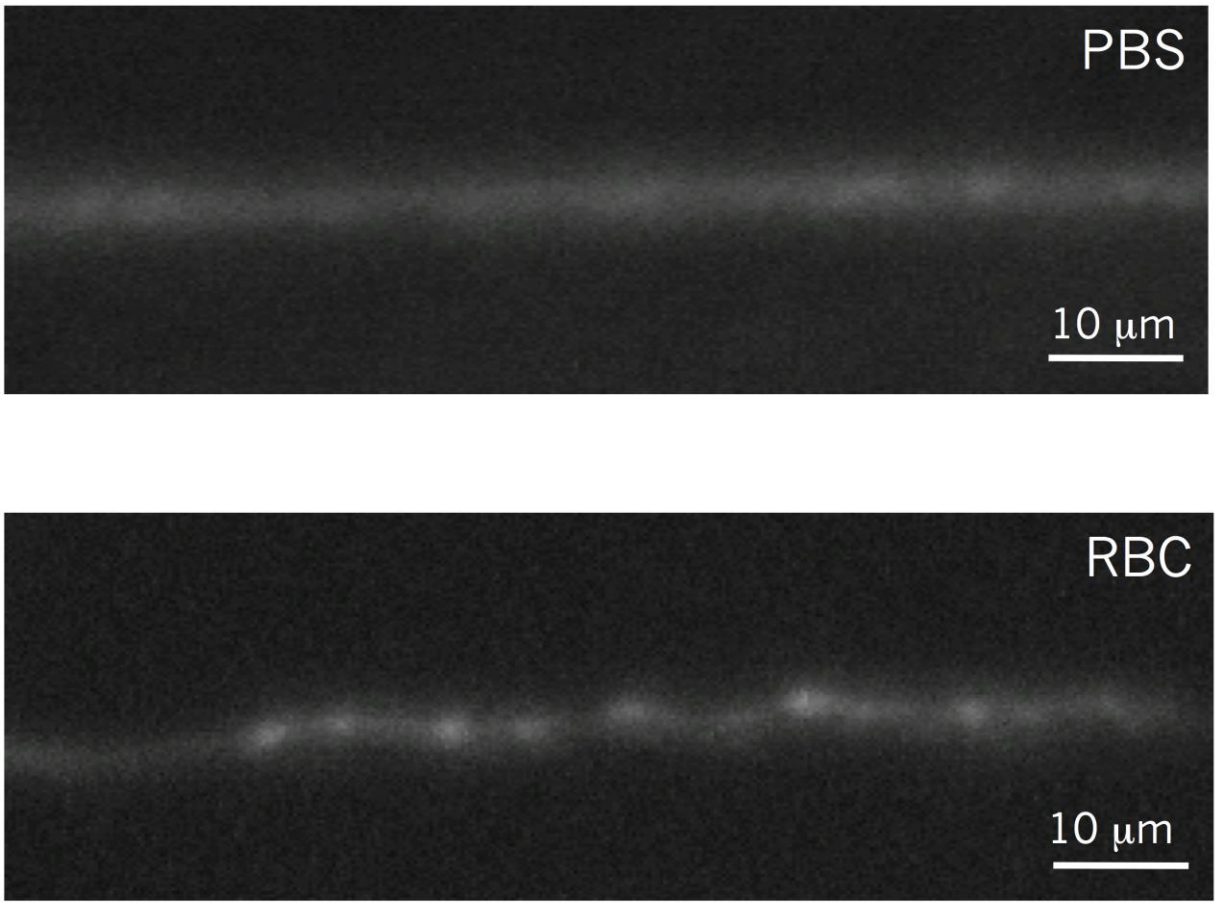

Fig. 1.20: Near-wall images of flowing beads (Diameter = 3 μm) with PBS and RBCs obtained using total internal reflection fluorescence (TIRF) microscopy.

Discussion

Targeted microbubbles encounter a complex hemodynamic environment *in vivo*, with large variations in shear rates and hematocrit at different levels of the vasculature, from the microvessels to the large vessels. Rational design of targeted microbubbles for diagnostic and therapeutic purposes requires adequate understanding of microbubble adhesion dynamics. Our understanding of microbubble targeting in the vasculature is still incomplete [61]. Notably, the influence of RBCs on the binding behavior of microbubbles has not yet been systematically investigated, although it is known that RBC interactions play a critical role in the adhesion of leukocytes and platelets. In the present work we conducted *in vitro* and *ex vivo* studies to assess the effect of RBCs on microbubble binding to streptavidin and P-selectin targets. We demonstrated that RBCs can enable antibody-conjugated microbubble targeting at higher WSR, but they may also disrupt the retention of microbubbles and limit targeting in certain conditions. At high ligand concentrations and higher shear rates (> 150 s^{-1}), we found that RBCs tend to enhance microbubble targeting relative to plain aqueous media. RBCs are effective in promoting microbubble adhesion even against buoyancy, as we observe in the inverted flow chamber studies. We demonstrated increased targeting to the inflammation marker P-selectin in an *ex vivo* carotid artery model, establishing the physiologic relevance of our results. On the other hand, at low microbubble ligand densities, RBCs diminished binding at high shear rates compared to plain buffer. Bound microbubbles were also detached from P-selectin substrate at several-fold lower shear rates when RBCs were present in flow. The key insight from our study is that RBCs can have both pro- and anti-adhesive effects with regard to microbubble adhesion.

The effect of RBCs on agents (particles or cells) in flow can be broadly divided into two categories. The first is due to collective lateral migration of RBCs that changes the cross-sectional distribution of agents. RBC migration away from the wall leads to exclusion of particles from the center of the vessel and relegates them to regions closer to the wall [34]. This typically results in a 'near-wall excess' of agents, most conspicuously observed in the case of platelets and platelet-sized particles [31, 44, 46], partially contributing to higher platelet adhesion in the presence of RBCs [44]. In the case of leukocytes, RBCs augment adhesion even without an increase in near-wall concentration [29, 43]. Our experimental method does not explicitly assess cross-sectional distribution of microbubbles; we quantified near-wall flux in the field-of-view to evaluate the adhesion efficiency in a parallel plate flow chamber (at the depth of ~10 μm or less). We did not observe an increase of the microbubble near-wall flux in the presence of RBCs; the flux actually decreased at higher WSR when RBCs were present. This indicates that increased targeting in the presence of RBCs does not *require* an increased number of microbubbles in the near-wall region. Migration of RBCs under flow is linked to their deformability; reducing the deformability of RBCs diminishes their migration effects [34]. Hardened RBCs were no different than normal RBCs in their effect on microbubble targeting. This further underscores that collective migration of RBCs is not playing a major role in targeting. Microbubble flow behavior in the microvasculature has been reported to be similar to RBCs [9, 10]: it has been suggested that microbubbles are present in higher concentration in the central region of flow as compared to the near-wall regions. This is considered a drawback for targeting, but our results show that high levels of binding can be achieved even under these circumstances since RBCs make targeting more efficient under conditions of high ligand

density on the bubble surface. Taken together with our results showing reduction in microbubble binding under low ligand conditions, this suggests that other factors might be more important for targeting than cross-sectional redistribution of agents.

The second effect is localized: individual particle motion [40-42, 62] as well as attachment and detachment dynamics are affected by hydrodynamic interactions and collisions with RBCs [51]. Microbubbles suspended in high viscosity medium have binding behavior similar to those suspended in PBS. This emphasizes that the particulate nature of blood has a distinct role in targeting. Interactions with RBCs impose forces and torques on microbubbles, additional to those exerted by the fluid. The force on a particle due to collisions with RBCs is comprised of wall-normal and tangential components [63, 64]. These forces would strongly affect particle motion. In an undisturbed laminar flow in plain buffer, particle interactions with the wall are minimal. Linear particle motion in the flow direction is hardly perturbed in this case, as seen in our TIRF microscopy images obtained without RBCs. We can envision a particle "skimming" in close proximity to the target surface but rarely touching it. In contrast, RBC collisions alter the particle trajectory and cause deviations from the linear path. In the TIRF microscopy images with RBCs present, the irregular motion of the particle was clearly visible. More importantly, punctate variation in intensity along the particle path was observed, indicative of out-of-plane (perpendicular to the wall) movement and/or changes in particle velocity. In the near-wall regions this would lead to increased number of interactions with the wall [40, 42]. The normal force on the bubble also increases the probability that a microbubble-wall interaction would result in adhesion i.e. enhance the efficiency of each interaction. The probability of binding would be boosted even in the absence of an increase in near-wall concentration. Moreover, at higher velocities, the

magnitude of the normal force imparted on impact and the number of collisions themselves would be greater. This might explain the observed increase in adhesion efficiency as WSR is increased. Thus, the wall-normal component tends to be pro-adhesive. The tangential component, on the other hand, is anti-adhesive and would tend to disrupt microbubble binding to the surface. The tangential component can blunt or even reverse the effect of the normal forces. This is evident from the reduction in binding in the presence of RBCs when ligand density on the microbubbles is low. In the detachment assay, the lower retention of bound microbubbles indicates that the presence of RBCs imposes substantial dislodging forces exceeding the fluid drag force when no RBCs are present. At high ligand concentrations, the normal forces and increased wall interactions aid the formation of sufficient number of bonds to overcome the additional tangential forces due to the RBCs. The microbubbles remain firmly bound to the wall and an overall increase in targeting is achieved. Conversely, at low ligand densities, due to the smaller number of bonds formed, the tangential forces imparted by flowing RBCs cannot be resisted; the bonds fail and microbubbles are sheared from the wall. An overall reduction in targeting is observed despite increased microbubble-wall interactions. In sum, local hydrodynamic effects of RBCs are critical factors in determining the fate of targeting.

Our results suggest that RBCs influence targeting by augmenting the frequency and efficiency of microbubble-wall interactions, on the one hand, and by imposing bond-disruptive forces, on the other. It is instructive to compare this explanation with the analytic approach used in the context of platelet adhesion and aggregation in the presence of RBCs. The effect of RBC collisions on platelet trajectory in flow has been modeled as a random walk phenomenon, albeit with dependence on shear rate and RBC concentration

[65-67]. Platelet diffusivity has been reported to be enhanced at least two orders of magnitude due to RBC motions [33, 65, 66]. The higher diffusion coefficient and high near-wall concentration of platelets in blood leads to increased wall collision rate and consequent increase in platelet adhesion. Platelet aggregation was similarly enhanced due to RBCs, but while the rate of aggregation increased with shear rate, the size of the aggregates decreased [68]. This was attributed to bond breakage at the higher shear forces, although forces imposed by RBCs were not explicitly held responsible.

In receptor-ligand mediated adhesion the bonds have to be able to resist shear forces and torques. Hence, quantifying the additional forces imposed by RBCs would aid our understanding of the adhesion process. Experimentally dissecting these small forces is often challenging, especially in concentrated suspensions where optical access into the flow is limited. Novel computational techniques have been used to analyze the forces stemming from RBC interactions. Migliorini et al. quantified the forces and torques resulting from the collision of a single RBC with a rolling leukocyte [63]. They reported a 10% increase in rolling velocity, resulting from increased tangential forces and torques. Furthermore, their computations suggested that the time of application and magnitude of the normal force due to RBCs ($\sim$ 15 pN) is sufficient to penetrate the endothelial glycocalyx and enhance adhesion. In another computational study, Isfahani et al. demonstrated that the surface-averaged stream-wise (in the flow direction) forces and normal forces on an adherent leukocyte were significantly higher, as compared to plasma, when RBCs were present at a hematocrit of 25% [64]. With RBCs, the local maximum normal stresses were 3-fold greater in comparison to a fluid with viscosity similar to plasma. RBCs' motion over the adherent cell also resulted in both tangential and normal forces exhibiting an oscillatory character.

Finally, it should be noted that RBCs at physiologic hematocrit modify the cross-sectional velocity profile [69], leading to a higher shear rates and shear stresses [70]. While computational studies have begun to quantify the forces exerted by individual RBCs, the relative contributions of the higher drag force and torque due to the steeper near-wall velocity gradient and the physical force exerted by RBC collisions remain an open question.

It is clear that RBCs modify the local hydrodynamics in a complex way, with implications for targeting. When receptor-ligand avidity is high, they help microbubbles overcome the anti-adhesive effects of higher shear forces and lower contact times that preclude bond formation at higher flow rates. This is consistent with a recent ICAM-1 targeting study conducted using whole blood, which found significant binding and retention of polymeric bubbles at high shear [71]. *In vitro* or *ex vivo* flow assays performed without RBCs may be underestimating the targeting efficacy of microbubbles *in vivo*. Owen et al. recently demonstrated that RBCs reduce targeting of magnetic as well as biotinylated microbubbles [38]. While this confirms a subset of the results presented in this study, a complete comparison is not possible due to differences in the experimental conditions; the most probable source of variation being the receptor site densities on the substrate and the ligand density on microbubbles. They used a cellulose tube (Inner diameter = 200 μm) as their substrate to assess binding and did not report receptor site densities. The diminution of binding presented in our study for low receptor-ligand avidity has interesting physiological ramifications: RBCs might be playing a role in preventing non-specific adhesion of microbubbles. Wu et al. report a reduction in non-specific binding of microbubbles when whole blood was introduced in their *ex vivo* flow assay [71]. Crucially, RBCs might disrupt adhesion in cases where the expression of target molecules on the

vascular endothelium is low, making early detection of disease markers challenging under fast flow conditions. However, if a constitutively expressed low level of target receptor is present in the normal vasculature, presence of RBCs may abolish microbubble adhesion, reducing non-specific ultrasound signal in normal tissues. Only if a significant overexpression of the receptor occurs, e.g. in the area of disease, the "pro-adhesive" effects would overcome the tangential "pro-dislodging" forces, and targeted microbubble adhesion would occur.

Qualitative and quantitative understanding of the role of RBCs in the adhesion process is relevant for the rational design of targeting agents and strategies. Microbubble size, ligand density, and shell material properties could be engineered with an emphasis on optimal hemodynamic performance. For example, large microbubbles provide a higher acoustic backscatter, but would be more easily dislodged from the endothelium due to blood flow [72, 73]. The use of acoustic radiation force to translate bubbles towards the vessel wall is a promising strategy for enhancing targeting and is being actively investigated [74-78]. In addition to bringing microbubbles in closer proximity to the wall, it is likely that radiation force aids microbubble retention by ensuring firmer adhesion of microbubbles that is harder for RBCs to disrupt. In this context, understanding the relative balance of attachment and detachment due to RBCs would enable better tuning of acoustic parameters.

The results presented in this study demonstrate that RBC interactions are multi-faceted and alter microbubble targeting in a manner that is more complex than is commonly assumed. The introduction of RBCs in a flow assay takes us a step closer to understanding the role of blood rheology in the microbubble adhesion process. Several questions still

remain to be answered. The quantification of forces imposed on microbubbles by RBCs would be a useful step in this direction. The recent fluid dynamic modeling studies mentioned above in the context of leukocyte adhesion and thrombus formation have shed useful light on the forces exerted by RBCs and their mechanical effects [52, 53, 64]. The next step would be a robust coupling of the fluid dynamic models with particle adhesion models.

Conclusions

RBCs at physiological hematocrit enhanced microbubble targeting, up to an order of magnitude, *in vitro* and *ex vivo* at high shear flow and high microbubble ligand densities. In contrast, RBCs decreased targeting at low ligand densities. The dislodging of microbubbles under flow was higher in the presence of RBCs. Particle trajectories obtained from TIRF microscopy exhibited punctate variation in intensity and deviations from the linear path when RBCs were present. The likely mechanistic basis of these observations lies in RBC collisions that exert tangential (anti-adhesion) and normal (pro-adhesion) forces on the microbubbles. Using RBCs in the *in vitro* flow targeting assays is physiologically relevant for studying microbubble targeting, and would aid in the development of microbubbles that are optimized for targeting *in vivo*.

Chapter 3

Disturbed Hemodynamics and Microbubble Targeting

Introduction

In the microvasculature viscous effects dominate inertial effects, but in the large arteries, due to the high flow rates, inertial effects become relevant. In particular, this leads to locally disturbed flow at certain sites of the vasculature. Atheroprone areas, like arterial bifurcations and curvatures, and vascular abnormalities, like stenoses and aneurysms, are frequent sites of disturbed flow. At these locations, as the flow encounters a geometric expansion (for e.g. the carotid sinus), it separates from the wall and reattaches some distance downstream, establishing a local zone of recirculation (Fig. 2.1). Under such conditions, the flow streamlines are no longer unidirectional and change direction abruptly (e.g. flow reversal) and the spatial distribution of wall shear stress is non-uniform. Disturbed flow has been shown to play an important role in the localization of atherosclerosis, affecting several key processes including endothelial gene expression, chemokine expression [79], and the focal recruitment of monocytes [80, 81].

The so-called backward step flow is a classic tool in experimental fluid dynamics to investigate recirculating flows and benchmark computational fluid dynamics (CFD) codes. Its flow chamber implementation essentially consists of a rectangular channel or cylinder with a step expansion. This arrangement creates a vortex (recirculation zone) as the flow goes over the step into the larger channel (Fig. 2.2). The region at which the flow reattaches to the wall is also referred to as the stagnation zone. Fully developed laminar flow is only reestablished further downstream of the stagnation zone. The flow over a step recreates

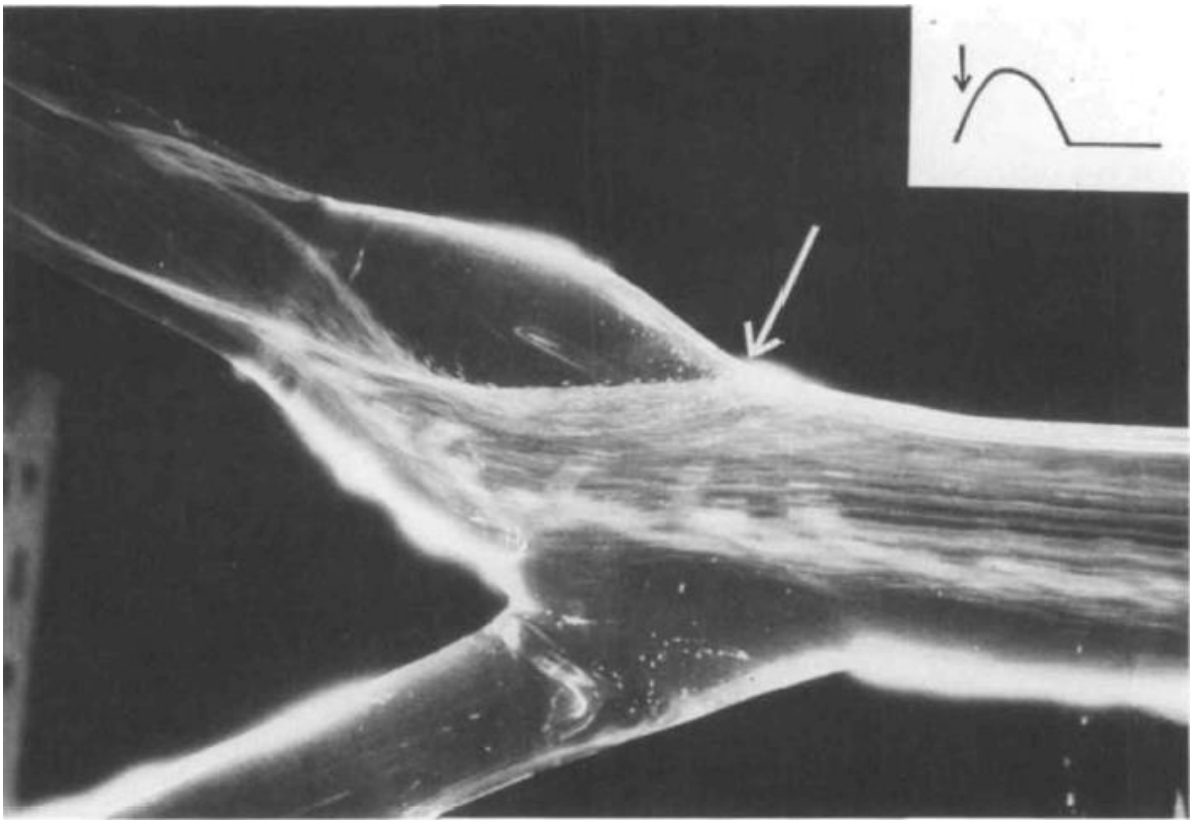

Fig 2.1: Flow visualization in a model of the carotid artery bifurcation during the accelerating phase of systole [82]. Arrow indicates the region where flow separates from the wall.

the essential features seen in disturbed flow in the vasculature. It allows us to examine adhesion behavior in sub-regions with distinctive flow features (the region of recirculation, the region of flow reattachment and stagnation, the region of flow recovery immediately downstream of the stagnation zone, and the region of fully developed flow far downstream). Several investigators have made fruitful use of the backward step assay to study the impact of locally disturbed flow on adhesion. At high shear rates, recirculating flow has been shown to promote the localized binding of neutrophils, lymphocytes, and

monocytes to P-selectin substrate [83-85] and to endothelial cells [80, 86]. The maximum adhesion typically occurred in the vicinity of the stagnation zone, presumably due to the low velocities in the region. Platelet adhesion to collagen under disturbed flow was investigated by Karino et al. who used a tubular expansion to create a stable annular vortex [87]. Peak adhesion in this case was found to occur within the recirculation zone. Charoenphol et al. also demonstrated a localized increase in the adhesion of sLe^A-conjugated micron-sized particles to endothelial cells in a step-expansion flow chamber [88].

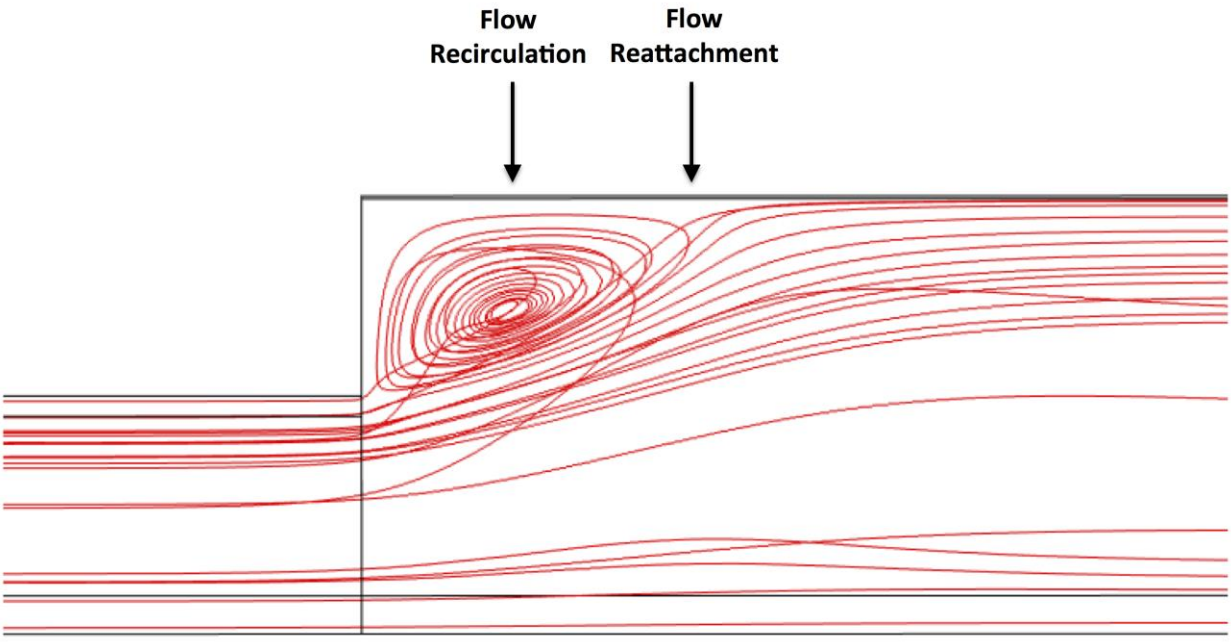

Fig 2.2: Flow streamlines and vortex formation in a backward step flow channel (Generated using CFD software COMSOL)

Atheroprone and stenosed regions of the vasculature are important candidates for molecular imaging and targeted drug delivery. In this context, understanding the influence

of disturbed flow on microbubble targeting is vital. We hypothesized that disturbed flow would facilitate microbubble adhesion at high shear rates. To test this we employed a step expansion flow chamber to characterize microbubble adhesion under recirculating flow conditions.

Materials and Methods

The flow chamber from **Aim 1** was modified to create the disturbed flow environment. The step expansion was created by the layering of two gaskets. One gasket was laid on top of the other in such a way that a portion of the channel was covered. This raised the vertical height of the flow path in one section of the chamber relative to the covered section. The narrower section served as the inlet. Step expansions of ratios 1:2 (inlet channel = 254 μm, expanded channel = 508 μm) and 1:3 (inlet channel = 127 μm, expanded channel = 381 μm) were generated by the arrangement of gaskets.

Microbubbles were prepared and streptavidin was adsorbed on the dishes (10 μg/ml) as described in Chap 1. Microbubble binding to the different regions was quantified using fluorescent microscopy. For the 1:2 expansion, two shear rates were tested (350 s^{-1} and 700 s^{-1}), with PBS as the buffer. The binding study in the 1:3 expansion was conducted at 700 s^{-1}. For the 1:2 expansion, additional experiments were performed with RBCs at 40% Hct and shear rate of 350 s^{-1}. The Reynolds number ranged from 8 to 26 for the different flow conditions. Imaging was performed using a 20X water-immersion lens. The observation area was 245 μm X 330 μm. The FOV was selected close to the centerline of the flow path to minimize side-wall effects. Microscopy was performed for 2 minutes at the region that encompassed the stagnation zone. At the end of 2 min, images were

sequentially collected, beginning at the step and up to a distance of 2000 μm downstream. Image analysis was performed off-line. Each FOV was partitioned into sections 50 μm wide and the adherent microbubbles in each section was counted. Spatial variation in microbubbles adhesion was also quantified by normalizing the number of adherent microbubbles in each section to the total number of bound microbubbles. The length of the recirculation zone – the distance between the step and reattachment zone - was also determined from the images. The reattachment zone was identified as the dividing region between backward and forward flow.

Three-dimensional laminar flow simulations using CFD software COMSOL Multiphysics (COMSOL, Inc. Burlington, MA) were conducted to compute the wall shear rates and the velocities in the vicinity of the vortex zone. The fluid was assumed to be Newtonian with constant viscosity (1 cP for plain buffer). For blood flow simulation, the non-Newtonian effects were neglected to simplify the computations and a constant viscosity of 3 cP was chosen. A schematic of the model is shown in Fig. 2.3. Further details of the CFD simulations are provided in the Appendix.

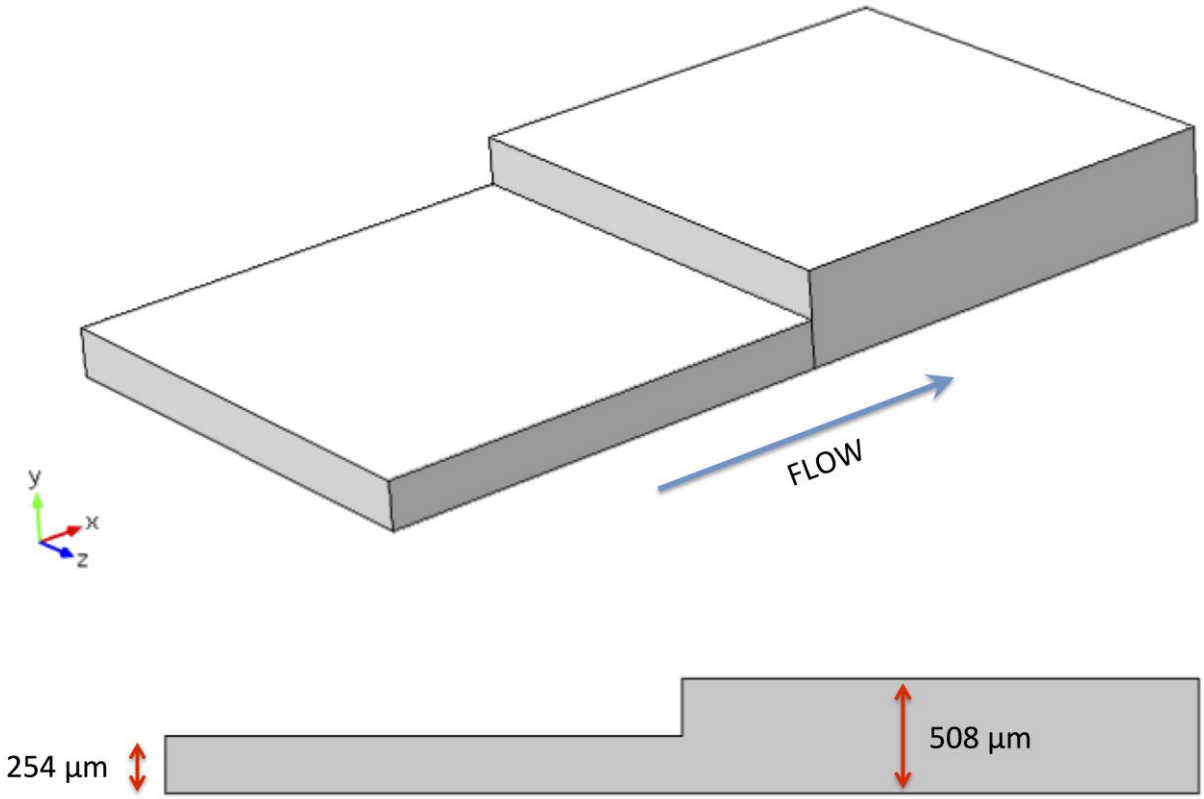

Fig. 2.3: Schematic of the geometry used for the CFD model

Results

Experimental and Computed Flow Features

The vortex past the step was stable for the lower shear rates, but at higher shear rates (700 s^{-1}) the reattachment zone was observed to oscillate back-and-forth over a small distance. Secondary flow (flow perpendicular to the side walls) was discernible inside the vortex. This was evident from the presence of a few microbubbles that entered the vortex from the sides before ultimately being shed from the vortex or adhering to the surface within the recirculation zone. The dimensions of the recirculation and stagnation zones for the different conditions are shown in Table 1. In the 1:2 expansion, increasing the flow rate

increased the length of the recirculation and reattachment zone. For the same flow rate and expansion ratio, the presence of RBCs (hct ~ 40%) reduced the length of the recirculation zone. This is a result of the higher bulk viscosity of the RBC suspension compared to PBS, which increases the resistance to flow separation. Employing a higher viscosity fluid in the computational flow model reduced the span of the recirculation zone as well.

The spatial variation in computed velocities and shear rates along the centerline displayed similar qualitative features for all the tested conditions. A representative example is illustrated in Fig. 2.4 for the 1:2 expansion and shear rate of 350 s^{-1}. Fig. 2.4a shows the computed wall-normal and axial velocity components along the length of the channel, 2 μm below the reactive surface. Negative normal velocities close to the step indicate flow away from the top wall. Positive values, indicating fluid motion towards the surface, are typical in the vicinity of the reattachment point. Normal velocities were zero close to the mid-point of the recirculation zone. Normal velocity components were also negligible far downstream, indicating reestablishment of non-disturbed flow. Axial velocities are negative in the vortexas the flow direction is towards the step; the peak negative velocity occurs at the midpoint between the step and the reattachment zone. After the stagnation zone the flow direction is away from the step and the fluid accelerates up to a constant velocity that is maintained downstream throughout (Fig. 2.4a). Fig. 2.4b shows a plot of the variation in wall shear rate along the channel centerline. In the vortex, the magnitude of shear rate increased from zero at the stagnation zone, reached a peak, and then decreased to zero at the step. The peak shear rates in the vortex were lower compared to fully developed flow downstream. The presence of RBCs further lowered the shear rates in the vortex.

Flow Condition	Length of Recirculation Zone (μm)		Length of Stagnation Zone (Experimental only) (μm)
	Experimental	Computed	
1:2 expansion, WSR 350	263 ± 6	280	31 ± 6
1:2 expansion, WSR 700	473 ± 6	459	71 ± 3
1:3 expansion, WSR 700	345 ± 5	324	59 ± 7
1:2 expansion, WSR 350, RBC (Hct ~ 40%)	125 ± 6	145	30 ± 3

Table 1: Dimensions of recirculation and stagnation zones determined from experiments and flow simulations for different flow conditions

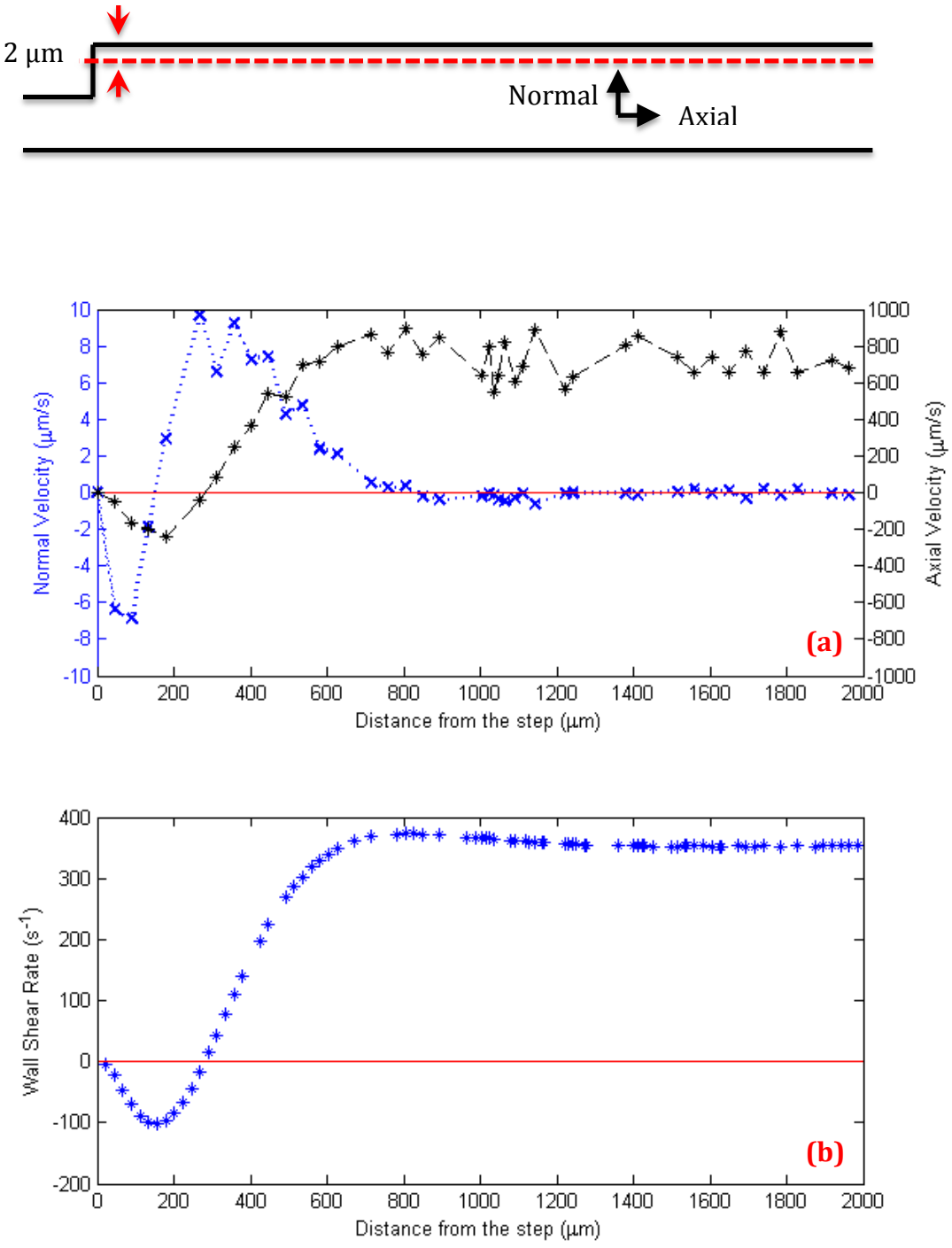

Fig. 2.4: (a) Computed normal and axial velocity components along the centerline of the chamber at a plane 2 µm from the top surface (b) Computed wall shear rate along the centerline of the chamber at the top surface

Microbubble Adhesion Pattern

Representative images of microbubble binding in the flow channel are shown in Fig. 2.5(a-d). Higher microbubble adhesion was observed around the reattachment point, while binding was lower in the regions close to the step and far downstream. The spatial variation in microbubble adhesion for each flow condition is shown in figures 2.6, 2.7, 2.8 and 2.10. Bound microbubbles were counted within sections 50 μm in length, up to a distance 2000 μm downstream of the step. To compare between flow conditions, adhesion in each 50 μm section was also quantified as percentage of all adherent microbubbles. Computed values of normal velocities, axial velocities, and wall shear rates at the corresponding locations are also plotted. The binding was lowest in all the cases closest to the step, for e.g. within a region 150 μm from the step microbubble binding was negligible for WSR 700 s^{-1}. The normal velocities in this region are directed away from the top wall. In this case the microbubbles are transported away from the wall, diminishing interactions with the substrate.

As noted above, the highest density of adherent microbubbles was found at the regions close to the reattachment zone. In the 1:2 expansion, at 350 s^{-1} the peak binding was about 2-fold higher than adhesion far downstream; at 700 s^{-1} the peak value was over 4-fold higher (Fig. 2.6 and Fig. 2.7). This was attributable to the lower binding downstream in fully developed flow at the higher shear rate, since increasing the flow rate had negligible effect on the peak fraction (~5-6% of the total bound microbubbles). In addition, the spatial extent of the region where elevated binding occurred was greater at 700 s^{-1} compared to 350 s^{-1} (800 μm and 450 μm, respectively). For the higher shear rate, this region accounted for 70% of the total binding, while for 350 s^{-1} about 36% of the

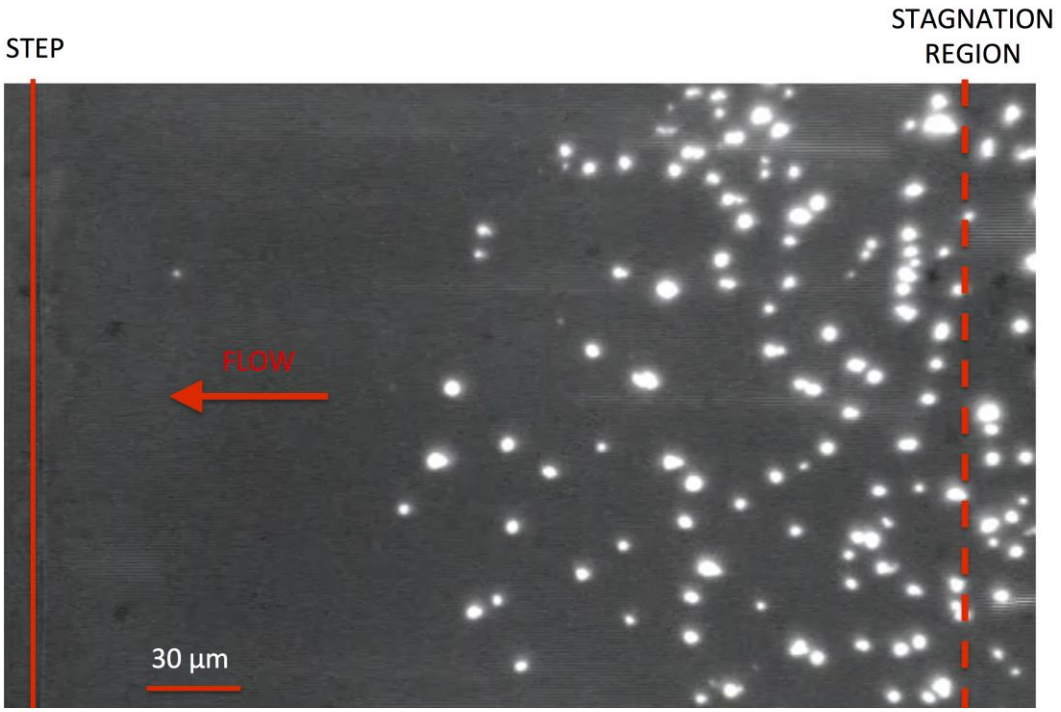

Fig. 2.5a: Microbubble adhesion to streptavidin in the region close to the step

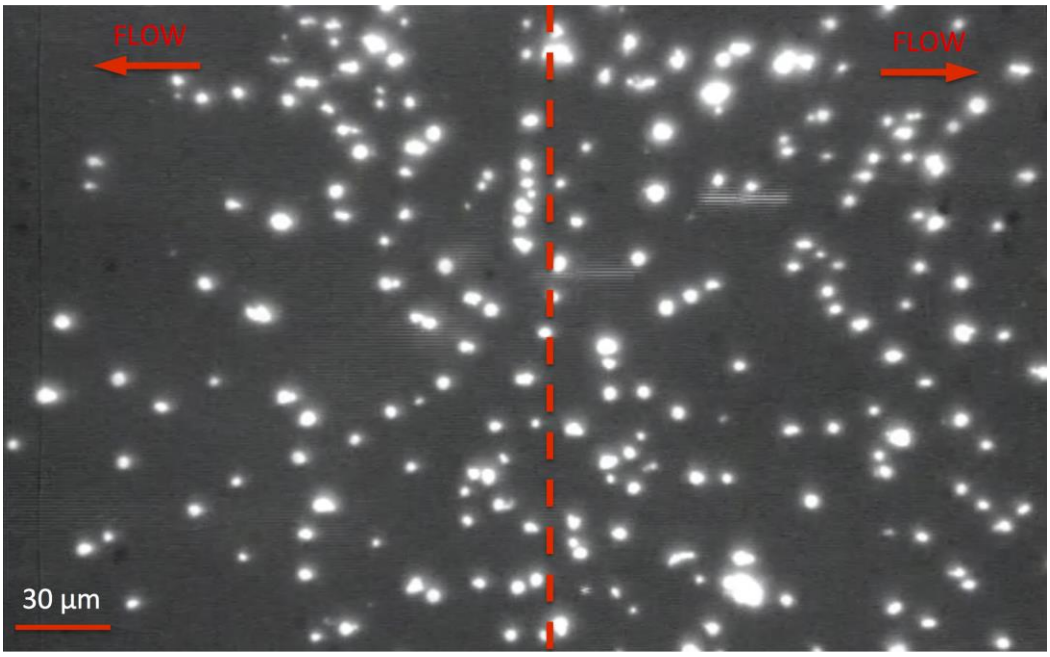

Fig. 2.5b: Microbubble adhesion to streptavidin on either side of the stagnation zone (dotted line)

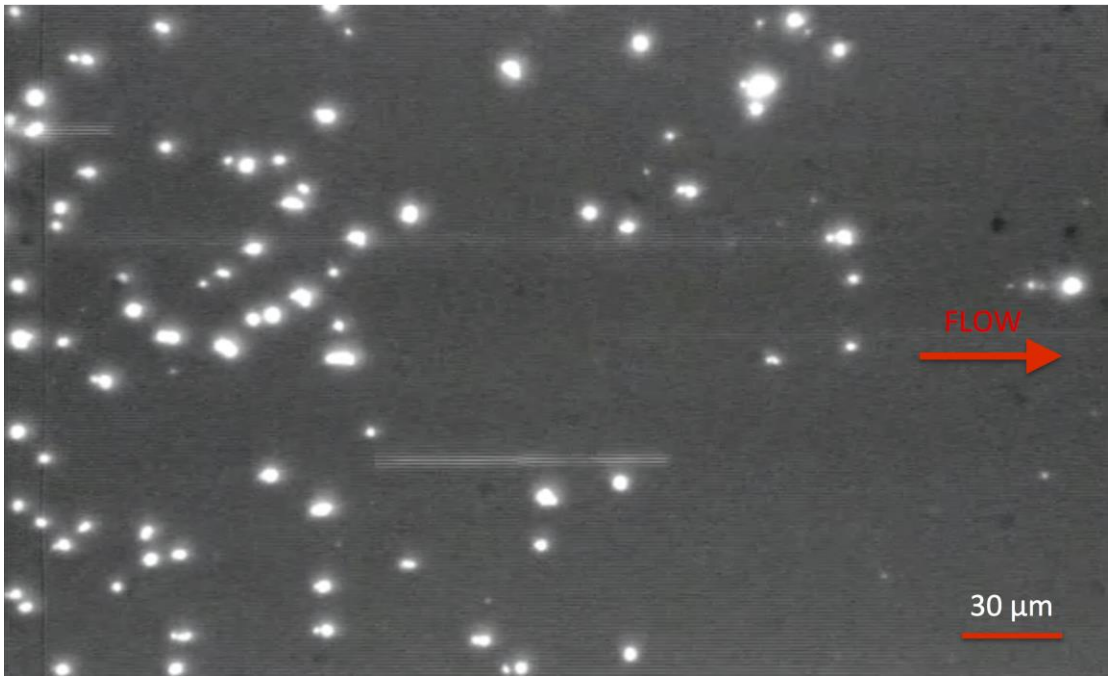

Fig. 2.5c: Microbubble adhesion to streptavidin immediately downstream of the stagnation zone. Binding is markedly lower downstream (right side of the FOV).

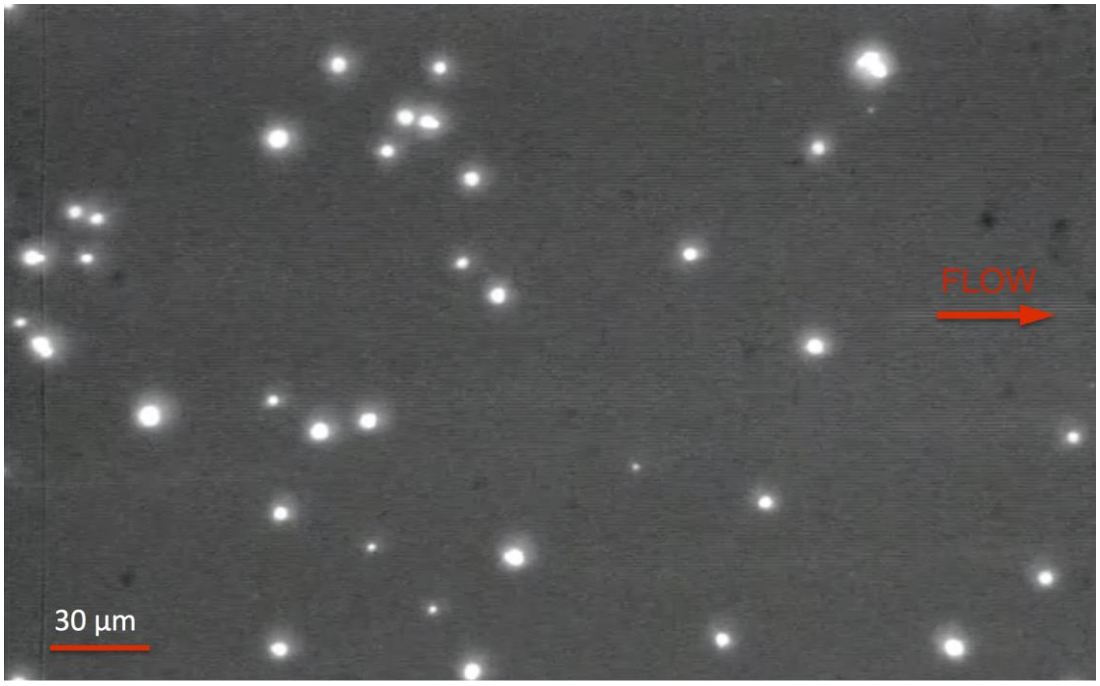

Fig. 2.5d: Microbubble adhesion to streptavidin far downstream

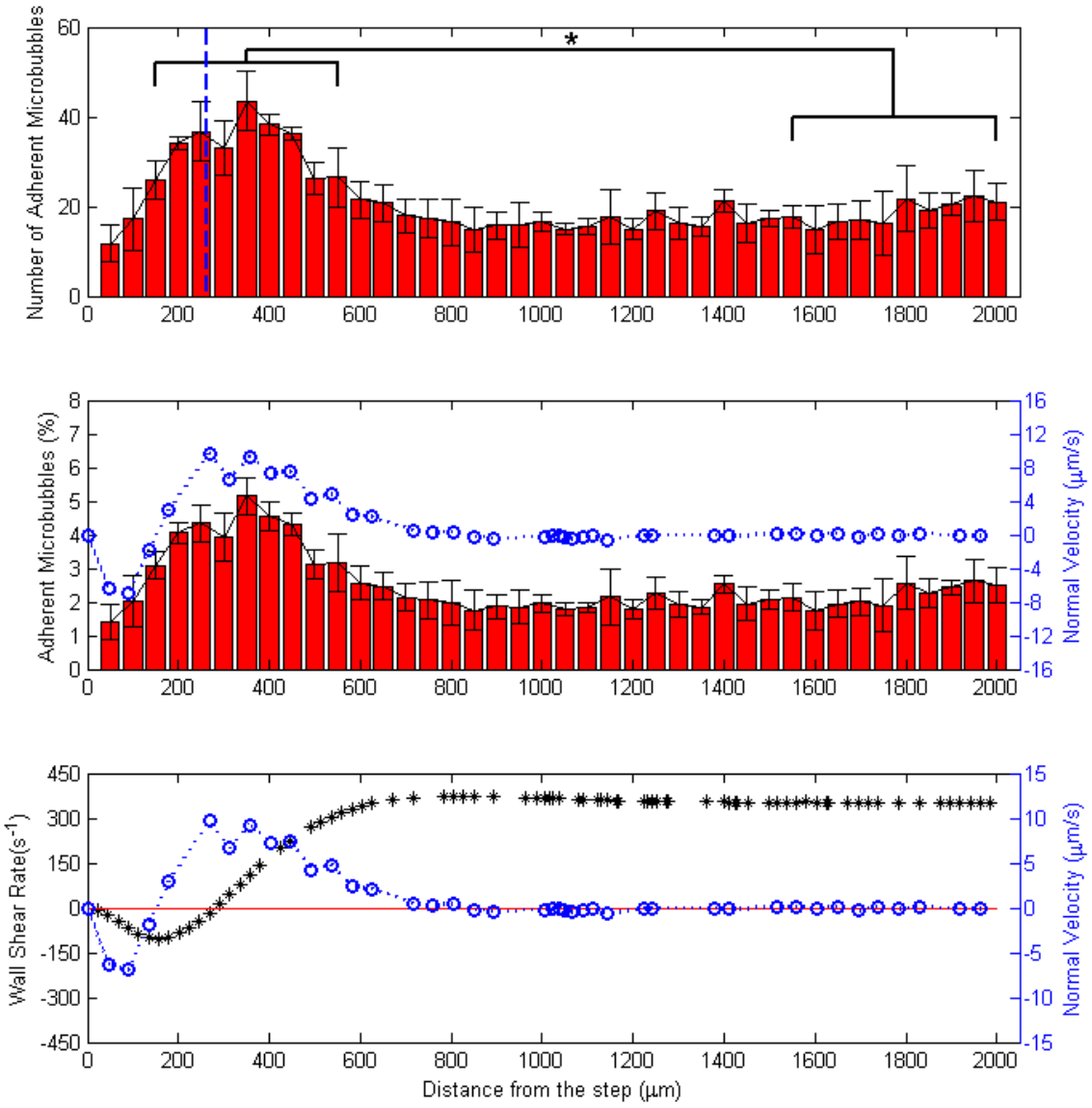

Fig. 2.6: (top) Microbubble adhesion pattern in the 1:2 expansion channel at 350 s^{-1} for microbubbles targeted to streptavidin. Blue dotted line indicates the mid-point of the stagnation zone. * indicates statistical significance ($p < 0.01$) between the binding in each 50 μm section in the region with higher binding and the average binding far downstream, n = 4; (middle) Adherent microbubbles in each section normalized to total bound bubbles, overlaid with the plot of computed normal velocities 2 μm below the reactive surface; (bottom) Plot of computed normal velocities and wall shear rate obtained from the CFD model.

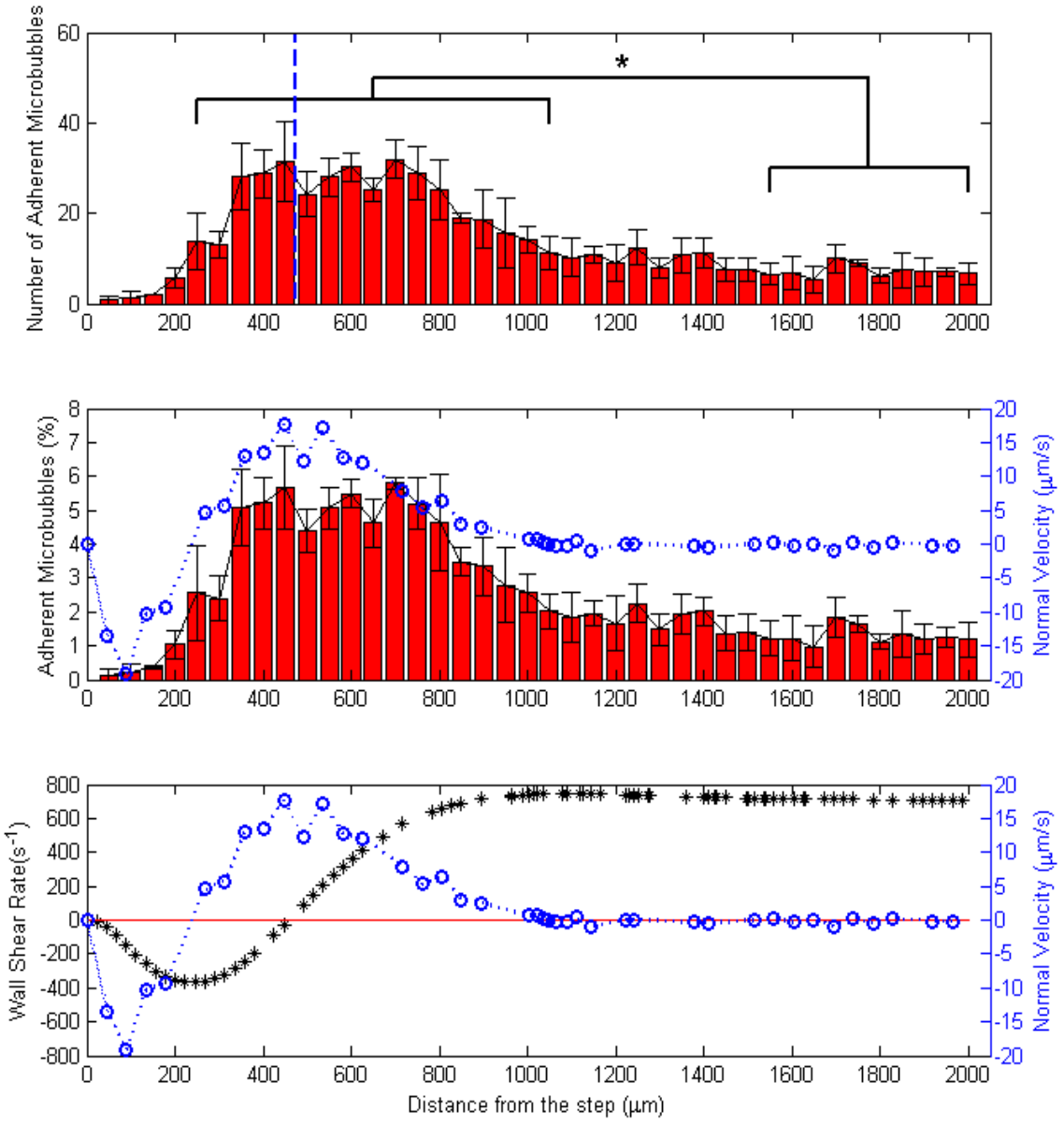

Fig. 2.7: (top) Microbubble adhesion pattern in the 1:2 expansion channel at 700 s^{-1} for microbubbles targeted to streptavidin. Blue dotted line indicates the mid-point of the stagnation zone. * indicates statistical significance ($p < 0.01$) between the binding in each 50 μm section in the region with higher binding and the average binding far downstream, n = 4; (middle) Adherent microbubbles in each section normalized to total bound bubbles, overlaid with the plot of computed normal velocities 2 μm below the reactive surface; (bottom) Plot of computed normal velocities and wall shear rate obtained from the CFD model.

microbubble adhesion occurred in this region. The mean binding in the respective regions relative to far downstream was enhanced by a factor of 1.8 for 350 s^{-1} and 3.2 for 700 s^{-1}. The area with elevated binding extended a greater distance downstream of the stagnation zone than upstream. In particular, at 700 s^{-1} the downstream portion was twice the length of the upstream segment. This was also reflected by the presence of normal velocities over a longer distance, suggesting the persistence of disturbed flow over a greater span downstream.

In the 1:3 expansion chamber (inlet = 127 μm, outlet = 381 μm) at 700 s^{-1}, the peak adhesion near the reattachment zone was 8-fold higher than far downstream (Fig. 2.8). The region of elevated binding spanned a length of 500 μm and accounted for 70% of the total binding. The mean binding in the region was enhanced by a factor of 5.5 relative to far downstream. In 1:3 expansion chamber, the normal velocities were slightly higher than in the 1:2 expansion and were present over a narrower region, suggesting the generation of a stronger focused jet. Microbubble adhesion for all the flow conditions in plain buffer is compared in Fig. 2.9.

Enhanced local adhesion was also observed when RBCs were introduced in the 1:2 expansion chamber at hematocrit of 40% and shear rate of 350 s^{-1}. The number of microbubbles adhering to the substrate was elevated throughout the flow path compared to PBS. But the increase in the binding near the reattachment zone was relatively modest, with the peak binding about 50% higher than far downstream. The region of higher binding was exclusively downstream of the stagnation zone. About 29% of the total binding occurred in this region and the mean binding was higher by a factor of 1.4 compared to far

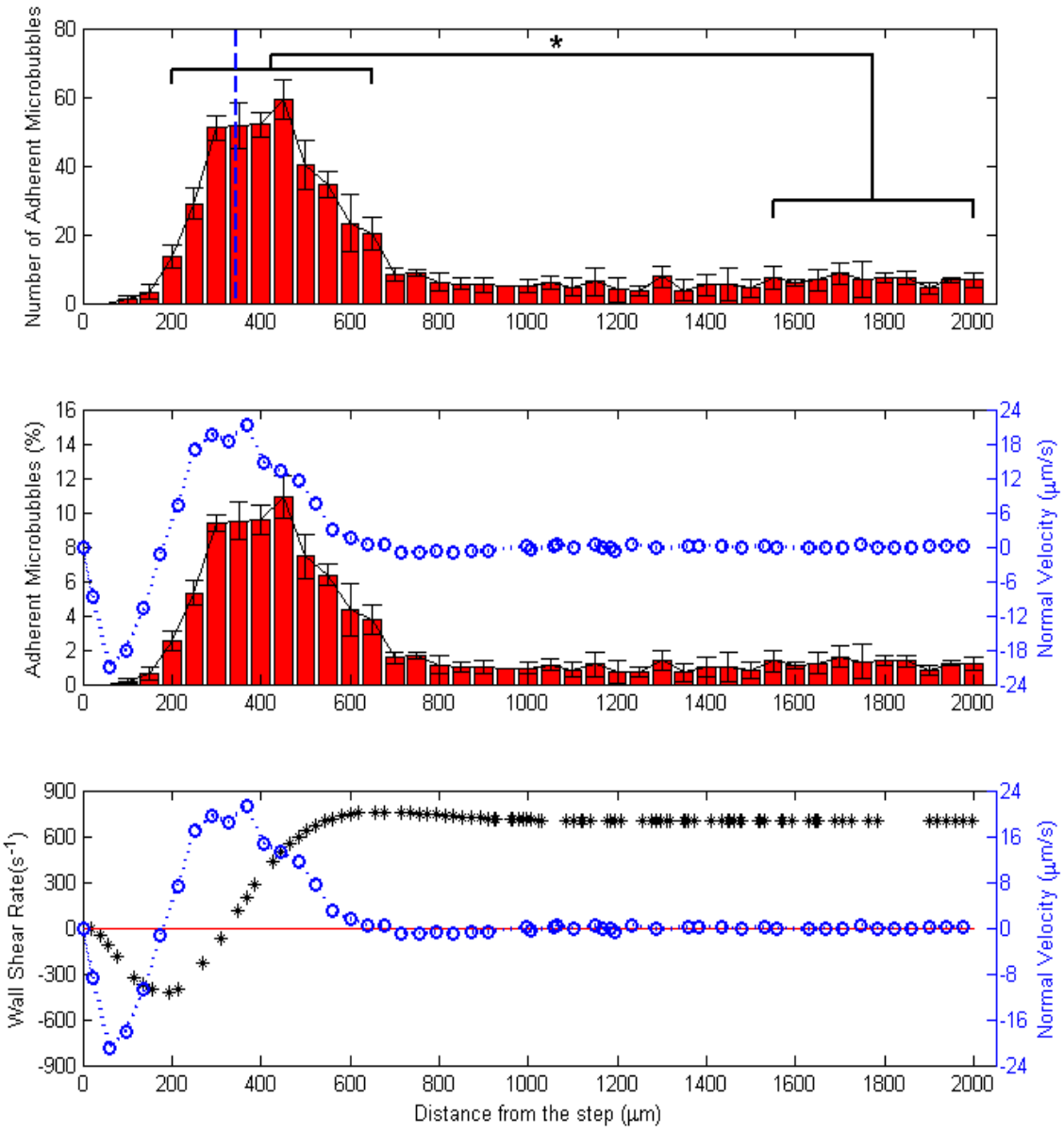

Fig. 2.8: (top) Microbubble adhesion pattern in the 1:3 expansion channel at 700 s^{-1} for microbubbles targeted to streptavidin. Blue dotted line indicates the mid-point of the stagnation zone. * indicates statistical significance ($p < 0.0001$) between the binding in each 50 μm section in the region with higher binding and the average binding far downstream, n = 3; (middle) Adherent microbubbles in each section normalized to total bound bubbles, overlaid with the plot of computed normal velocities 2 μm below the reactive surface; (bottom) Plot of computed normal velocities and wall shear rate obtained from the CFD model.

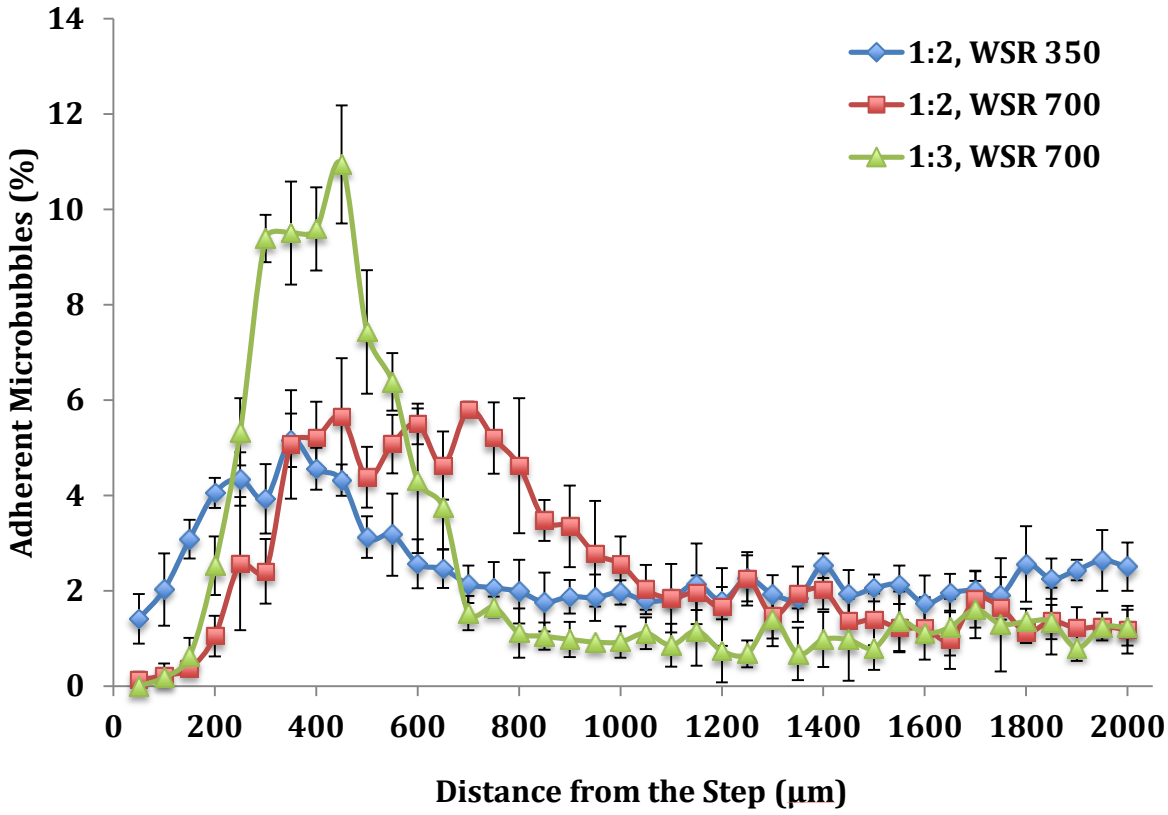

Fig 2.9: Microbubble adhesion for all flow experiments conducted in plain buffer. 1:2 and 1:3 in the legend refer to the inlet-to-outlet ratio.

downstream. The significantly diminished binding immediately upstream of the reattachment zone compared to the post-reattachment region could be the effect of the lower shear rate in the recirculation zone. As demonstrated in chap 1, RBCs enhance binding substantially at higher shear rates. Microbubble adhesion with and without RBCs at WSR 350 s^{-1} is compared in Fig. 2.11. Table 2 summarizes the main findings from the microbubble adhesion patterns for all flow conditions.

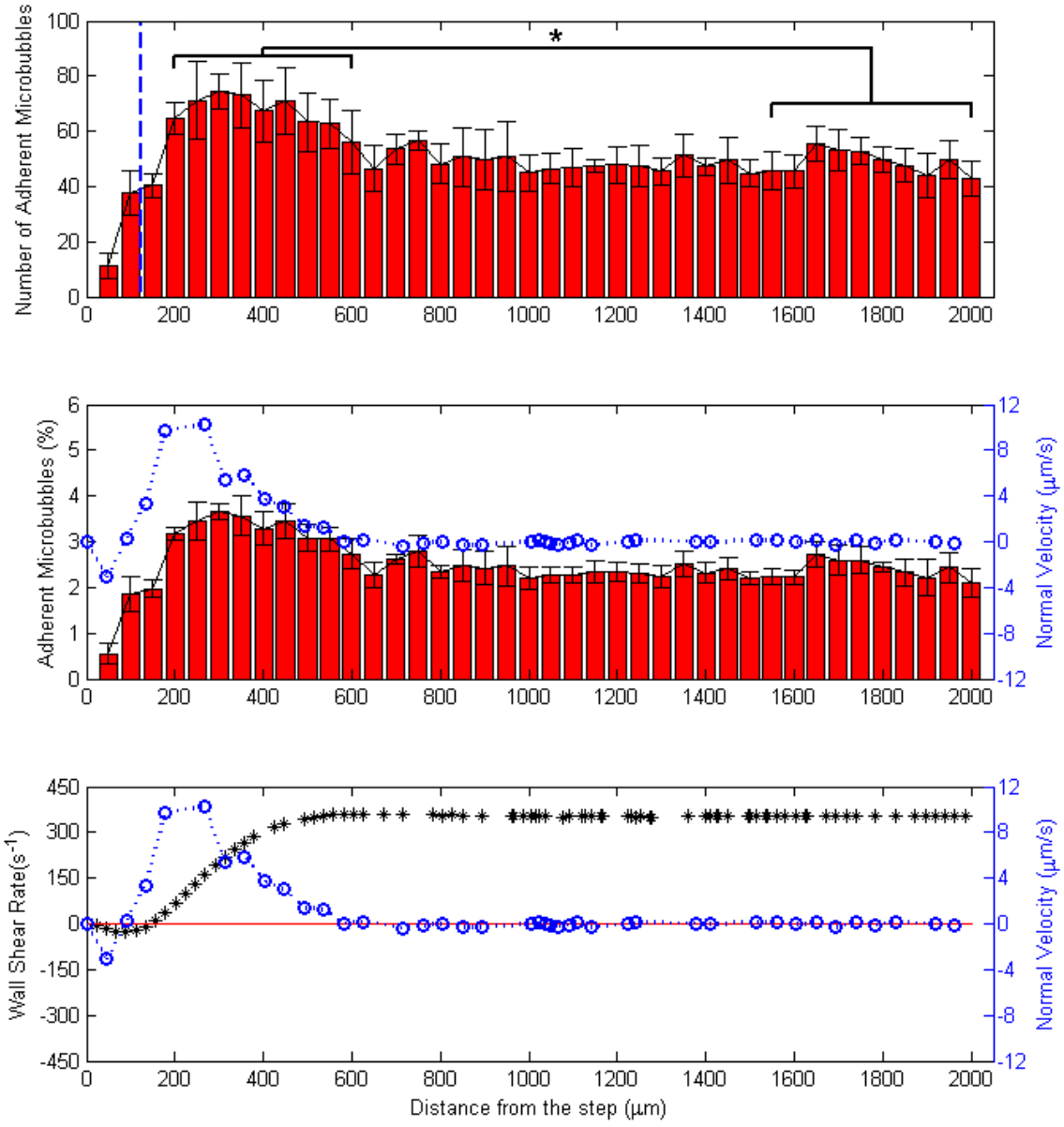

Fig. 2.10: (top) Microbubble adhesion pattern in the 1:2 expansion channel with RBCs at 40% hematocrit and shear rate 350 s^{-1} for microbubbles targeted to streptavidin. Blue dotted line indicates the mid-point of the stagnation zone. * indicates statistical significance ($p < 0.005$) between the binding in each 50 μm section in the region with higher binding and the average binding far downstream, n = 4; (middle) Adherent microbubbles in each section normalized to total bound bubbles, overlaid with the plot of normal velocities computed 2 μm below the reactive surface; (bottom) Plot of computed normal velocities and wall shear rate obtained from the CFD model assuming fluid viscosity of 3 cP.

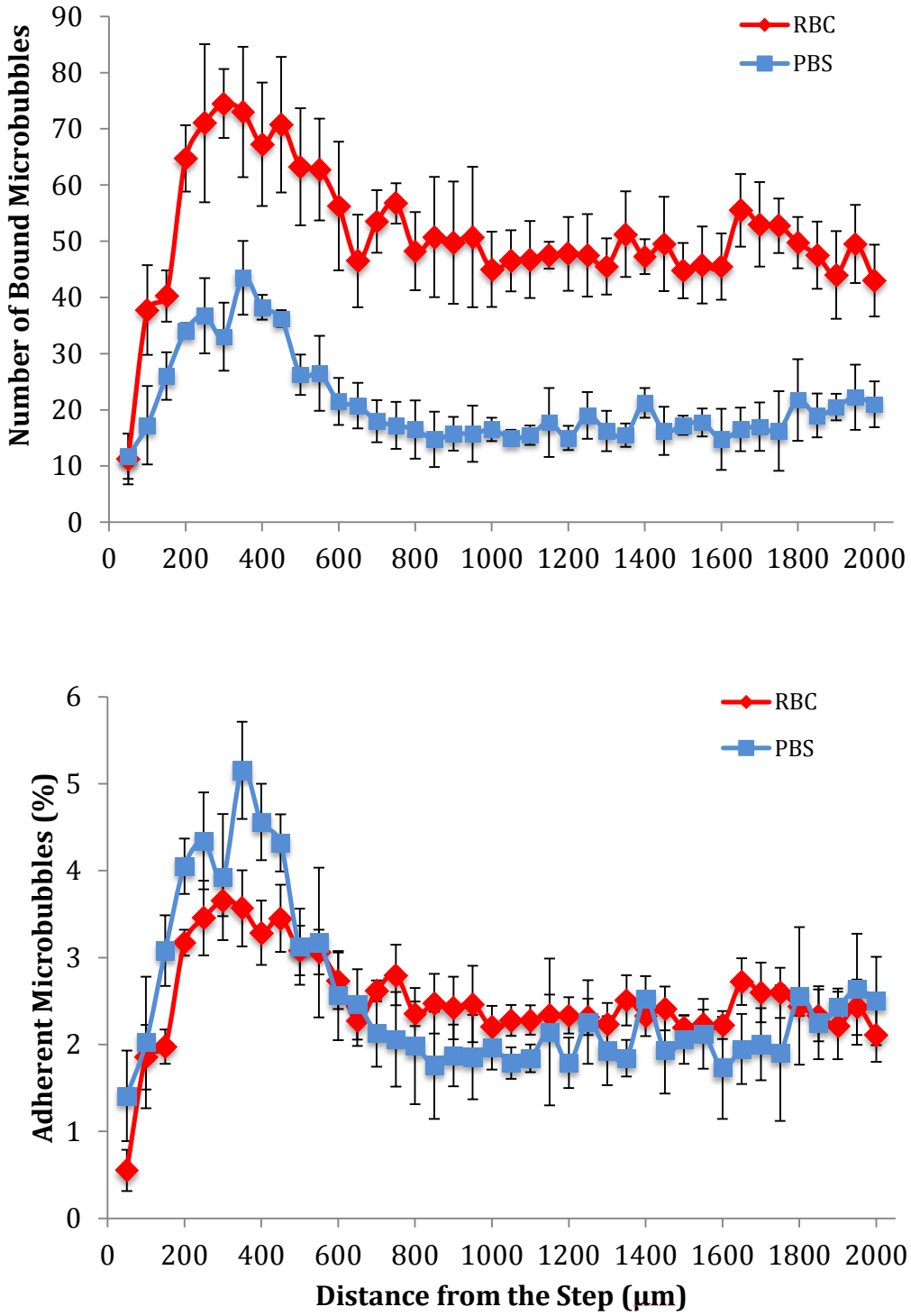

Fig. 2.11: Microbubble adhesion with and without RBCs for the 1:2 expansion at 350 s^{-1}. (top) Number of bound microbubbles as a function of distance from the step; (bottom) Adhesion expressed as percentage of all adherent microbubbles.

Chamber expansion ratio	Shear Rate (s^{-1})	Length of the Region with Elevated Binding (μm)	Peak Binding/Binding Far Downstream	Mean Enhancement in Binding relative to Far Downstream	% of total adherent microbubbles in the region with elevated binding
1:2	350	450	2.1	1.8	36
1:2	700	850	4.3	3.2	70
1:3	700	500	8	5.5	69
1:2	350 (RBCs)	400	1.5	1.4	29

Table 2: Features of microbubble adhesion pattern under different flow conditions

Discussion

In the present work we analyzed the effect of disturbed flow on the adhesion of microbubbles using a backward step flow chamber. Recirculating flow established a region of augmented microbubble adhesion in the vicinity of the reattachment zone. With 1:2 expansion ratio, the peak adhesion in the region relative to far downstream was greater at higher shear rates (4-fold at 700 s^{-1} vs 2-fold at 350 s^{-1}). The mean binding in this region was enhanced by a factor of 3.2 and 1.8 at shear rates 700 s^{-1} and 350 s^{-1}, respectively. With step expansion ratio of 1:3, the peak and mean adhesion in the region of elevated binding was enhanced 8-fold and 5-fold relative to far downstream, respectively. Furthermore, the region of higher binding had a greater span when the shear rate was increased and lower span when the expansion ratio was changed from 1:2 to 1:3. The presence of RBCs at

physiologic hematocrit resulted in a modest local increase in adhesion compared to far downstream. The enhancement with RBCs was lower compared to that observed with plain buffer (40% higher binding with RBCs compared to about 80% higher with PBS).

The major findings of this study are in line with previous work in the context of leukocyte and platelet adhesion under disturbed flow conditions. Skilbeck et al. isolated the effects of disturbed flow on leukocyte adhesion to P-selectin in dilute cell suspensions and demonstrated that most of the adhesion occurred within 800 μm from the step (reattachment zone ~300 μm from the step) at 300 s^{-1} [83]. Local enhancement of leukocyte adhesion was found to occur in whole blood too. With RBCs the length of the recirculation zone was reduced and leukocyte adhesion was two-fold higher immediately downstream of the stagnation zone than immediately upstream [85]. The microbubble binding around the reattachment zone showed similar pattern in the presence of RBCs: binding was 70% higher immediately downstream of the reattachment zone compared to upstream. Platelet adhesion to collagen in recirculating flow revealed a slightly different pattern [87]. Peak adhesion occurred *within* the eddy zone, midway between the step and the reattachment zone, and the peak value was 50-60% higher than the adhesion downstream. A pronounced dip in adhesion was observed in the stagnation zone itself (although statistical testing was not reported). This was presumed to be due to the curving away of flow streamlines from the stagnation zone and the consequent deposition of platelets at the outer edges of the zone. A drop in adhesion at the stagnation zone was noticeable in microbubble adhesion at 350 s^{-1}, but it was not significantly different from the neighboring segments. RBCs enhanced platelet adhesion everywhere in the flow path in a hematocrit dependent manner, but the ratio of peak to far downstream binding was

unaffected and remained about 1.6, nearly identical to the enhancement in microbubble adhesion with RBCs (peak to far downstream binding ratio ~1.5).

Shear rate and normal velocities were critical determinants of the spatial distribution of microbubble adhesion. Peak adhesion coincided with high normal velocities towards the wall or low shear rates. In the immediate neighborhood of the reattachment zone where microbubble adhesion was highest, both conditions were present. Microbubble residence times are longer near the reattachment zone as result of low axial velocities and shear rates, providing a favorable environment for binding. In addition, the presence of positive normal fluid velocity correlated well with higher levels of adhesion in PBS (r^2 values were 0.91 for 1:2 expansion at 350 s^{-1}, 0.81 for 1:2 expansion at 700 s^{-1}, and 0.83 for 1:3 expansion at 700 s^{-1}), suggesting that convective transport of microbubbles in the normal direction strongly influences targeting. The wall-normal convective transport brings a particle in close proximity to the surface, enhancing the likelihood of receptor-ligand encounter as compared with only diffusion. Another effect is that in the regions with normal fluid motion microbubbles that do not bind at the initial point of contact continue traveling in close proximity to the wall due to the wall-directed fluid pressure, increasing the probability of adhesion. In sum, convective transport towards the wall would explain the elevated binding observed in regions downstream of the reattachment zone, where shear rates are no longer low. Conversely, high negative normal velocities were associated with the lowest binding, even at low shear rates. Microbubble transport in the upstream half of the recirculation zone was directed away from the wall, resulting in minimal binding in the region.

Binding of targeted microbubbles in vivo in fast flow environments like the aortic arch has previously been reported [13, 14]. In view of the low adhesion efficiency of microbubbles *in vitro*, the basis of adhesion under these conditions is poorly understood. The presence of RBCs and pulsatility of flow are relevant factors that could enhance binding. The aortic arch, with its loop structure, multiple bifurcations at the top of the arch and high flow rate, is an outstanding example of a vascular region where disturbed flow conditions exist [89-91]. The flow disturbances provide an additional mechanism for microbubble adhesion in the aortic arch and more generally around stenoses and bifurcations. In the large arteries of the body the inertial forces are dominant, especially during the peak systolic phase of the cardiac cycle. The Reynolds number during this phase can range from ~1000 in the common carotid artery to ~6000 in the aorta. This results in the formation of complicated secondary flow structures including vortices and helical flow patterns, as reported in several studies [92-96]. At high velocities and for finite particle size, particle inertia is also factor. Near stagnation zones the streamlines undergo sharp change in direction as a result of flow reversal, but the particle trajectory deviates from the streamline due to its inertia and crosses to a new streamline, or impinges on to the wall when sufficiently close [97]. Particle deviations from curving streamlines are a common phenomenon, especially at high flow velocities. In a physiologic context, it is known to be one of the basic mechanisms for particle deposition in the lung airways [98]. Along with gravitational and diffusive effects, inertial impingement is one of the rudimentary means of particle deposition on a surface. Its role has been emphasized in vascular particle deposition models as well [99]. Microbubble binding in arteries would likely be enhanced due to particle inertial effects. Around a bifurcation, higher levels of binding are to be expected at the carina and

downstream at the outer walls of the daughter vessels. Similarly, adhesion would likely be greater downstream of a moderate or severe stenosis compared to a mild one. Overall, the presence of disturbed flow features would result in spatially non-uniform adhesion in these hemodynamic regions.

We demonstrated that microbubble adhesion patterns are significantly influenced by flow streamlines as well as local wall shear rates. Velocity components normal to the wall are important in establishing adhesion as they affect the convective transport of microbubbles towards or away from the wall. The presence of disturbed flow aids adhesion and provides a mechanism for microbubble adhesion in regions with high flow rates. The results suggest that binding in the arterial system around bifurcations, stenoses, and aneurysms is likely to be highly non-uniform spatially. Future studies would involve targeting against a physiologically relevant marker. In addition, a comprehensive understanding of the mechanisms of binding in arteries would require an investigation of the role of flow pulsatility.

References

[1] R. Mirnezami, J. Nicholson, A. Darzi, Preparing for precision medicine, The New England journal of medicine, 366 (2012) 489-491.

[2] T.F. Massoud, S.S. Gambhir, Molecular imaging in living subjects: seeing fundamental biological processes in a new light, Genes & development, 17 (2003) 545-580.

[3] A.L. Klibanov, Targeted delivery of gas-filled microspheres, contrast agents for ultrasound imaging, Advanced drug delivery reviews, 37 (1999) 139-157.

[4] J.R. Lindner, Microbubbles in medical imaging: current applications and future directions, Nature reviews. Drug discovery, 3 (2004) 527-532.

[5] A.L. Klibanov, P.T. Rasche, M.S. Hughes, J.K. Wojdyla, K.P. Galen, J.H. Wible, Jr., G.H. Brandenburger, Detection of individual microbubbles of ultrasound contrast agents: imaging of free-floating and targeted bubbles, Invest Radiol, 39 (2004) 187-195.

[6] B. Haider, R.Y. Chiao, Higher order nonlinear ultrasonic imaging., IEEE Ultrasonics Symposium, 2 (1999) 1527-1531.

[7] P. PJ., Contrast pulse sequences (CPS): imaging nonlinear microbubbles, IEEE Ultrasonics Symposium, 2 (2001) 1739-1745.

[8] S. Kaul, Myocardial contrast echocardiography: a 25-year retrospective, Circulation, 118 (2008) 291-308.

[9] M.W. Keller, S.S. Segal, S. Kaul, B. Duling, The Behavior of Sonicated Albumin Microbubbles within the Microcirculation - a Basis for Their Use during Myocardial Contrast Echocardiography, Circ Res, 65 (1989) 458-467.

[10] J.R. Lindner, J. Song, A.R. Jayaweera, J. Sklenar, S. Kaul, Microvascular rheology of Definity microbubbles after intra-arterial and intravenous administration, Journal of the American Society of Echocardiography : official publication of the American Society of Echocardiography, 15 (2002) 396-403.

[11] K. Wei, A.R. Jayaweera, S. Firoozan, A. Linka, D.M. Skyba, S. Kaul, Quantification of myocardial blood flow with ultrasound-induced destruction of microbubbles administered as a constant venous infusion, Circulation, 97 (1998) 473-483.

[12] S. Unnikrishnan, A.L. Klibanov, Microbubbles as ultrasound contrast agents for molecular imaging: preparation and application, AJR. American journal of roentgenology, 199 (2012) 292-299.

[13] B.A. Kaufmann, J.M. Sanders, C. Davis, A. Xie, P. Aldred, I.J. Sarembock, J.R. Lindner, Molecular imaging of inflammation in atherosclerosis with targeted ultrasound detection of vascular cell adhesion molecule-1, Circulation, 116 (2007) 276-284.

[14] B.A. Kaufmann, C.L. Carr, J.T. Belcik, A. Xie, Q. Yue, S. Chadderdon, E.S. Caplan, J. Khangura, S. Bullens, S. Bunting, J.R. Lindner, Molecular Imaging of the Initial Inflammatory Response in Atherosclerosis Implications for Early Detection of Disease, Arterioscl Throm Vas, 30 (2010) 54-U132.

[15] B.A. Kaufmann, C. Lewis, A. Xie, A. Mirza-Mohd, J.R. Lindner, Detection of recent myocardial ischaemia by molecular imaging of P-selectin with targeted contrast echocardiography, Eur Heart J, 28 (2007) 2011-2017.

[16] J.R. Lindner, J. Song, J. Christiansen, A.L. Klibanov, F. Xu, K. Ley, Ultrasound assessment of inflammation and renal tissue injury with microbubbles targeted to P-selectin, Circulation, 104 (2001) 2107-2112.

[17] C. Bachmann, A.L. Klibanov, T.S. Olson, J.R. Sonnenschein, J. Rivera-Nieves, F. Cominelli, K.F. Ley, J.R. Lindner, T.T. Pizarro, Targeting mucosal addressin cellular adhesion molecule (MAdCAM)-1 to noninvasively image experimental Crohn's disease, Gastroenterology, 130 (2006) 8-16.

[18] N. Deshpande, A.M. Lutz, Y. Ren, K. Foygel, L. Tian, M. Schneider, R. Pai, P.J. Pasricha, J.K. Willmann, Quantification and Monitoring of Inflammation in Murine Inflammatory Bowel Disease with Targeted Contrast-enhanced US, Radiology, 262 (2012) 172-180.

[19] J.K. Willmann, R. Paulmurugan, K. Chen, O. Gheysens, M. Rodriguez-Porcel, A.M. Lutz, I.Y. Chen, X. Chen, S.S. Gambhir, US imaging of tumor angiogenesis with microbubbles targeted to vascular endothelial growth factor receptor type 2 in mice, Radiology, 246 (2008) 508-518.

[20] C.R. Anderson, J.J. Rychak, M. Backer, J. Backer, K. Ley, A.L. Klibanov, scVEGF microbubble ultrasound contrast agents: a novel probe for ultrasound molecular imaging of tumor angiogenesis, Invest Radiol, 45 (2010) 579-585.

[21] S. Pochon, I. Tardy, P. Bussat, T. Bettinger, J. Brochot, M. von Wronski, L. Passantino, M. Schneider, BR55: A Lipopeptide-Based VEGFR2-Targeted Ultrasound Contrast Agent for Molecular Imaging of Angiogenesis, Invest Radiol, 45 (2010) 89-95.

[22] M.A. Pysz, K. Foygel, J. Rosenberg, S.S. Gambhir, M. Schneider, J.K. Willmann, Antiangiogenic cancer therapy: monitoring with molecular US and a clinically translatable contrast agent (BR55), Radiology, 256 (2010) 519-527.

[23] C.R. Anderson, X. Hu, H. Zhang, J. Tlaxca, A.E. Decleves, R. Houghtaling, K. Sharma, M. Lawrence, K.W. Ferrara, J.J. Rychak, Ultrasound molecular imaging of tumor angiogenesis with an integrin targeted microbubble contrast agent, Invest Radiol, 46 (2011) 215-224.

[24] H. Wijkstra, Smeenge, M., Rosette, J.J.M.C.H. de la, Pochon, S., Tranquart, F., Targeted microbubble prostate cancer imaging with BR55, in: Proceedings of the 17th European Symposium on Ultrasound Contrast Imaging, Rotterdam, The Netherlands, Jan 19-20, 2012.

[25] W.H. Wright, T.P. McCreery, E.A. Krupinski, P.J. Lund, S.H. Smyth, M.R. Baker, R.L. Hulett, E.C. Unger, Evaluation of new thrombus-specific ultrasound contrast agent, Acad Radiol, 5 (1998) S240-S242.

[26] Y.Q. Wu, E.C. Unger, T.P. McCreery, R.H. Sweitzer, D.K. Shen, G.L. Wu, M.D. Vielhauer, Binding and lysing of blood clots using MRX-408, Invest Radiol, 33 (1998) 880-885.

[27] P.A. Schumann, J.P. Christiansen, R.M. Quigley, T.P. McCreery, R.H. Sweitzer, E.C. Unger, J.R. Lindner, T.O. Matsunaga, Targeted-microbubble binding selectively to GPIIb IIIa receptors of platelet thrombi, Invest Radiol, 37 (2002) 587-593.

[28] R.J. Melder, L.L. Munn, S. Yamada, C. Ohkubo, R.K. Jain, Selectin- and integrin-mediated T-lymphocyte rolling and arrest on TNF-alpha-activated endothelium: augmentation by erythrocytes, Biophys J, 69 (1995) 2131-2138.

[29] L.L. Munn, R.J. Melder, R.K. Jain, Role of erythrocytes in leukocyte-endothelial interactions: mathematical model and experimental validation, Biophys J, 71 (1996) 466-478.

[30] R.J. Melder, J. Yuan, L.L. Munn, R.K. Jain, Erythrocytes enhance lymphocyte rolling and arrest in vivo, Microvasc Res, 59 (2000) 316-322.

[31] E.C. Eckstein, A.W. Tilles, F.J. Millero, 3rd, Conditions for the occurrence of large near-wall excesses of small particles during blood flow, Microvasc Res, 36 (1988) 31-39.

[32] P. Charoenphol, R.B. Huang, O. Eniola-Adefeso, Potential role of size and hemodynamics in the efficacy of vascular-targeted spherical drug carriers, Biomaterials, 31 (2010) 1392-1402.

[33] V.T. Turitto, H.R. Baumgartner, Platelet interaction with subendothelium in a perfusion system: physical role of red blood cells, Microvasc Res, 9 (1975) 335-344.

[34] W.S. Uijttewaal, E.J. Nijhof, P.J. Bronkhorst, E. Den Hartog, R.M. Heethaar, Near-wall excess of platelets induced by lateral migration of erythrocytes in flowing blood, The American journal of physiology, 264 (1993) H1239-1244.

[35] A.L. Klibanov, J.J. Rychak, W.C. Yang, S. Alikhani, B. Li, S. Acton, J.R. Lindner, K. Ley, S. Kaul, Targeted ultrasound contrast agent for molecular imaging of inflammation in high-shear flow, Contrast media & molecular imaging, 1 (2006) 259-266.

[36] E.A. Ferrante, J.E. Pickard, J. Rychak, A. Klibanov, K. Ley, Dual targeting improves microbubble contrast agent adhesion to VCAM-1 and P-selectin under flow, J Control Release, 140 (2009) 100-107.

[37] A.M. Takalkar, A.L. Klibanov, J.J. Rychak, J.R. Lindner, K. Ley, Binding and detachment dynamics of microbubbles targeted to P-selectin under controlled shear flow, J Control Release, 96 (2004) 473-482.

[38] J. Owen, P. Grove, P. Rademeyer, E. Stride, The influence of blood on targeted microbubbles, Journal of the Royal Society, Interface / the Royal Society, 11 (2014) 20140622.

[39] S. Kim, R.L. Kong, A.S. Popel, M. Intaglietta, P.C. Johnson, Temporal and spatial variations of cell-free layer width in arterioles, American journal of physiology. Heart and circulatory physiology, 293 (2007) H1526-1535.

[40] H.L. Goldsmith, J.C. Marlow, Flow Behavior of Erythrocytes .2. Particle Motions in Concentrated Suspensions of Ghost Cells, J Colloid Interf Sci, 71 (1979) 383-407.

[41] H.L. Goldsmith, T. Karino, Microscopic Considerations - Motions of Individual Particles, Ann Ny Acad Sci, 283 (1977) 241-255.

[42] H.L. Goldsmith, Red cell motions and wall interactions in tube flow, Federation proceedings, 30 (1971) 1578-1590.

[43] K.B. Abbitt, G.B. Nash, Rheological properties of the blood influencing selectin-mediated adhesion of flowing leukocytes, American journal of physiology. Heart and circulatory physiology, 285 (2003) H229-240.

[44] P.A. Aarts, S.A. van den Broek, G.W. Prins, G.D. Kuiken, J.J. Sixma, R.M. Heethaar, Blood platelets are concentrated near the wall and red blood cells, in the center in flowing blood, Arteriosclerosis, 8 (1988) 819-824.

[45] G.J. Tangelder, H.C. Teirlinck, D.W. Slaaf, R.S. Reneman, Distribution of blood platelets flowing in arterioles, The American journal of physiology, 248 (1985) H318-323.

[46] A.W. Tilles, E.C. Eckstein, The near-wall excess of platelet-sized particles in blood flow: its dependence on hematocrit and wall shear rate, Microvasc Res, 33 (1987) 211-223.

[47] L. Crowl, A.L. Fogelson, Analysis of mechanisms for platelet near-wall excess under arterial blood flow conditions, J Fluid Mech, 676 (2011) 348-375.

[48] K. Vahidkhah, S.L. Diamond, P. Bagchi, Hydrodynamic interaction between a platelet and an erythrocyte: effect of erythrocyte deformability, dynamics, and wall proximity, Journal of biomechanical engineering, 135 (2013) 51002.

[49] L.M. Crowl, A.L. Fogelson, Computational model of whole blood exhibiting lateral platelet motion induced by red blood cells, International journal for numerical methods in biomedical engineering, 26 (2010) 471-487.

[50] A.A. Tokarev, A.A. Butylin, E.A. Ermakova, E.E. Shnol, G.P. Panasenko, F.I. Ataullakhanov, Finite platelet size could be responsible for platelet margination effect, Biophys J, 101 (2011) 1835-1843.

[51] A.A. Tokarev, A.A. Butylin, F.I. Ataullakhanov, Platelet adhesion from shear blood flow is controlled by near-wall rebounding collisions with erythrocytes, Biophys J, 100 (2011) 799-808.

[52] D. Mori, K. Yano, K. Tsubota, T. Ishikawa, S. Wada, T. Yamaguchi, Computational study on effect of red blood cells on primary thrombus formation, Thrombosis research, 123 (2008) 114-121.

[53] J.K.W. Chesnutt, H.-C. Han, Effect of red blood cells on platelet activation and thrombus formation in tortuous arterioles, Frontiers in Bioengineering and Biotechnology, 1 (2013) 1-12.

[54] R.P. McEver, J.H. Beckstead, K.L. Moore, L. Marshall-Carlson, D.F. Bainton, GMP-140, a platelet alpha-granule membrane protein, is also synthesized by vascular endothelial cells and is localized in Weibel-Palade bodies, The Journal of clinical investigation, 84 (1989) 92-99.

[55] T.N. Mayadas, R.C. Johnson, H. Rayburn, R.O. Hynes, D.D. Wagner, Leukocyte rolling and extravasation are severely compromised in P selectin-deficient mice, Cell, 74 (1993) 541-554.

[56] A.L. Klibanov, H. Gu, J.K. Wojdyla, J.H. Wible Jr., D.H. Kim, D. Needham, F.S. Villanueva, G.H. Brandenburger, Attachment of ligands to gas-filled microbubbles via PEG spacer and lipid residues anchored at the interface, in: Proceedings of the International Symposium on Controlled Release of Bioactive Materials, Boston, MA, 1999, pp. 124-125.

[57] E.M. Sevick, R.K. Jain, Effect of red blood cell rigidity on tumor blood flow: increase in viscous resistance during hyperglycemia, Cancer research, 51 (1991) 2727-2730.

[58] J.J. Rychak, J.R. Lindner, K. Ley, A.L. Klibanov, Deformable gas-filled microbubbles targeted to P-selectin, J Control Release, 114 (2006) 288-299.

[59] S. Hernot, S. Unnikrishnan, Z. Du, T. Shevchenko, B. Cosyns, A. Broisat, J. Toczek, V. Caveliers, S. Muyldermans, T. Lahoutte, A.L. Klibanov, N. Devoogdt, Nanobody-coupled microbubbles as novel molecular tracer, J Control Release, 158 (2012) 346-353.

[60] C. Foxall, S.R. Watson, D. Dowbenko, C. Fennie, L.A. Lasky, M. Kiso, A. Hasegawa, D. Asa, B.K. Brandley, The three members of the selectin receptor family recognize a common

carbohydrate epitope, the sialyl Lewis(x) oligosaccharide, The Journal of cell biology, 117 (1992) 895-902.

[61] L.M. Kornmann, K.D. Reesink, R.S. Reneman, A.P. Hoeks, Critical appraisal of targeted ultrasound contrast agents for molecular imaging in large arteries, Ultrasound in medicine & biology, 36 (2010) 181-191.

[62] M. Saadatmand, T. Ishikawa, N. Matsuki, M. Jafar Abdekhodaie, Y. Imai, H. Ueno, T. Yamaguchi, Fluid particle diffusion through high-hematocrit blood flow within a capillary tube, Journal of biomechanics, 44 (2011) 170-175.

[63] C. Migliorini, Y. Qian, H. Chen, E.B. Brown, R.K. Jain, L.L. Munn, Red blood cells augment leukocyte rolling in a virtual blood vessel, Biophys J, 83 (2002) 1834-1841.

[64] A.H. Isfahani, J.B. Freund, Forces on a wall-bound leukocyte in a small vessel due to red cells in the blood stream, Biophys J, 103 (2012) 1604-1615.

[65] V.T. Turitto, A.M. Benis, E.F. Leonard, Platelet Diffusion in Flowing Blood, Ind Eng Chem Fund, 11 (1972) 216-&.

[66] H.L. Goldsmith, V.T. Turitto, Rheological aspects of thrombosis and haemostasis: basic principles and applications. ICTH-Report--Subcommittee on Rheology of the International Committee on Thrombosis and Haemostasis, Thrombosis and haemostasis, 55 (1986) 415-435.

[67] E.C. Eckstein, F. Belgacem, Model of platelet transport in flowing blood with drift and diffusion terms, Biophys J, 60 (1991) 53-69.

[68] D.N. Bell, S. Spain, H.L. Goldsmith, The effect of red blood cells on the ADP-induced aggregation of human platelets in flow through tubes, Thrombosis and haemostasis, 63 (1990) 112-121.

[69] G.J. Tangelder, D.W. Slaaf, A.M. Muijtjens, T. Arts, M.G. oude Egbrink, R.S. Reneman, Velocity profiles of blood platelets and red blood cells flowing in arterioles of the rabbit mesentery, Circ Res, 59 (1986) 505-514.

[70] G.J. Tangelder, D.W. Slaaf, T. Arts, R.S. Reneman, Wall shear rate in arterioles in vivo: least estimates from platelet velocity profiles, The American journal of physiology, 254 (1988) H1059-1064.

[71] Z. Wu, A. Curaj, S. Fokong, E.A. Liehn, C. Weber, T. Lammers, F. Kiessling, M. Zandvoort van, Rhodamine-loaded intercellular adhesion molecule-1-targeted microbubbles for dual-modality imaging under controlled shear stresses, Circulation. Cardiovascular imaging, 6 (2013) 974-981.

[72] K.C. Chang, D.A. Hammer, Influence of direction and type of applied force on the detachment of macromolecularly-bound particles from surfaces, Langmuir, 12 (1996) 2271-2282.

[73] V.R. Shinde Patil, C.J. Campbell, Y.H. Yun, S.M. Slack, D.J. Goetz, Particle diameter influences adhesion under flow, Biophys J, 80 (2001) 1733-1743.

[74] P. Dayton, A. Klibanov, G. Brandenburger, K. Ferrara, Acoustic radiation force in vivo: a mechanism to assist targeting of microbubbles, Ultrasound in medicine & biology, 25 (1999) 1195-1201.

[75] S. Zhao, M. Borden, S.H. Bloch, D. Kruse, K.W. Ferrara, P.A. Dayton, Radiation-force assisted targeting facilitates ultrasonic molecular imaging, Molecular imaging, 3 (2004) 135-148.

[76] J.J. Rychak, A.L. Klibanov, J.A. Hossack, Acoustic radiation force enhances targeted delivery of ultrasound contrast microbubbles: In vitro verification, Ieee T Ultrason Ferr, 52 (2005) 421-433.

[77] J.J. Rychak, A.L. Klibanov, K.F. Ley, J.A. Hossack, Enhanced targeting of ultrasound contrast agents using acoustic radiation force, Ultrasound in medicine & biology, 33 (2007) 1132-1139.

[78] P.J. Frinking, I. Tardy, M. Theraulaz, M. Arditi, J. Powers, S. Pochon, F. Tranquart, Effects of acoustic radiation force on the binding efficiency of BR55, a VEGFR2-specific ultrasound contrast agent, Ultrasound in medicine & biology, 38 (2012) 1460-1469.

[79] C. Cheng, D. Tempel, R. van Haperen, H.C. de Boer, D. Segers, M. Huisman, A.J. van Zonneveld, P.J. Leenen, A. van der Steen, P.W. Serruys, R. de Crom, R. Krams, Shear stress-induced changes in atherosclerotic plaque composition are modulated by chemokines, The Journal of clinical investigation, 117 (2007) 616-626.

[80] J.J. Chiu, C.N. Chen, P.L. Lee, C.T. Yang, H.S. Chuang, S. Chien, S. Usami, Analysis of the effect of disturbed flow on monocytic adhesion to endothelial cells, Journal of biomechanics, 36 (2003) 1883-1895.

[81] K.M. Barber, A. Pinero, G.A. Truskey, Effects of recirculating flow on U-937 cell adhesion to human umbilical vein endothelial cells, The American journal of physiology, 275 (1998) H591-599.

[82] D.N. Ku, D.P. Giddens, Pulsatile flow in a model carotid bifurcation, Arteriosclerosis, 3 (1983) 31-39.

[83] C. Skilbeck, S.M. Westwood, P.G. Walker, T. David, G.B. Nash, Population of the vessel wall by leukocytes binding to P-selectin in a model of disturbed arterial flow, Arteriosclerosis, thrombosis, and vascular biology, 21 (2001) 1294-1300.

[84] C. Skilbeck, S.M. Westwood, P.G. Walker, T. David, G.B. Nash, Dependence of adhesive behavior of neutrophils on local fluid dynamics in a region with recirculating flow, Biorheology, 38 (2001) 213-227.

[85] C.A. Skilbeck, P.G. Walker, T. David, G.B. Nash, Disturbed flow promotes deposition of leucocytes from flowing whole blood in a model of a damaged vessel wall, British journal of haematology, 126 (2004) 418-427.

[86] C.N. Chen, S.F. Chang, P.L. Lee, K. Chang, L.J. Chen, S. Usami, S. Chien, J.J. Chiu, Neutrophils, lymphocytes, and monocytes exhibit diverse behaviors in transendothelial and subendothelial migrations under coculture with smooth muscle cells in disturbed flow, Blood, 107 (2006) 1933-1942.

[87] T. Karino, H.L. Goldsmith, Adhesion of human platelets to collagen on the walls distal to a tubular expansion, Microvasc Res, 17 (1979) 238-262.

[88] P. Charoenphol, P.J. Onyskiw, M. Carrasco-Teja, O. Eniola-Adefeso, Particle-cell dynamics in human blood flow: Implications for vascular-targeted drug delivery, Journal of biomechanics, 45 (2012) 2822-2828.

[89] A. Feintuch, P. Ruengsakulrach, A. Lin, J. Zhang, Y.Q. Zhou, J. Bishop, L. Davidson, D. Courtman, F.S. Foster, D.A. Steinman, R.M. Henkelman, C.R. Ethier, Hemodynamics in the mouse aortic arch as assessed by MRI, ultrasound, and numerical modeling, American journal of physiology. Heart and circulatory physiology, 292 (2007) H884-892.

[90] P.E. Vincent, A.M. Plata, A.A. Hunt, P.D. Weinberg, S.J. Sherwin, Blood flow in the rabbit aortic arch and descending thoracic aorta, Journal of the Royal Society, Interface / the Royal Society, 8 (2011) 1708-1719.

[91] J. Burk, P. Blanke, Z. Stankovic, A. Barker, M. Russe, J. Geiger, A. Frydrychowicz, M. Langer, M. Markl, Evaluation of 3D blood flow patterns and wall shear stress in the normal and dilated thoracic aorta using flow-sensitive 4D CMR, Journal of cardiovascular magnetic resonance : official journal of the Society for Cardiovascular Magnetic Resonance, 14 (2012) 84.

[92] M. Motomiya, T. Karino, Flow patterns in the human carotid artery bifurcation, Stroke; a journal of cerebral circulation, 15 (1984) 50-56.

[93] D.N. Ku, D.P. Giddens, D.J. Phillips, D.E. Strandness, Jr., Hemodynamics of the normal human carotid bifurcation: in vitro and in vivo studies, Ultrasound in medicine & biology, 11 (1985) 13-26.

[94] D.N. Ku, D.P. Giddens, C.K. Zarins, S. Glagov, Pulsatile flow and atherosclerosis in the human carotid bifurcation. Positive correlation between plaque location and low oscillating shear stress, Arteriosclerosis, 5 (1985) 293-302.

[95] D.A. Steinman, J.B. Thomas, H.M. Ladak, J.S. Milner, B.K. Rutt, J.D. Spence, Reconstruction of carotid bifurcation hemodynamics and wall thickness using computational fluid dynamics and MRI, Magnetic resonance in medicine : official journal of the Society of Magnetic Resonance in Medicine / Society of Magnetic Resonance in Medicine, 47 (2002) 149-159.

[96] Q. Long, X.Y. Xu, B. Ariff, S.A. Thom, A.D. Hughes, A.V. Stanton, Reconstruction of blood flow patterns in a human carotid bifurcation: a combined CFD and MRI study, Journal of magnetic resonance imaging : JMRI, 11 (2000) 299-311.

[97] M. Fichman, D. Pnueli, C. Gutfinger, Aerosol Deposition in the Vicinity of a Stagnation Point, Aerosol Sci Tech, 13 (1990) 281-296.

[98] N.R. Labiris, M.B. Dolovich, Pulmonary drug delivery. Part I: physiological factors affecting therapeutic effectiveness of aerosolized medications, British journal of clinical pharmacology, 56 (2003) 588-599.

[99] P. Worth Longest, C. Kleinstreuer, Comparison of blood particle deposition models for non-parallel flow domains, Journal of biomechanics, 36 (2003) 421-430.

Appendix

Streptavidin Site Density

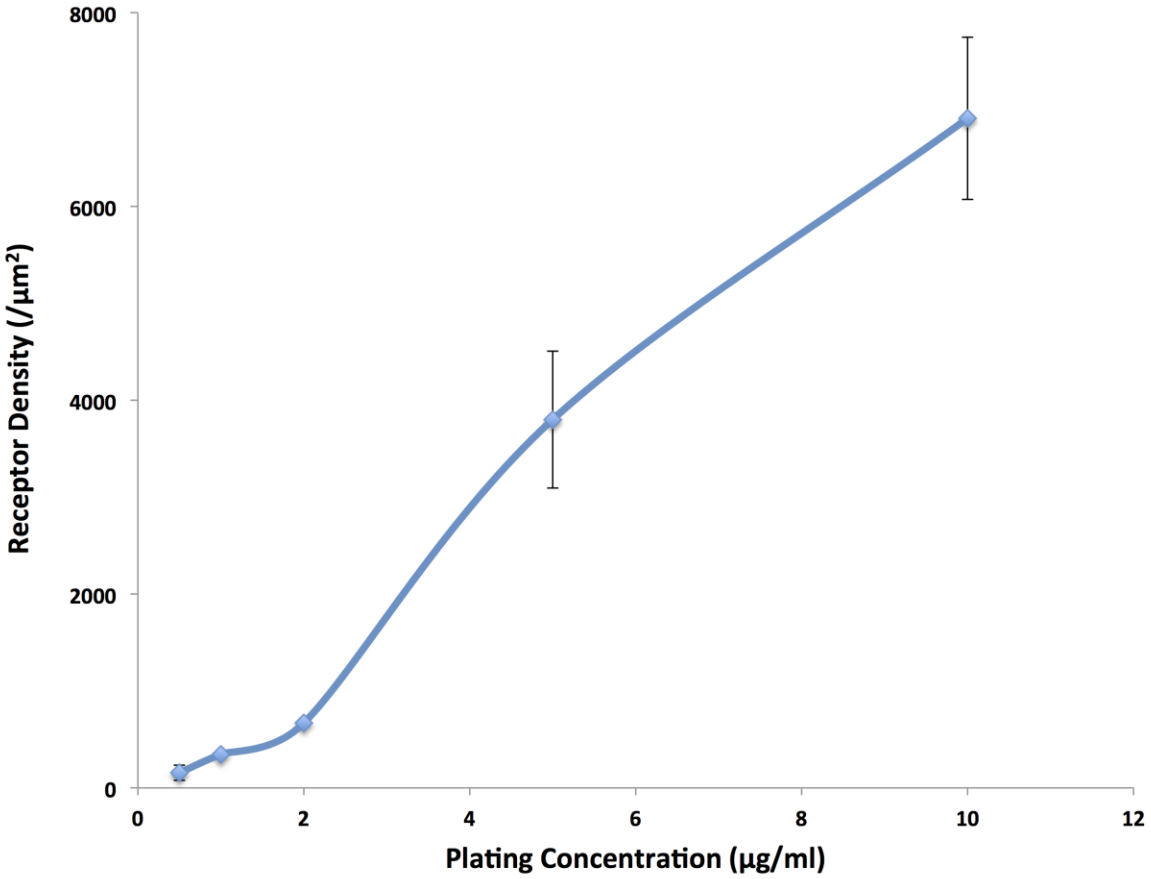

Streptavidin site density was measured using Europium (Eu)-labeled streptavidin (DELFIA, PerkinElmer, Boston, MA) and time-resolved fluorescence (Excitation – 355 nm, Emission – 615 nm). Eu-labeled streptavidin was adsorbed onto polystyrene culture dishes as described in Chap 2 and incubated overnight at 4 C. After washing away excess streptavidin using saline, the dishes were incubated with DELFIA enhancement solution for 15 min to dissociate the Eu^{3+} ions and form a fluorescent micellar solution (n = 5 for 0.5, 5, 10 µg/ml; n = 1 for 1, 2 µg/ml).

CFD Methodology

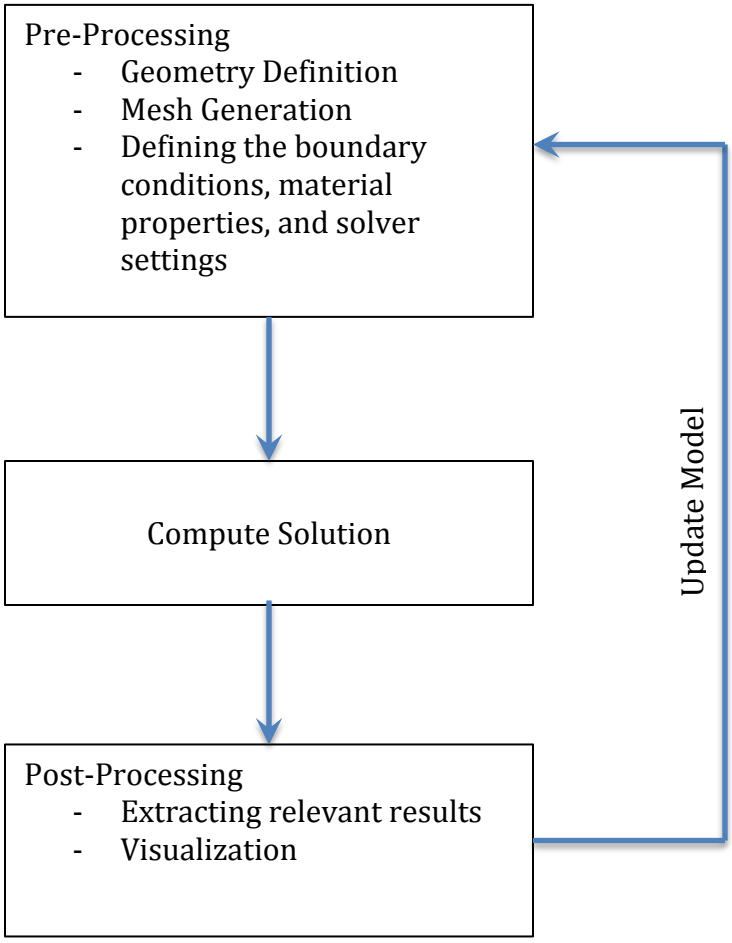

Parameters of the CFD simulation in COMSOL

Dimensions of the model

Inlet height = 254 μm (1:2 model), 127 μm (1:3 model)

Outlet height = 508 μm (1:2 model), 381 μm (1:3 model)

Cross-sectional width of the model = 0.25 cm

Axial length of the model = 0.5 cm

Number of mesh elements – 2.2 million (1:2 model), 2.5 million (1:3 model)

Boundary Conditions (B.C)

- Wall – No-slip B.C
- Inlet – Laminar Inflow B.C (Specified Parameter - Average Velocity)
- Outlet – Pressure B.C (Stress-free, 0 Pa)

Solver Type – Laminar Incompressible, Stationary (Steady state) Flow, Single Phase

Dynamic Viscosity – 0.001 Pa.s for plain buffer, 0.003 Pa.s for higher viscosity fluid

Density – 1000 kg/m^3

Temperature – 293.15 K

Molecular Imaging of VCAM-1 in ApoE-/- and Diet-Induced Obesity Murine Models using Targeted Microbubbles

Introduction

Cardiovascular disease, including coronary heart disease, stroke, and peripheral arterial disease, is a prominent cause of mortality and morbidity across the globe. Atherosclerosis is the underlying pathological process responsible for the disease. Atherosclerosis is a complex disease with key involvement of the immune and metabolic systems. Vascular inflammation plays a central role in the initiation and advancement of the disease. Endothelial cell activation and upregulation of leukocyte adhesion molecules (e.g., VCAM-1, ICAM-1) enable the recruitment of circulating mononuclear immune cells to focal sites in the vessel wall, contributing to disease progression. Inflammatory molecules on the endothelium are thus important markers of disease activity. With the help of molecular imaging, they could be exploited for clinical diagnosis and prediction of disease progression. Inflammation can be assessed non-invasively using targeted microbubbles and ultrasound [1, 2].

Animal models for atherosclerosis research depend on genetic manipulations that affect lipoprotein regulation and metabolism. Apolipoprotein E deficient (apoE-/-) mice and low-density lipoprotein receptor deficient (LDLr-/-) mice are the most commonly used models. With growing understanding of the role of obesity and diabetes in cardiovascular disease, alternative models based on C57BL/6 mice on high-fat diet are now being investigated.

Mice on high-fat diet (~60% diet calories from fat) are known to develop obesity, hyperglycemia, and insulin resistance, and are robust models for understanding the pathology of diabetes [3]. But vascular inflammation in the context of atherosclerosis has not been characterized in this model. The objective of our study was to compare the inflammatory status of the vasculature of the diet-perturbed model with the well-established ApoE-/- high-cholesterol diet model. We used microbubbles targeted to VCAM-1 and contrast-enhanced ultrasound imaging to assess inflammation *in vivo*.

Materials and Methods

Microbubble Preparation

Lipid-shelled biotinylated microbubbles containing decafluorobutane gas were manufactured by sonication of aqueous saline lipid micellar dispersion [4]. For murine VCAM-1 targeting, biotinylated monoclonal antibody against VCAM-1 (MVCAM.A, BD Biosciences, San Jose, CA) was conjugated to the microbubble surface using streptavidin, as previously described [5]. Microbubbles conjugated to isotype-matched IgG were used as control microbubbles. Microbubble concentration and size distribution was measured using a Coulter counter (Coulter Multisizer 3, Beckman Coulter, Brea, CA).

Animal Models

C57BL/6 mice were put on lard-based high-fat diet (HFD mice, 60% caloric intake from fat) at 6 weeks of age. ApoE-/- mice were put on high-cholesterol diet at 6 weeks of age, while wild-type control mice were kept on normal chow diet throughout.

Contrast Enhanced Ultrasound Imaging and Analysis

Ultrasound imaging was performed on animals over 30 weeks old. Imaging was conducted in contrast pulse sequencing (CPS) mode (15L8 probe, Siemens Sequoia) at 7MHz and mechanical index (MI) 0.2. The mice were maintained under anesthesia using 2% isoflurane in air during the imaging period. For the purpose of carotid artery visualization, imaging was performed at the neck region. Microbubbles (~10 million) were administered intravenously as a bolus by retro-orbital injection. Imaging was performed for 10 min after injection. During this period circulating bubbles were cleared from the bloodstream and a fraction adhered to VCAM-1. At the end of 10 minutes, the background image was obtained by destroying the microbubbles in the field of view by increasing the MI to 1.9. Both VCAM-1 targeted microbubbles and control microbubbles were injected in the same animal in no particular order.

Image analysis was performed off-line using ImageJ (NIH, Bethesda, MD). To determine the signal from bound microbubbles, the frames collected after high-intensity destruction of microbubbles were subtracted from the images acquired immediately prior to destruction. Targeting was quantified in a selected region-of-interest (ROI) by normalizing the image intensity at 10 min to the peak echo intensity (observed within 15-20 seconds after injection).

Immunohistochemistry

Immunohistochemistry was performed on tissue sections to detect the presence of VCAM-1. After the animal was sacrificed, the tissue around the neck region was removed for further processing. The tissue was embedded in paraffin and 5 μm-thick sections were prepared. The sections were blocked with 10% horse serum in PBS and avidin blocking

reagent (sp-2001, Vector Laboratories, Burlingame, CA, USA), and incubated overnight at 4 °C with anti-VCAM-1 primary antibody (10 ng/mL). Biotinylated secondary horse-anti-goat IgG (BA-9500, Vector Laboratories) was added to the sections and incubated for 1 h at room temperature. The ABC reagent (PK7100, Vector Laboratories) was then added to the sections and incubated for 45 min at room temperature. For staining, diaminobenzidine (DAB solution, Sigma Aldrich) was used as the chromogen and dark brown color indicated positive reaction product.

Statistical analysis

Data were expressed as mean ± standard deviation. Two-tailed Student t-test was used to compute the p-values and p-values < 0.05 were considered significant.

Results

Figures 1, 2 and 3 show representative CEUS images of VCAM-1 targeting to the carotid vasculature region in ApoE-/-, HFD, and wild-type mice, respectively. Microbubble binding in the vasculature was diffuse and not restricted to the large vessels. Microbubble targeting to endothelial VCAM-1 was more than 2-fold higher in the HFD mice compared to wild-type animals ($p < 0.001$). The binding in HFD model was equivalent to the ApoE-/- animals (Fig. 4). Isotype-matched control IgG microbubbles showed negligible targeting in all experimental groups.

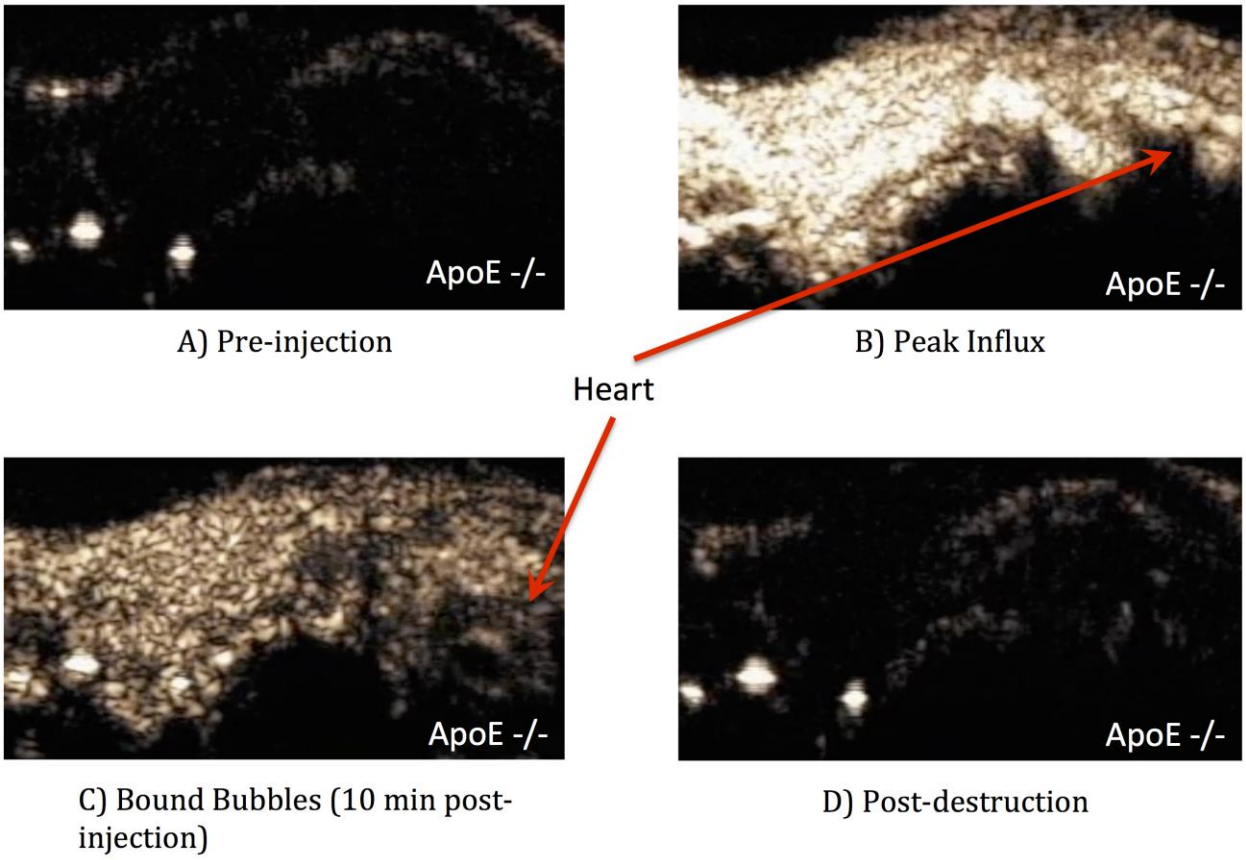

A) Pre-injection

B) Peak Influx

C) Bound Bubbles (10 min post-injection)

D) Post-destruction

Fig. 1: Representative images of targeting in the carotid vasculature region using anti-VCAM-1 antibody conjugated microbubbles in ApoE -/- mice. A) Pre-injection B) Peak signal 15-20 seconds after injection C) Echo signal from bound bubbles 10 min after injection D) Post microbubble destruction

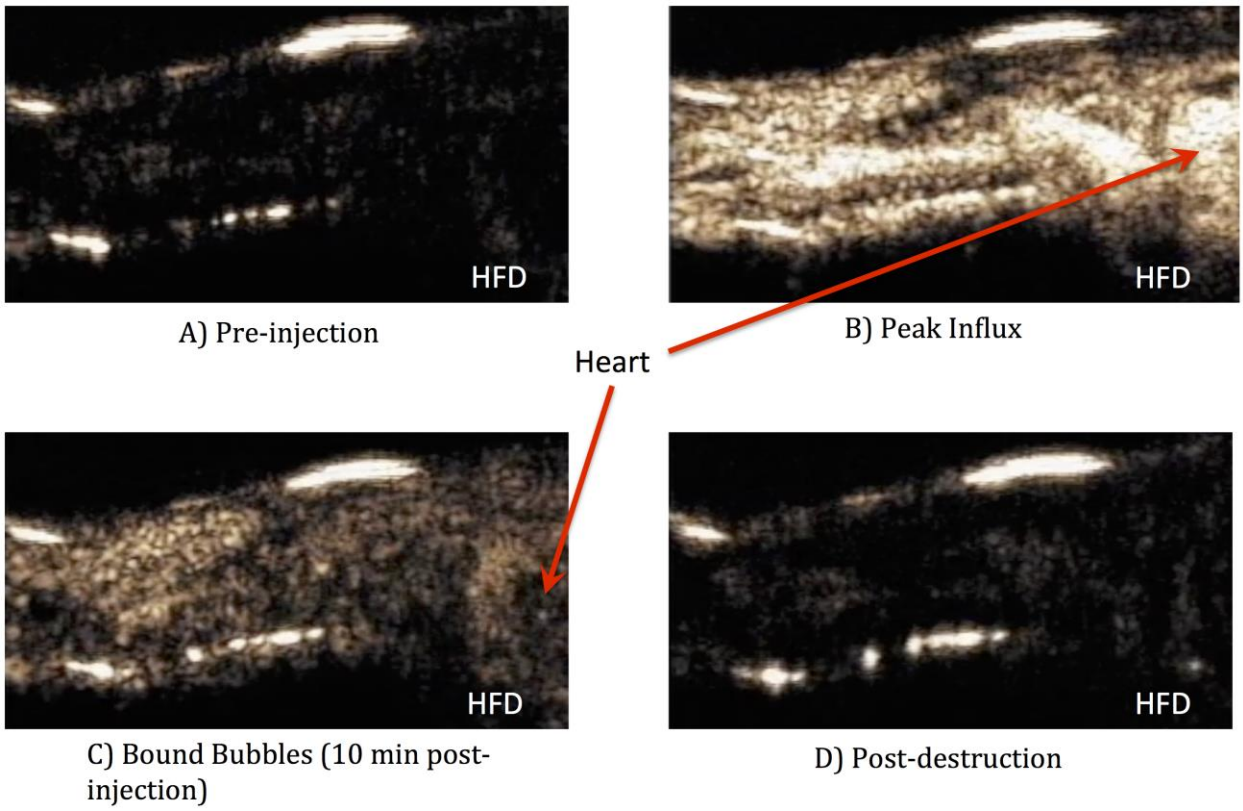

Fig. 2: Representative images of targeting in the carotid vasculature region using anti-VCAM-1 antibody conjugated microbubbles in HFD mice. A) Pre-injection B) Peak signal 15-20 seconds after injection C) Echo signal from bound bubbles 10 min after injection D) Post microbubble destruction

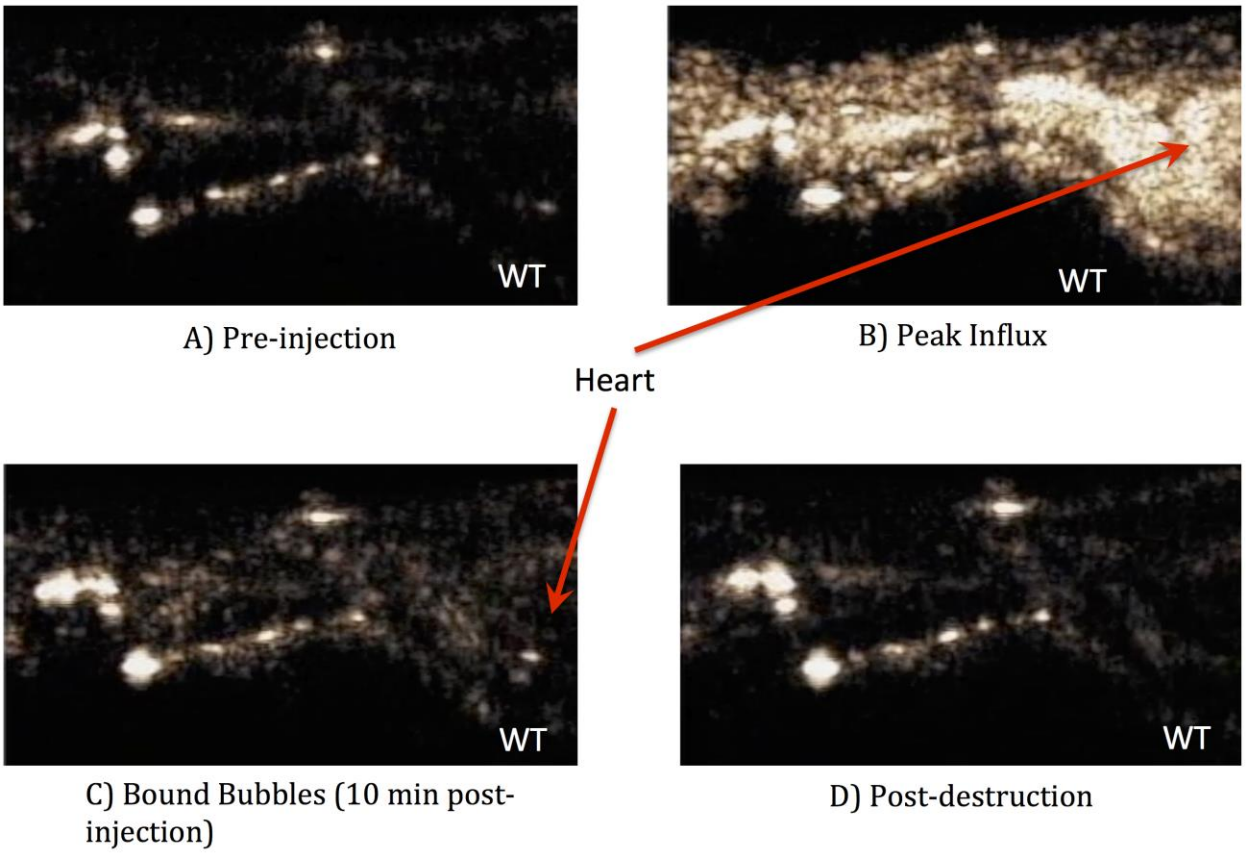

Fig. 3: Representative images of targeting in the carotid vasculature region using anti-VCAM-1 antibody conjugated microbubbles in wildtype (WT) mice. A) Pre-injection B) Peak signal 15-20 seconds after injection C) Echo signal from bound bubbles 10 min after injection D) Post microbubble destruction

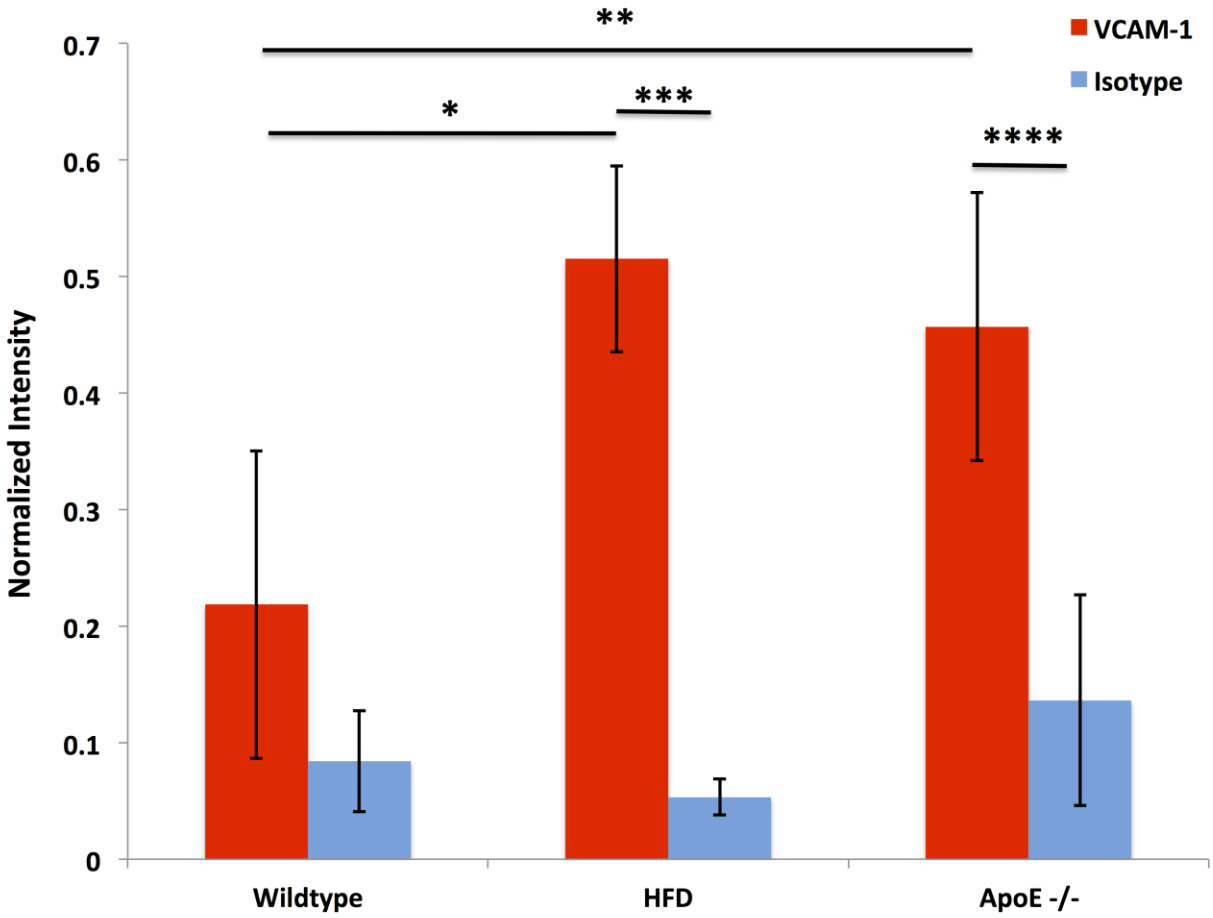

Fig. 4: Microbubble targeting to VCAM-1 in wild-type, HFD and ApoE-/- mice (n=4-6, * $p < 0.001$, ** $p < 0.01$).

Immunohistochemistry was performed on tissue samples obtained from mice that were kept on high-fat diet for 16 weeks. Immunostaining confirmed VCAM-1 over-expression in the vasculature of HFD (Fig. 5A). The presence of VCAM-1 was also confirmed in apoE-/- mice tissue (Fig. 5B). VCAM-1 was not detected in control wild-type animals.

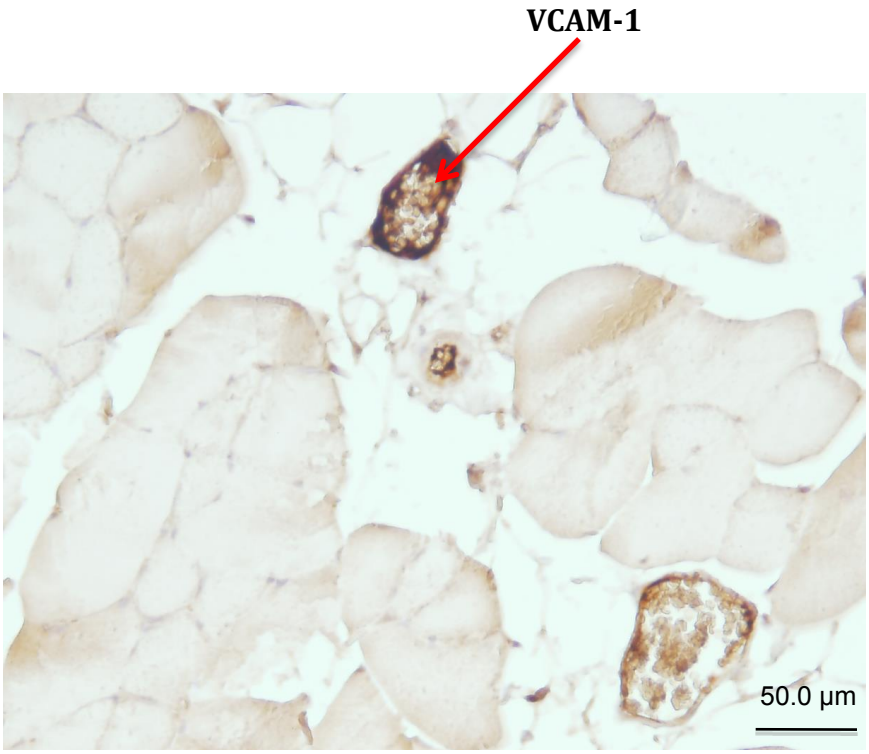

Fig. 5A: Immunohistological detection of VCAM-1 in HFD mice after 16 weeks on diet. Brown color indicates the presence of VCAM-1.

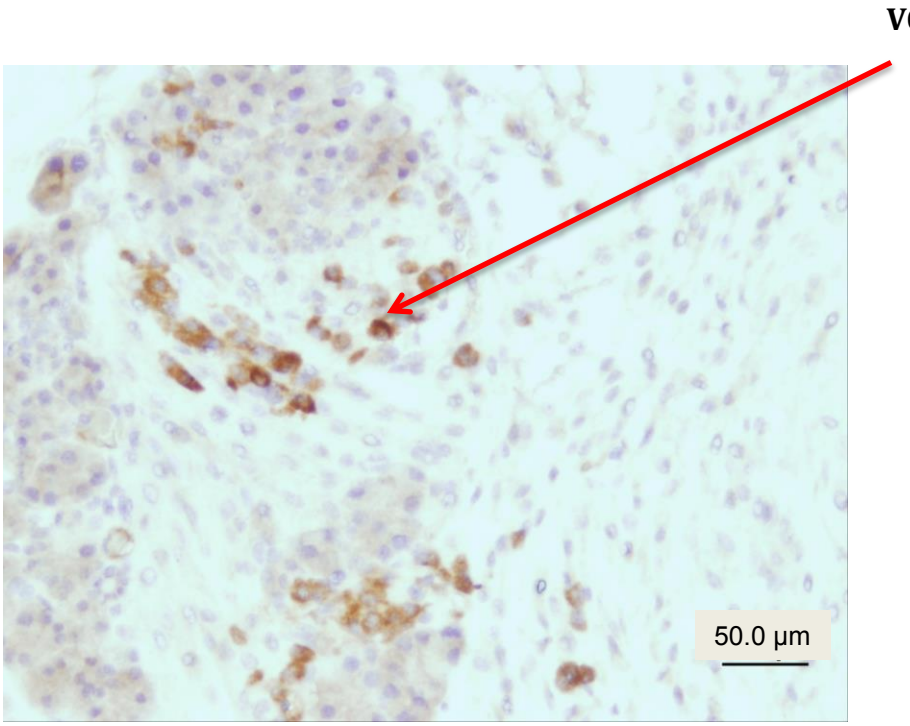

Fig. 5B: Immunohistological detection of VCAM-1 in ApoE-/- mice. Brown color indicates the presence of VCAM-1.

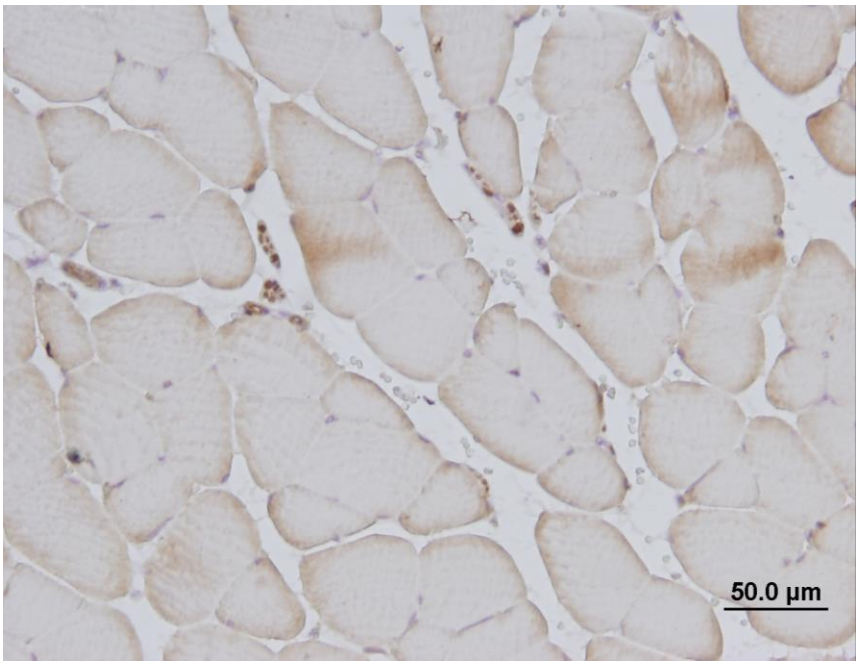

Fig. 5C: VCAM-1 was not detected in control wild-type mice by immunohistochemistry.

Discussion

Cardiovascular comorbidity is common among type 2 diabetes patients. Due to the deleterious effects of dyslipidemia, hyperglycemia, and insulin resistance on the vasculature, diabetes is an independent and key risk factor for the development of atherosclerosis and cardiovascular disease [6, 7]. Inflammatory processes are intimately involved in both diseases. Chronic inflammation of the vessel wall of large arteries results in atherosclerotic lesion formation. Inflammatory cytokines are known to be associated with diabetes and circulating inflammation markers have been suggested as predictors of diabetes and cardiovascular mortality in diabetes [8-10]. Evidence from basic research [11, 12] and patient data [13, 14] indicate that inflammatory processes mediate the link between obesity and type 2 diabetes. Increased levels of cytokines like TNF-α, IL-6, IL-1β [15, 16] and macrophage infiltration [17, 18] characterize adipose tissue in obesity.

Furthermore, in HFD mouse models endothelial dysfunction (ICAM-1 and VCAM-1 upregulation and reduction in NO production) occurs prior to inflammation in liver, skeletal muscle, and adipose tissue [19]. This suggests that endothelial markers of vascular inflammation could be used for early detection of the disease. In conjunction with traditional metrics this information could be factored into prognosis and risk assessment. Molecular imaging using targeted microbubbles can non-invasively evaluate early stages of endothelial dysfunction and temporal progression [20]. In non-human primates on a high-fat diet (36% of caloric intake), carotid artery imaging using targeted microbubbles has demonstrated that the expression of endothelial P-selectin and VCAM-1 precedes the changes in intima-media thickness (IMT), a commonly used clinical metric for assessing carotid arterial disease [21]. Moreover, CAM expression increased over time and this progression could be detected using microbubbles. Similarly, ultrasound imaging of mice on a high-cholesterol diet revealed enhanced accumulation of VCAM-1 targeted microbubbles in the aorta relative to mice on regular chow diet [2].

In the present work, we demonstrated that targeted microbubbles could be used to image vascular inflammation in a HFD mouse model. VCAM-1 targeting in HFD animals was significantly higher (over 2-fold) than in wild type animals on normal chow diet and equivalent to apoE-/- animals on high-cholesterol diet. Interestingly, microbubble accumulation pattern was diffuse and not limited to the large vessels, suggesting systemic and microvascular expression of VCAM-1. This could be caused by an increased production of inflammatory cytokines by nearby subcutaneous adipose tissue depots.

This work illustrates the feasibility of using targeted microbubbles and ultrasound for early detection of endothelial inflammation. Future work would involve investigating the onset

and temporal progression of inflammation in the model. Additionally, different endothelial CAMs (ICAM-1, selectins) could be targeted to understand the nature of the inflammatory response. This might help us distinguish between macro- and micro-vascular responses. Furthermore, for clinical application microbubbles functionalized with peptides would need to be explored.

References

[1] A.L. Klibanov, Targeted delivery of gas-filled microspheres, contrast agents for ultrasound imaging, Adv Drug Deliv Rev, 37 (1999) 139-157.

[2] B.A. Kaufmann, J.M. Sanders, C. Davis, A. Xie, P. Aldred, I.J. Sarembock, J.R. Lindner, Molecular imaging of inflammation in atherosclerosis with targeted ultrasound detection of vascular cell adhesion molecule-1, Circulation, 116 (2007) 276-284.

[3] M.S. Winzell, B. Ahren, The high-fat diet-fed mouse: a model for studying mechanisms and treatment of impaired glucose tolerance and type 2 diabetes, Diabetes, 53 Suppl 3 (2004) S215-219.

[4] A.L. Klibanov, H. Gu, J.K. Wojdyla, J.H. Wible Jr., D.H. Kim, D. Needham, F.S. Villanueva, G.H. Brandenburger, Attachment of ligands to gas-filled microbubbles via PEG spacer and lipid residues anchored at the interface, in: Proceedings of the International Symposium on Controlled Release of Bioactive Materials, Boston, MA, 1999, pp. 124-125.

[5] J.R. Lindner, J. Song, J. Christiansen, A.L. Klibanov, F. Xu, K. Ley, Ultrasound assessment of inflammation and renal tissue injury with microbubbles targeted to P-selectin, Circulation, 104 (2001) 2107-2112.

[6] S.M. Grundy, I.J. Benjamin, G.L. Burke, A. Chait, R.H. Eckel, B.V. Howard, W. Mitch, S.C. Smith, Jr., J.R. Sowers, Diabetes and cardiovascular disease: a statement for healthcare professionals from the American Heart Association, Circulation, 100 (1999) 1134-1146.

[7] J.A. Beckman, M.A. Creager, P. Libby, Diabetes and atherosclerosis: epidemiology, pathophysiology, and management, JAMA : the journal of the American Medical Association, 287 (2002) 2570-2581.

[8] M.I. Schmidt, B.B. Duncan, A.R. Sharrett, G. Lindberg, P.J. Savage, S. Offenbacher, M.I. Azambuja, R.P. Tracy, G. Heiss, Markers of inflammation and prediction of diabetes mellitus in adults (Atherosclerosis Risk in Communities study): a cohort study, Lancet, 353 (1999) 1649-1652.

[9] J.C. Pickup, M.B. Mattock, G.D. Chusney, D. Burt, NIDDM as a disease of the innate immune system: association of acute-phase reactants and interleukin-6 with metabolic syndrome X, Diabetologia, 40 (1997) 1286-1292.

[10] J.C. Pickup, M.B. Mattock, Activation of the innate immune system as a predictor of cardiovascular mortality in Type 2 diabetes mellitus, Diabetic medicine : a journal of the British Diabetic Association, 20 (2003) 723-726.

[11] M.Y. Donath, S.E. Shoelson, Type 2 diabetes as an inflammatory disease, Nature reviews. Immunology, 11 (2011) 98-107.

[12] M.F. Gregor, G.S. Hotamisligil, Inflammatory mechanisms in obesity, Annual review of immunology, 29 (2011) 415-445.

[13] V.C. Luft, M.I. Schmidt, J.S. Pankow, D. Couper, C.M. Ballantyne, J.H. Young, B.B. Duncan, Chronic inflammation role in the obesity-diabetes association: a case-cohort study, Diabetol Metab Syndr, 5 (2013) 31.

[14] C.M. Phillips, I.J. Perry, Does inflammation determine metabolic health status in obese and nonobese adults?, The Journal of clinical endocrinology and metabolism, 98 (2013) E1610-1619.

[15] G.S. Hotamisligil, N.S. Shargill, B.M. Spiegelman, Adipose expression of tumor necrosis factor-alpha: direct role in obesity-linked insulin resistance, Science, 259 (1993) 87-91.

[16] S.E. Shoelson, J. Lee, A.B. Goldfine, Inflammation and insulin resistance, The Journal of clinical investigation, 116 (2006) 1793-1801.

[17] S.P. Weisberg, D. McCann, M. Desai, M. Rosenbaum, R.L. Leibel, A.W. Ferrante, Jr., Obesity is associated with macrophage accumulation in adipose tissue, The Journal of clinical investigation, 112 (2003) 1796-1808.

[18] H. Xu, G.T. Barnes, Q. Yang, G. Tan, D. Yang, C.J. Chou, J. Sole, A. Nichols, J.S. Ross, L.A. Tartaglia, H. Chen, Chronic inflammation in fat plays a crucial role in the development of obesity-related insulin resistance, The Journal of clinical investigation, 112 (2003) 1821-1830.

[19] F. Kim, M. Pham, E. Maloney, N.O. Rizzo, G.J. Morton, B.E. Wisse, E.A. Kirk, A. Chait, M.W. Schwartz, Vascular inflammation, insulin resistance, and reduced nitric oxide production precede the onset of peripheral insulin resistance, Arteriosclerosis, thrombosis, and vascular biology, 28 (2008) 1982-1988.

[20] B.A. Kaufmann, C.L. Carr, J.T. Belcik, A. Xie, Q. Yue, S. Chadderdon, E.S. Caplan, J. Khangura, S. Bullens, S. Bunting, J.R. Lindner, Molecular Imaging of the Initial Inflammatory Response in Atherosclerosis Implications for Early Detection of Disease, Arterioscl Throm Vas, 30 (2010) 54-U132.

[21] S.M. Chadderdon, J.T. Belcik, L. Bader, M.A. Kirigiti, D.M. Peters, P. Kievit, K.L. Grove, J.R. Lindner, Proinflammatory endothelial activation detected by molecular imaging in obese nonhuman primates coincides with onset of insulin resistance and progressively increases with duration of insulin resistance, Circulation, 129 (2014) 471-478.